DIGITAL MICROFLUIDICS FOR THE DETECTION OF INORGANIC IONS IN AEROSOLS

by

Shuquan Huang

Department of Electrical and Computer Engineering

Duke University

Date:_____

Approved:

_____

Richard B. Fair, Supervisor

_____

Hisham Massoud

_____

Ana P. Barros

_____

Krish Chakrabarty

_____

Tony Jun Huang

Dissertation submitted in partial fulfillment of
the requirements for the degree of Doctor
of Philosophy in the Department of
Electrical and Computer Engineering in the Graduate School
of Duke University

2018

ABSTRACT

DIGITAL MICROFLUIDICS FOR THE DETECTION OF INORGANIC IONS IN AEROSOLS

by

Shuquan Huang

Department of Electrical and Computer Engineering

Duke University

Date:_____

Approved:

_____

Richard B. Fair, Supervisor

_____

Hisham Massoud

_____

Ana P. Barros

_____

Krish Chakrabarty

_____

Tony Jun Huang

Dissertation submitted in partial fulfillment of
the requirements for the degree of Doctor
of Philosophy in the Department of
Electrical and Computer Engineering in the Graduate School
of Duke University

2018

Abstract

The quantitative measurement of inorganic ions in the atmosphere is an important aspect in environmental science. The three most important inorganic ions are sulfate, nitrate and ammonium, which are the most abundant components of atmospheric pollutants and have a significant impact on rainfall, atmospheric visibility and human health. To accurately and quickly measure the distribution of inorganic ions in the vertical and horizontal directions of the atmosphere, a compact and automatic real-time detection system is in need.

The research performed in this study is aimed at developing the science and technology for an aerosol detection system that combines digital microfluidics technology, aerosol impaction and chemical detection on the same chip. The system will be smaller and faster with respect to current aerosol analyzing instruments. The chip in this study performs the integrated functions of aerosol collection, extraction, and quantitative detection in real-time, unlike current benchtop methods that require operator handling and laboratory equipment. All functions are realized in dedicated sections on a digital microfluidic platform.

This thesis will present the design and test of individual components of the aforementioned functions. The digital microfluidics chip design includes transparent top and bottom plates for light absorbance measurement. The droplets are dispensed, transported and mixed on chip with other droplets by activating electrodes individually with a 50V AC sine voltage.

In Chapters 3 and 4, the issues involving droplet transportation are addressed, including

droplet movement between the air and silicone oil media and droplet transport across the aerosol impaction area. Next, an aerosol impactor and a chip-to-world chamber are demonstrated and tested with lab generated sulfate aerosol. The collected aerosol showed a clear pattern on the impaction plate, and the collection efficiency inside the chip was 96%.

In Chapter 5, the development of colorimetric methods are described as well as experimental testing for inorganic ion detection. Three well-known tests for detecting sulfate, nitrate and ammonium were first adjusted to adapt to on-chip measurement conditions, the adjustments including the choices of solvent, concentration ranges and mixing ratios. The particle measurement results using a conventional spectrometer were compared with on-chip measurements in terms of absorbance range, limit of detection, sensitivity (based on the coefficient of determination and the slope of the linear regression) and signal-to- noise ratio (presented with standard deviation/average of absorbance measurements).

The thin oil film between the droplet and the top/bottom plate, which is naturally formed, plays an important role in lubrication and reduces contact angle hysteresis. However, these oil films are not always uniform in thickness. During the absorbance measurement tests, varied sizes of oil lenses were observed at the oil/top plate interface, and the size and position of the oil lenses randomly changed when a droplet moved between electrodes. The absorbance measured in the normal direction to the chip's surface was affected by these oil lenses and, thus, not stable for multiple measurements of the same droplet or for different droplets. To solve this problem, optical fibers were

introduced horizontally inside the chip, and measurements taken in this direction proved to produce stable results.

Prototypes of the chip have been fabricated, and the impaction and on-chip colorimetric tests for sulfate and ammonium were successful. Although this study was designed to build the fundamentals of a novel detection system of inorganic ions in aerosol, the potential use of the designed system is not limited to atmospheric studies. Applications can extend to testing the quality of drinking water, detection of nitroaromatic explosives or other experiments based on colorimetry.

Contents

List of Tables

List of Figures

Acknowledgements

It is with immense gratitude that I acknowledge my academic advisor, professor Fair, who started this project with professor Khlystov (Dessert Research Institute). Professor Fair gave me the most support during my research and my study in Duke University.

Credits of this work are shared with Jessica Connelly, whom I collaborated with, and contributed greatly in developing chemical assays and aerosol collection assays.

My sincere thanks to Feilun Wu from Professor You's group, who helped me with colorimetric assays with the equipment from her lab.

My great appreciations go to all my lab mates, especially, Liji Chen helped me with the chip design and fabrication. Shruti Preetam and Yaas Bigdeli always share ideas and updates with me. I learned a lot from them.

Great thanks to Steven Earp and Greg Bumpass from Duke student machine shop, for their expertise in machines, and patience when teaching me using the tools. Also, thanks to Duke SMIF clean room and the staffs.

I would like to thank my undergraduate study program advisor, Professor Reed (University of Virginia), for giving me an opportunity to try doing research as an undergrad. That experience greatly influenced me.

Last but not least, I would like to thank my family and friends. My parents Jinlong Huang and Peng Peng, and my best friend Siyun Yang.

Chapter 1 Introduction

1.1 Introduction and Motivation

Atmospheric particulate matter (PM) is the general term for various suspensions of fine solid particles or liquid droplets in the atmosphere. These suspensions of fine particles are relatively evenly dispersed in the air to form a stable suspension system, or an aerosol system [1]. Aerosols are multiphase systems composed of particles and ambient gases. Dust, smoke, fog and haze are all commonly found in the category of aerosols. The size of atmospheric particles is closely related to their properties [2], and it is one of the most often studied characteristics in sampling and subsequent research. The shapes of the atmospheric particles are irregular, and the particle size is represented by the aerodynamic diameter, Stober [3], which is defined as the diameter of a sphere with a unit density (ρ_0 = 1 g/cm^3) that reaches the same final settling velocity as the actual particle when it moves with low Reynolds number in still air. According to the aerodynamic diameter, atmospheric particles can be divided into different categories. Pooley and Gibbs [4] defined particles that can enter the human alveoli as $PM_{2.5}$, or particles with an aerodynamic diameter of 2.5 microns or less. $PM_{2.5}$ has a smaller particle size and larger surface area to volume ratio, and thus is more chemically active and easily attaches toxic and harmful substances [2] [5]. It also has a long residence time in the atmosphere and a long transportation distance [6]. Day-to-day particulate air pollution is associated with an increased risk of various adverse health outcomes, including cardiopulmonary mortality [7]. The latest research shows that ambient $PM_{2.5}$ has been found to rank fifth in mortality risk factors and was the cause of 7.6% of total global deaths in 2015 [8].

The Air Quality Index (AQI) is a non-linear, non-dimensional index that quantitatively

describes air quality. Larger values indicate more serious air pollution. According to the U.S. Clean Air Act [9], criteria for six pollutants should be regulated based on each individual AQI, and they are ground-level ozone, particle pollution, lead, carbon monoxide, sulfur dioxide and nitrogen dioxide [10]. The U.S. Environmental Protection Agency has established standards for each of these pollutants [10]. In this thesis, two pollutants in the AQI that are of interest are nitrogen dioxide (NO_2) and sulfur dioxide (SO_2). The most updated corresponding EPA primary standards (for public health protection) are: for nitrogen dioxide: the level for 98th percentile of 1-hour daily maximum concentrations over 3 years is 100 parts per billion (ppb), and for sulfur dioxide: the level for 99th percentile of 1-hour daily maximum concentrations over 3 years is 75 ppb [10]. The predominant chemical components in $PM_{2.5}$are sulfate, nitrate, ammonium, sea salt, mineral dust, organic compounds and black or elemental carbon [11] [12]. The inorganic ions – sulfate, nitrate and ammonium each contribute 10-30% of the total aerosol mass [13]. Particulate matter can be divided into primary particles and secondary particles. Primary particles are natural pollutants and artificial sources of pollutants released into the atmosphere directly, such as soil particles, sea salts, burning smoke and so on. Secondary particles refer to the solid or liquid particles generated from atmospheric gaseous pollutants through a series of chemical transformation or physical process, and they are the main source of $PM_{2.5}$ [14] [15]. The gas precursors are mostly SO_2, NO_x (NO, NO_2), and NH_3 [16]:

$$SO_2 \xrightarrow{[O]} H_2SO_4 \xrightarrow{NH_3} (NH_4)_2SO_4$$

$$NO_X \xrightarrow{[O]} HNO_3 \xrightarrow{NH_3} NH_4NO_3$$

During the formation of nitrates and sulfate, the same amount ($(NH_4)_2SO_4$, NH_4NO_3) of product is generated from reactants (SO_2, NO_2) in terms of parts per billion, thus the targeted detection range is 0-100 ppb for nitrate and 0-75 ppb for sulfate.

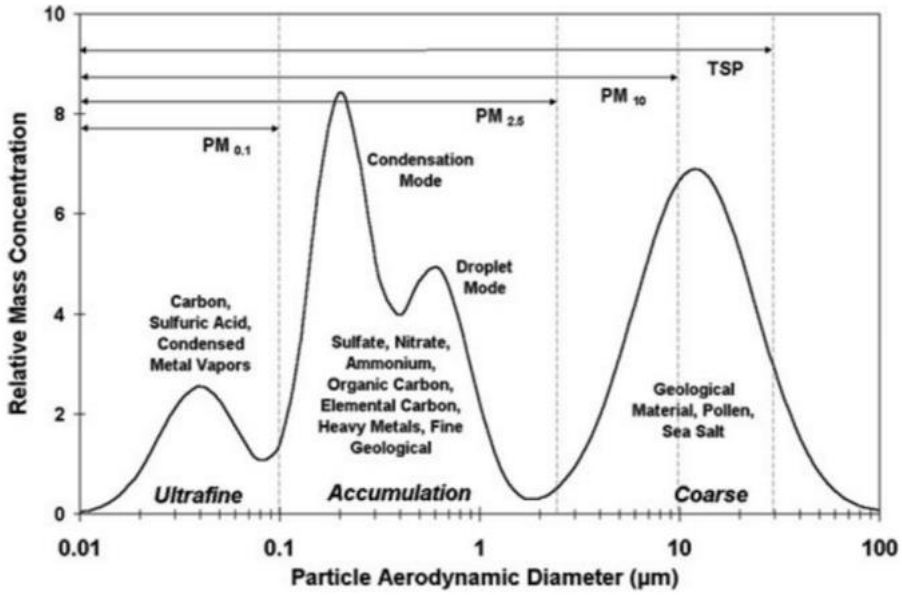

Figure 1: Relative mass concentration as a function of particle aerodynamic diameter [2]

It can be seen from Figure 1 [2] that $PM_{2.5}$ happens to have a trough between two modes, and it includes all particles that lie in the left region of the line that indicates 2.5 µm. Most of the fine particles from human activities are found in this region, and they are the particles that affect public health the most.

To address the problem of monitoring fine inorganic particulates in real time, this thesis explores the integration of an electrowetting-on-dielectric (EWD) digital microfluidics platform with an aerosol collection system to create a portable instrument for detecting and quantifying airborne chemical components sulfate, nitrate, ammonium in $PM_{2.5}$. Realization of a proof-of-concept instrument that demonstrates fundamental scientific principles is a key step towards further development of flyable, portable systems that can measure airborne contaminants over large areas.

Specifically, this thesis advances the hypothesis that the scientific and engineering basis for integrating aerosol collection into the EWD microfluidic environment requires the

development of on-chip chemical assays, stable colorimetric detection techniques, and on-chip impaction and collection of aerosol particulates for analysis. The following specific hypotheses were developed to aid in designing the experimental tasks performed on this research:

Hypothesis 1: It is possible to design and manufacture a microfluidic chip that incorporates areas for particle collection and extraction, reagent storage, and colorimetric detection of sulfate, nitrate and ammonium.

Hypothesis 2: It is possible to adapt bench-top colorimetric assays for nitrate, sulfate and ammonium detection to be compatible with a digital microfluidic platform.

Hypothesis 3: The microfluidic platform can efficiently extract water soluble components from a variety of on-chip impacted aerosol matrixes of particles larger than 100 nm.

By way of background, current collection and detection methods will be first reviewed.

1.2 Current Aerosol Collection and Detection Methods

1.2.1 Off-line methods

Off-line methods are the most widely used in aerosol analysis. These methods involve separate steps for aerosol collection or sampling, and chemical detection. Collection or sampling methods include filtering, inertial sedimentation, centrifugal sedimentation, gravitational sedimentation and thermal collection [17]. According to different

measurement methods and purposes, the collected samples need to be pretreated to separate and concentrate the chemical components, and this is often done with extraction.

Analytical measurements include X-ray fluorescence (XRF), Fourier-transform infrared spectroscopy (FTIR), atomic absorption spectroscopy (AAS), gas chromatography (GC), high-performance liquid chromatography (HPLC), ion chromatography (IC), secondary ion mass spectrometry (SIMS), and inductively coupled plasma mass spectrometry (ICP-MS) [18-20].

Off-line analysis uses the above conventional chemical analytical methods and does not require modification of measuring instruments. However, these methods are not specifically designed for analyzing atmospheric particles, because these methods are not aimed at the composition of atmospheric particulate matter and because the concentration ranges of the target analytes are too large or too small, so that it takes a long time to collect sufficient amounts of samples or the samples need to be diluted. Also, during sample collection, transportation and pretreatment, there are many factors that can cause measurement errors. Temperature and humidity changes may cause adsorption, absorption or reaction between gas components and the particulate matter. The loading and unloading of the collection membrane may cause samples to fall off. The component to be measured may react with certain types of filters or pre-treatment solvents, causing changes of content in the sample. Meanwhile, sampling and preprocessing offline can be time-consuming, and will make it difficult to perform a long time-resolved dynamic study of chemical composition of the atmospheric particles.

1.2.2 On-line methods

To obtain the space-time distribution of aerosol composition and concentration, online

analytical methods have become one of the hot topics in the study of atmospheric particles. One reason is that the online methods are more sensitive and require smaller concentrations of collected samples. Also, avoiding the steps of sample pretreatment and transportation will reduce the time for a complete run of an analysis. Another reason is that the collected samples do not need to be stored, and random errors that may be introduced in the off-line methods are reduced.

Scaringelli and Rehme [21] first built a sulfuric acid aerosol online analyzer. The aerosols were collected by impaction and filtration, then sulfuric acid was decomposed at a controlled temperature, which formed sulfur trioxide. This product was then transformed into sulfur dioxide with heated copper at 500℃, and measured with flame photometric detection.

Crider [22] built a hydrogen flame emission spectrophotometer to measure both sulfur dioxide and sulfuric acid aerosol. The peak emission intensity was at 380 nm, although a 402 nm filter was used, since it was the closest wavelength the researcher could get. The apparatus was exposed to room air for 2 minutes for calibration, and the peak response was reported to occur at the end of the 2-minute sulfur exposure. However, this sulfur detection system had several drawbacks. One was that the system did not distinguish the chemical form of sulfur, although by using a filter, gaseous sulfur and particulate matter could be measured separately. Another drawback was that other ions might interfere with the emission at 402 nm.

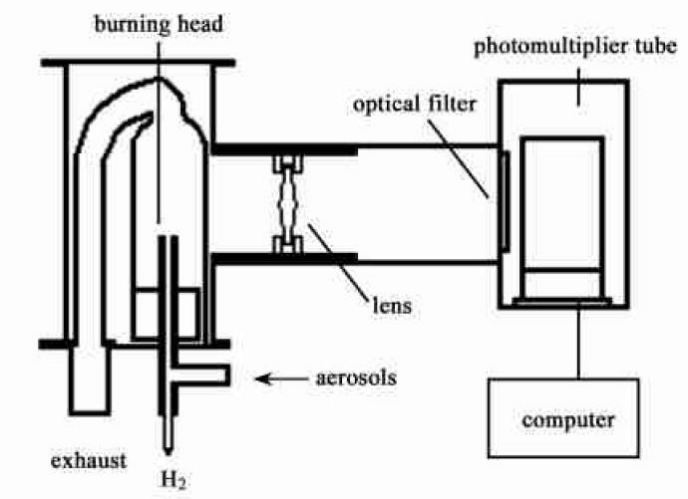

Figure 2: Online analyzer for sulfate in aerosol by flame emission spectroscopy [23]

Slanina et al [24] developed an automatic thermodenuder system to measure ammonium sulfate concentration in aerosols. The collected air sample first entered a K_2CO_3 denuder and carbon denuder, which trapped the SO_2 and H_2S gases. Then sulfuric acid and ammonium sulfate volatilized and was collected separately at 120℃ and 220℃, respectively. Ammonium sulfate was then treated in a Cu/CuO denuder and transformed to sulfur dioxide. The sulfur dioxide was measured by a Meloy SA 285 flame photometric sulfur analyzer.

A method for automated measurement of nitrate in atmosphere was invented by Stolzenburg [23]. Samples were collected by humidified impaction, and after going through flash vaporization, analysis was done by a chemiluminescent NO_x analyzer (model 42C, Thermo Environmental Instruments). The chemistry was based on reducing higher nitrogen oxides to nitric oxide (NO), and chemiluminescence was measured when NO reacted with ozone. The typical collection time was 8 minutes, and analysis time was 90 seconds. However, ammonium ions and nitric oxide were reported to interfere strongly with the nitrate measurement.

In the past two decades on-line methods also have been developed to be used in aircraft research. One of these methods is a particle-into-liquid sampler (PILS) coupled with an ion chromatography (IC) system [25]. This instrument can measure particles with diameters between 0.03 and 10 μm. By carefully choosing columns and eluents, nine major inorganic species can be separated and measured in 3.5-4 minutes.

Another popular aircraft-based research instrument is the aerodyne aerosol mass spectrometer (AMS). The TSI 3800 was the world's first commercially available aerosol mass spectrometer. It addressed the need for real-time size and chemical composition measurement of each single particulate matter sample. The particle time-of-flight data was used to calculate the exact time when each particle flies to the focal point, where a laser emits and ionizes the particle. The ionized particle then enters a time-of-flight mass spectrometer (TOFMS) and its chemical composition is analyzed.

Figure 3: TSI ® Series 3800 Aerosol Time-of-Flight Mass Spectrometer [26]

While these systems have proven to provide high quality data in aircraft studies, they

are large and heavy, and require specially trained personnel to operate and maintain. The costs for purchase and maintenance are high as well. Tradeoffs between expense, instrument sensitivity, time resolution and ease of use are likely involved.

The goal of the present research was to find a simpler and cheaper solution that provides comparable or improved resolution and efficiency of state-of-the-art aerosol sensing instruments. This new technology should feature an integration of aerosol collection and chemical analysis, and should have the advantage of less reagent consumption, less waste, and the portability to be used in aircraft research.

1.3 Proposed Integrated On-chip Aerosol Collection and Analysis

An integrated aerosol detection system is proposed and scientifically and experimentally demonstrated in this thesis based on digital microfluidics for on-line analysis of sulfate, nitrate and ammonium. The system combines aerosol impaction, extraction and chemical detection on the same chip in real time. The system is smaller than current aerosol analyzing instruments (the chip and the chip-to-world connection occupy less than 10 cm^3). The collection, extraction and detection functions were individually designed and tested, and the results are discussed in Chapters 3, 4 and 5.

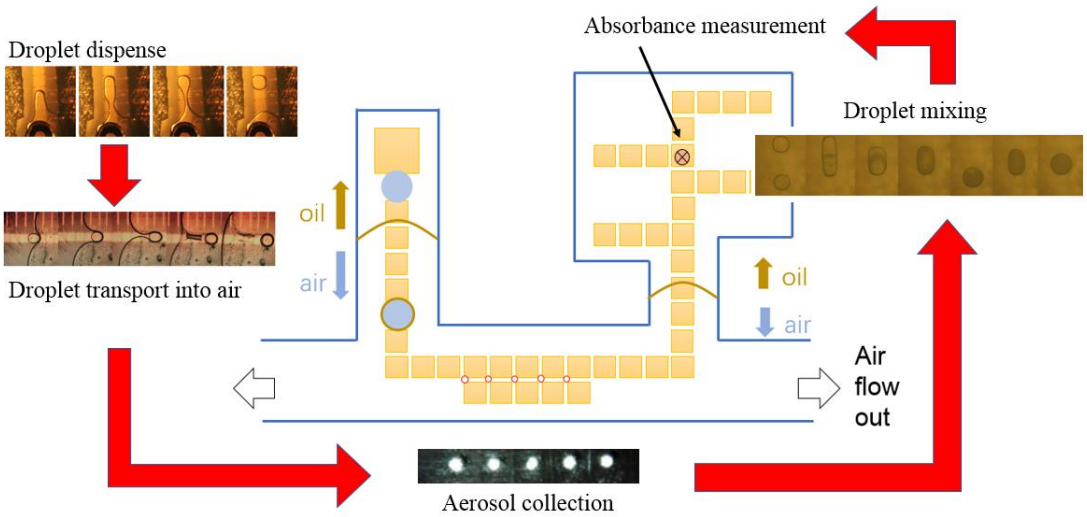

Figure 4: Diagram of inorganic ion concentration analysis process for aerosols. Middle: digital microfluidics chip layout. From left to right following the red arrows: the functional areas of the chip are displayed in sequence - droplet dispense, droplet transport, aerosol collection, mixing and absorbance detection in the colorimetric test.

The operation of the integrated chip system is shown in Figure 4. Aerosol impaction from an air stream is first performed on five sequential electrodes on the chip. After the air flow is stopped, a droplet of water or buffer solution is dispensed into an oil medium from a reservoir and moved through an oil/air interface by electrowetting to the impaction/collection area of the chip. The collection droplet in the air medium is clad with a thin oil film to reduce droplet evaporation and aid droplet transport by electrowetting on dielectric (EWD). The collected aerosol from the five sequential electrodes dissolves in the oil-clad buffer droplet, providing the five-fold concentration of aerosol in a single droplet. Next, the droplet with dissolved analytes is moved through an air/oil interface for further analytical processing.

A background absorbance measurement will be made in the optical detection system to account for the contribution of the insoluble and other light absorbing material. This

background reading will be used to correct the colorimetric measurements. The droplet will then be split into three droplets. Droplets of reagents for each of the analytes will be dispensed from the corresponding reservoirs and mixed with the extract droplets in the oil medium, and the absorbances of the final mixed droplets are measured.

Sufficient time is required to collect adequate concentrations of impacted sample, so that when the sample is extracted into the testing droplet, the concentration of the analyte is in the detectable range. If C_d is the concentration of the analyte in the extraction droplet and C_a is the concentration in air, Q is the flow rate of air, t is the sampling time, and V is the volume of the droplet, then the relationship between Cd and C_a is:

$$C_a = \frac{C_d V}{Q t} \quad (1)$$

Three colorimetric tests for measuring the concentrations of sulfate, nitrate and ammonium will be introduced in Chapter 2.3. When three ions coexist in the droplet, and even other intervening ions coexist in the droplet, the effect of these ions on absorbance will be introduced in Chapter 5.1.3.

The on-chip colorimetric assays have been found to have a limit of detection 0.25-11 ppm, and the corresponding limit of detection in air is 0.15 ppb – 6.6 ppb. The shortest time of one cycle of measurement including collection time, extraction time, reaction time and detection time was found to be about 1-2 minutes.

The limit of detections compared with current state-of-the art measurement results of Stolzenburg's automated system (0.4 μg/m^3 or 0.0004 ppb) and Crider's aerosol sulfur detector (<1 ppb) are smaller, but the method proposed in this study requires less aerosol collection time (<1min compared to a few tens of minutes to hours). The results were obtained in a chip and the chip-to-world connection that occupies less than 10 cm^3 compared with 200 kg, 0.5 m^3 AMS systems, or 50-100 kg, 0.2 m^3 PILS

systems, or TOFMS systems shown in Figure 3.

The following objectives have been pursued in a proof-of-concept research effort to create an integrated on-chip aerosol collection and analysis system:

1. Design a microfluidic chip that incorporates areas for particle collection and extraction, reagent storage, and colorimetric detection of sulfate, nitrate and ammonium.
2. Develop micro/nanoliter colorimetric assay formulations for nitrate and ammonium detection that are compatible with the digital microfluidic platform.
3. Fine-tune droplet actuation conditions for efficient extraction of target compounds from a variety of aerosol matrixes.
4. Characterize particle collection efficiency and potential interferences and artifacts during the sampling and analysis steps.

With these objectives in mind, the following chapters of this thesis describe the theoretical and experimental results that have driven the co-design of the first microfluidic chip that integrates aerosol collection and on-chip analytical analysis of collected analytes. Chapter 2 gives an overview of the core technologies that are utilized in the chip/collector co-design. Chapter 3 describes theory and experiments behind transporting collection droplets from an oil medium to an air medium for scanning particles through an oil/air interface. Chapter 4 describes the measurement of particle impaction efficiency, and Chapter 5 describes issues in achieving stable absorption measurements of collected analytes in droplets contained in an oil medium.

Chapter 6 presents conclusions, contributions and recommendations for future work.

Chapter 2 Technology Overview

The process flow of the experimental prototype chip designed for proof-of-concept studies begins with aerosol collection, as shown in Figure 4. Then a droplet of water or buffer solution is dispensed and moved by electrowetting to the collection area of the chip. The collected aerosol dissolves in the buffer droplet. Next, the droplet with dissolved analytes is moved to mix with colorimetric assay reagents, and the absorbance of the final mixed droplet is measured. The principle of droplet control is introduced in chapter 2.1. The technology used to realize two main functions on the chip, aerosol collection and ion detection, including sulfate, nitrate and ammonium are discussed in Chapter 2.2 and 2.3. The selection of these technologies to a large extent depends on whether the technology is suitable for a digital microfluidic device, and the performance and reliability of these certain technologies are also considered.

2.1 Digital Microfluidics

Microfluidic devices are gaining popularity as an alternative to bench-top chemical analysis. They are miniaturized platforms that integrate basic operation units such as sample preparation, reaction, separation and detection in biological, chemical and medical analysis onto a single chip, and the entire analysis process may be automated. The microfluidic chip has the advantages of controllable flow, low reagent consumption and increased speed of reaction in reduced liquid volumes.

This technology is made possible with microelectromechanical system (MEMS) technologies. The first groundbreaking miniaturized total chemical analysis system (μTAS) developed by Manz et al. [27] was based on conventional planar processing technology used in fabricating microelectronic devices, including photolithography and

wet etching. Later, Whitesides et al. [28] developed soft lithography, which used elastomeric materials to build complex structures such as microchannels, further simplifying manufacturing process and reducing cost.

There are still two shortcomings about many microfluidic devices. The first is that even when the lab environment is miniaturized and put onto a small chip, bulky off-chip lab equipment such as mechanical pumps, valves and tubes are used, which make the device not a lab-on-a-chip but a chip-in-a-lab. To solve this problem, among all the various mechanisms that can cause a liquid to move, the one that requires the least peripheral structures is the most desirable. The second problem is to make the device programmable and reusable. With continuous-flow microfluidics, the physical structures such as fluid channels, reservoirs and pumps, and physical parameters, such as the position of the sensors, are predetermined. The chip is limited to do a specific application only. In the development of microfluidic systems, surface tension is widely used as the driving force of the liquid. In fixed channel devices, the driving method that makes use of capillary force between liquid and channel walls is simple and does not require much energy, but because more and more functions are required on the chip, the microfluidic operation steps are more complex, and the irreversible driving mode and fixed flow path make it more difficult to design and fabricate a highly efficient chip system. Thus, it is important to use capillary force in a more flexible way.

The concept of digital microfluidics came to solve these two problems. Digital microfluidics deals with discrete droplets instead of continuous flows. The main idea is its three-level hierarchy of design [29]. The top level is the design of the chip's scientific functions, which are usually biomedical functions, such as agent detection, DNA analysis, or immunoassays. The second level is the top-level applications decomposed into elemental fluid functions, such as mixing, transporting, or detection. The user can

realize top-level functions by combining these second-level functions. The bottom level is composed of physical structures, such as channels, valves, and mixers. Only the top level will be programmable by the end user. The device is designed to perform three ion detections and the user can decide each protocol from the beginning of aerosol collection to absorbance measurement. All variables, including collection time, how many times the droplet scans through the impaction area, detection time, etc. can be controlled by the user. Based on aerosol concentration range and composition in different regions, the user has the freedom to develop a specific testing method.

2.1.1 Principle of digital microfluidics – electrowetting on dielectric (EWD)

At the end of the nineteenth century, G. Lippmann [30] found that when the voltage between a liquid-gas interface and a liquid-solid interface changes, the interfacial tension will also change, which causes the liquid to move reversibly. This is called electrowetting (EW). A subsequent study [31] also found that if the voltage is applied to a metal surface covered with a few microns of insulating film, the operational reliability is greatly improved, and electrolysis phenomenon, that causes electrode damage and deterioration of the specimen, can be avoided. To differentiate from earlier electrowetting technology, this improved technology is called electrowetting-on-dielectric (EWD) technology.

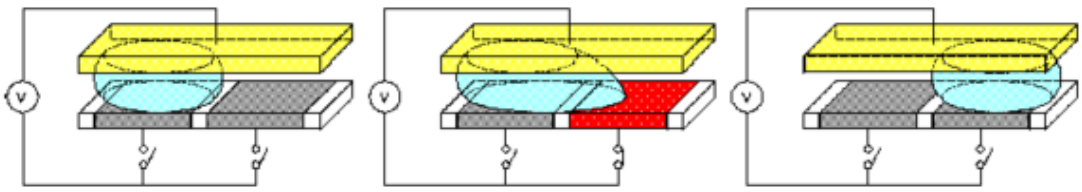

Figure 5: Droplet transport in an electrowetting on dielectric device. [32]

The EWD system consists of top and bottom plates that sandwich a fluid layer, as shown in Figure 5. The bottom plate comprises conductive electrodes that are patterned on an insulating substrate and a dielectric layer that is deposited over the electrodes. The top plate is grounded during operation. Both surfaces of top and bottom plates are modified to be hydrophobic. When a voltage is applied to an electrode, the contact angle of the droplet on the dielectric surface is changed. Electric potentials applied between the EWD electrodes and the top plate counter electrode reduce the contact angle of a droplet positioned on an electrode, thus increasing the wetting area of the droplet. Since changing the contact angle of liquid by an applied voltage can control the movement of liquid on a hydrophobic surface, a single droplet can be actuated across a dielectric covering two electrode plates with different voltages, and the droplet tends to move to the electrode with the higher applied voltage. The attraction is stronger when the applied voltage difference is larger, as is the droplet transport velocity. If these electrodes are arranged in a checkerboard pattern beneath a hydrophobic insulator, it is possible to direct the droplets of a specimen or reactant to a specific position for chemical reaction or analysis. In addition to its high efficiency and low energy consumption, this microfluidic operational platform with electrical controls has the potential for system miniaturization and integration with integrated circuit back-end control systems. Furthermore, using electrode arrays can achieve the manipulation of both continuous and discontinuous fluids (digital microfluidics).

Droplet transport is achieved by a non-zero net force from electrowetting. As shown in Figure 5 [32], the top plate is electrically conductive and grounded, the bottom has two separate electrodes, and the droplet overlaps both electrodes. When the electrode on the right side of the droplet is activated, contact angle changes according to Young-Lippmann equation [30]:

$$\gamma_{SL}(V) = \gamma_{SL}(0) - \frac{\epsilon_0 \epsilon_r}{2d} V^2 \qquad (2)$$

$\gamma_{SL}(V)$ is the surface tension between the liquid and the solid when the voltage is on, and it is smaller than $\gamma_{SL}(0)$, which is the surface tension when the voltage was off. ϵ_0 and ϵ_r are permittivity of free space and relative permittivity of the dielectric, d is the dielectric thickness, and V is the applied voltage.

The phenomenon is shown by a changing contact angle:

$$\cos\theta_V = \cos\theta_0 + \frac{\epsilon_0 \epsilon_r}{2d\gamma_{LV}} V^2 \qquad (3)$$

Here θ_V and θ_0 are the contact angles with and without applied voltage. γ_{LV} is the surface tension between the liquid and the medium.

The changing surface tension along the contact line is the force for droplet movement.

A hydrophobic layer is added to prevent contact angle saturation, which is observed when the contact angle cannot be further reduced by applying larger voltage. Contact angle saturation in water is about 80˚ [33], so the larger θ_0 is, the more effective the force difference between interfacial surface tension is to overcome the drag force. For the same reason, the top plate has a continuous layer of conductive material, and on top of that, a layer of hydrophobic surface coating.

For continuous flow devices that use pump systems, one problem of using microchannels and microvalves is that in order to provide a continuous flow of a specimen, a dead volume is often formed in the beginning of the operation, and this part of the valuable specimen is wasted [34, 35]. Digital microfluidics can access and manipulate liquid from anywhere on the chip and effectively solve this problem. Also, because droplets have a large surface-to-volume ratio, digital microfluidics can shorten

the reaction and detection time greatly [36, 37].

EWD-based platforms include four basic types of droplet operation: droplet transportation, droplet mixing, droplet splitting and droplet dispensing. By programming this operation and simply using electrical signals, it is possible to conduct complex, trace molecular detection.

2.1.2 Chip design and chip fabrication process

The purpose of this research was to develop a Lab-on-Chip system to be used in aerosol analysis studies. The chip performs the functions of aerosol collection, extraction, and detection in real time. All functions are realized in dedicated sections on a digital microfluidic platform. Different approaches for each function are first designed and tested individually, including aerosol impaction, droplet dispensing with different kinds of reagents, droplet transport between silicon oil/air interface and across the impaction area, and colorimetric assays for sulfate, nitrate and ammonium measurement.

The bottom plate and the top plate (Figure 6) are fabricated separately, and later pressed together with a gasket layer put in between. The bottom substrate is on a 500 μm thick borosilicate glass wafer. 140 nm indium tin oxide (ITO) is sputtered and patterned into 0.7 mm × 0.7 mm electrodes with 0.05 mm separation space between each. Then a 1.3 μm thick Parylene C is deposited as the dielectric layer. Finally, 90 nm spin-on CYTOP (AGC Chemicals) covers the entire surface and the chip is baked at 100˚C followed by 190˚C, each for 10 minutes. This allows glass transition of CYTOP to happen.

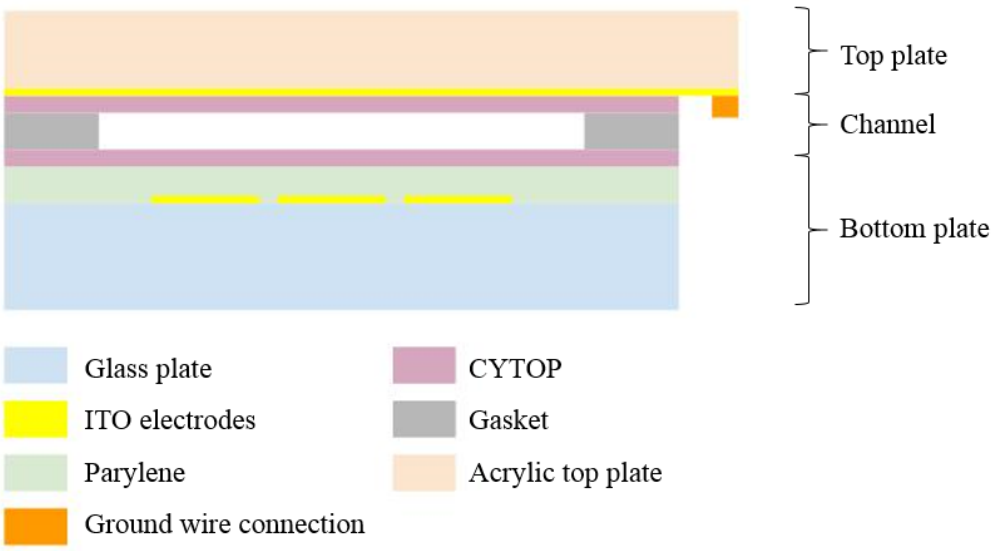

Figure 6: The cross-sectional view of the chip

The top plate is made from 1 mm thick acrylic sheet, its pipette ports and impactor nozzles are made by a drill press. The drill size used for the small impaction nozzles is #88 and the diameter is 0.2413 mm. The top plate is completely covered with 140 nm ITO and 90 nm CYTOP. However, the plate may not be baked, since acrylic starts melting when temperature is above 65˚C and warping destroys the ITO conductivity. Instead, the chip is left in a desiccator overnight to allow CYTOP to dry. This makes CYTOP not resistive to acidic solutions.

ITO is used to make the electrodes because it is a transparent conductive material, so the absorbance can be measured with the droplet sitting on any of the electrodes. CYTOP is used as the final hydrophobic layer because of its unique characteristics: transparency, electric insulation, water and oil repellency, and chemical resistance.

There are two design patterns for the electrodes. The first design (Figure 7) is on a

42×30mm chip with 32 pins and 57 electrodes to perform the full function of collection and detection. Because the goal is to fit in more electrodes with less connection pads, each connection pad has to control multiple electrodes.

Transportation electrodes are 1mm×1mm squares. The five “T” shaped electrodes in Figure 7 are reservoirs, and the inlet holes are drilled on the top plate right above them. The aerosol analysis process happens on the chip from left to right: region 1: droplet dispensing; region 2, droplet transportation across the oil/air interface; region 3, aerosol deposition; region 4, colorimetric detection. The gasket is designed so that region 1 and region 4 are in ambient oil. The top plate has five drilled impaction holes right above the aerosol deposition electrodes. This chip design is used for aerosol deposition tests. The size of the chip is large and only four chips can be made out of a 4” wafer.

The second generation chip design (Figure 8) is a smaller chip, the size of it is 28×23 mm, and eight chips can be made on a single wafer. There are 20 connection pads (long rectangular shapes) and 26 electrodes, so the chip is also a multiplexed system, meaning that one connection pad connects to multiple electrodes. This design is used for absorbance tests for ion detection, and there are only four reservoir holes drilled on its top plate.

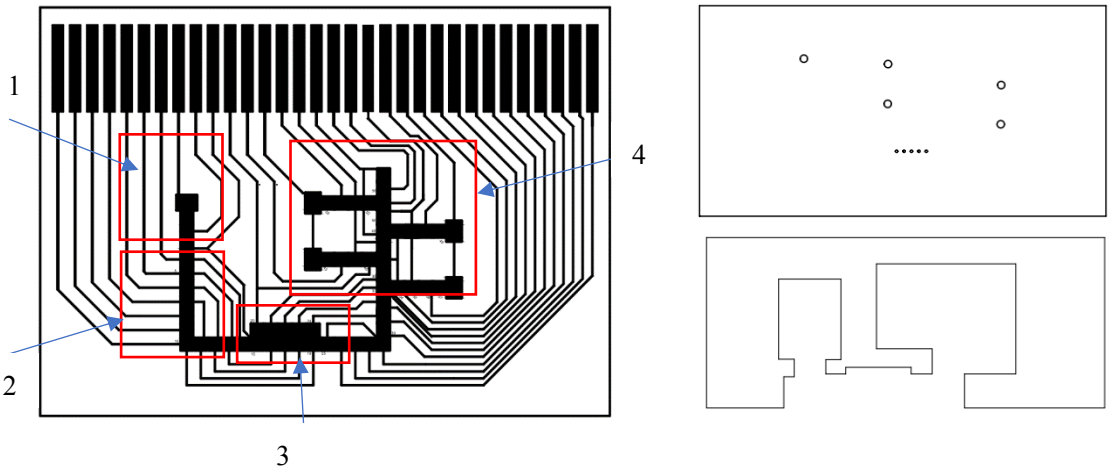

Figure 7: Initial chip design. Left: bottom plate. Right top: top plate. Right bottom: gasket (42×30 mm chip)

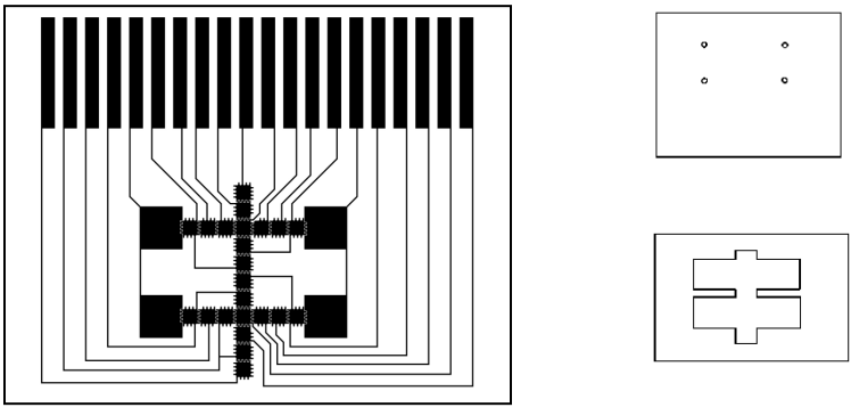

Figure 8: Second generation chip design. Left: bottom plate. Right top: top plate. Right bottom: gasket (28×23 mm chip)

2.2 Aerosol Collection – Impaction

In general, aerosol collection requires a steady flow of air and a planar collecting surface. Depending on desirable aerosol sizes and collecting efficiency, different methods have been extensively explored. However, not all are applicable in this project,

considering the following design constraints provided by collection on an EWD chip:

1) The impacted particles should be soluble in the collection droplet
2) The collecting surface over which the collection droplet passes should be compatible with EWD droplet transport
3) Larger airflow rates can reduce collection time; however, the maximum amount of airflow should be compatible with EWD devices operating with a millimeter scale.

Common collection methods include impaction [38], filtration [39], cyclones [40], and a virtual impactor [41]. However, a porous or fibrous surface is not suitable for EWD droplet transport. Thus, filters are not compatible with digital microfluidics. Cyclones use centrifugal force to separate particles with large inertia. When gas that contains impurities enters the cyclone separation tube, the airflow is guided by the blades and forms a strong rotation. The dense particles and droplets react under centrifugal force and are deposited on the wall. This will not fit with the chip's design either. A virtual impactor is also based on the principle of inertia, and it is an improvement from the traditional solid inertial impactor [42]. The traditional impactor, due to the collisions between particles and a solid surface, has problems with particle fracture, particle bounce and reentry, and excessive deposition [43]. The virtual impactor introduces a collection cavity to replace the previous impaction plate [44]. This is not an ideal aerosol collection method for an electrowetting chip.

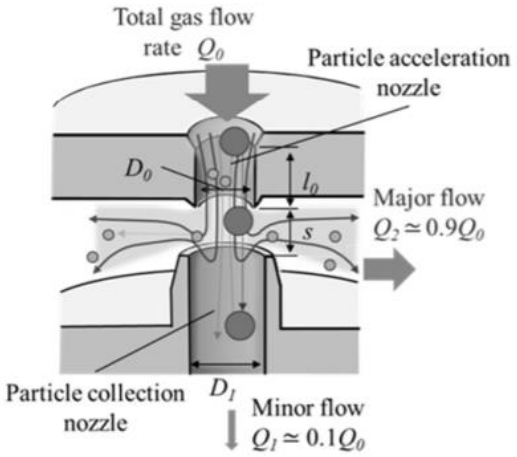

Figure 9: The principle of operation of a virtual impactor. Particles larger than the cut-off size follow the minor flow and particles smaller follow the major flow. The minor flow rate is typically 10% of total flow rate [44].

The most commonly reported impactors are inertial impactors, and numerous studies have been conducted on optimizing collection efficiency as well as improving the relationship between aerosol cut-off diameter and geometric dimensions [45-49]. Thus, the inertial impactor is chosen to be the primary collection method used in this work. As shown in Figure 10, the inertial impactor separates aerosols from airflow by a 90° trajectory change, based on the inertia of particles. Larger particles have a larger turning radius. In Figure 10, r_1 represents the turning radius of a larger particle, which impacts the collector plate, while r_2 represents the turning radius of a smaller particle, which is exhausted from the system. Thus, when air flow changes direction at a T-junction from vertical to horizontal flow, the larger particles are impacted since they are not able to follow the horizontal flow path [49]. These large particles form a deposition pattern under the inlet nozzles until a liquid droplet with chemical reagents passes through the impaction area and dissolves them.

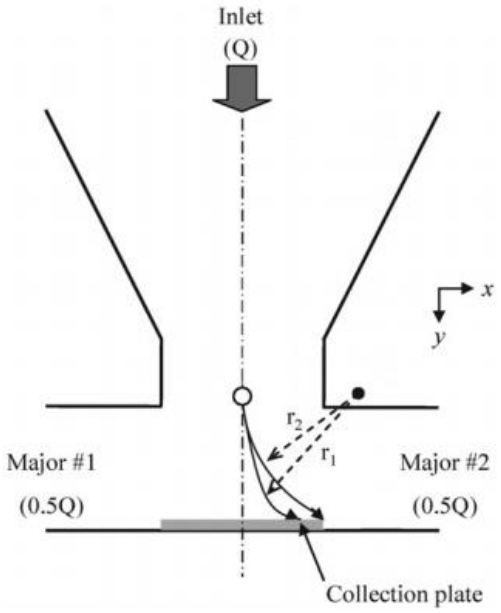

Figure 10: A schematic diagram of inertial impactor with circular nozzle [44]

The design of an inertial impactor is based on both empirical data and fluid mechanics. By solving Navier-Stokes equations [44], Marple found that particle velocity is a function of physical dimensions of the impactor and the Reynolds number (Re) at the nozzle, where Re is defined as:

$$\mathrm{Re} = \frac{\rho v_0 L}{\mu} \quad \text{For circular nozzles} \qquad (4)$$

$$\mathrm{Re} = \frac{\rho v_0 2L}{\mu} \quad \text{For rectangular nozzles} \qquad (5)$$

Here ρ is the air density, v_0 is the airflow velocity at the end of the nozzle, L is the diameter of circular nozzles or the width of rectangular nozzles, and μ is the viscosity of air.

The trajectory of a particle determines if the particle can be collected by the impaction plate. The solution for a particle trajectory is a function of the particle's Stokes number. Larger Stokes number means that it is more difficult for the particle to change direction

with the airflow. The cutoff diameter is defined as the diameter of particles with 50% collecting efficiency and can be expressed as [50]:

$$d_{50}\sqrt{C_c} = \left[\frac{9\eta L(Stk_{50})}{\rho v_0}\right]^{\frac{1}{2}} \qquad (6)$$

In the equation, d_{50} is the cutoff diameter, C_c is the Cunningham slip correction factor, η is the air viscosity, and ρ is the particle density. Since

$$v_0 = \frac{Q}{\pi r^2} = \frac{4Q}{\pi L^2} \qquad (7)$$

where Q is the volumetric flow rate, and for $d_{50} \geq 0.1\ \mu m$, C_C is approximately 1 [51], we can derive

$$d_{50} = \left[\frac{9\pi\eta L^3(Stk_{50})}{4\rho Q}\right]^{\frac{1}{2}} \qquad (8)$$

Thus, the collection efficiency is a function of Stokes number of the particle, Reynolds number of the airflow, and the physical dimensions of the impactor (nozzle diameter or nozzle width L, the distance between nozzle end and impaction plate S, and the nozzle length T). Experimental results show that the design considerations of an impactor include the following [52]:

1) The minimum value of S/L should be:

   S/L =1 for circular nozzles

   S/L = 1.5 for rectangular nozzles

2) Re should be between 500 and 3000. When Re is in this region, the collection efficiency curve is not much affected by Re [52].

3) T/L > 1.0. The nozzle length T does not greatly influence the collection efficiency unless the nozzle is too short for the particle to accelerate to the same velocity of the air flow [52].

Based on conditions 1) and 2), $\sqrt{\mathrm{Stk}_{50}}$ should be 0.49 and 0.77 for round and rectangular nozzles, respectively. Based on the aforementioned principles, the design of the impactor is explained in Chapter 4.

2.3 Colorimetric Detection of Inorganic Ions

There are many ways to analyze inorganic ions, including gravimetry, turbidimetry, spectrophotometry, ion chromatography and inductively coupled plasma emission spectrometry [54, 55]. EPA has developed standard methods for all these methods [56-59]. Ion chromatography is based on the principle of ion exchange and can qualitatively and quantitatively measure a wide range of ions. In recent years, ion chromatography is the most widely used method in detection of inorganic anions, organic acids and cations in the rain or in the atmosphere, because it can analyze multiple components in the same run, uses less chemical reagents, and has higher sensitivity and good selectivity [60, 61]. However, the separation of the mixture in the column requires the ionic solution to be in a mobile phase and requires a pump to provide carefully controlled pressure. This makes it difficult to create an interface between the digital microfluidics chip to the continuous flow required in the column. Instead, a colorimetric method that is based on chemical reaction and spectrophotometry is a more compatible method.

The Lambert-Beer Law (also called Beer's Law) explains the basic principle of spectrophotometry [62]. It explains the relationship between the light absorption at a

certain wavelength, the concentration of the light-absorbing substance, and the thickness of the liquid layer. According to the Lambert-Beer law [63, 64], when monochromatic light travels through absorbing media, the transmitted light decreases with traveled distance and the concentration of absorbing medium. The relationship is:

$$A = -\log_{10}\frac{I_t}{I_0} = \log_{10}\frac{1}{T} = \varepsilon lc \qquad (9)$$

In the equation above, A is absorption, I_0 is intensity of incident light, I_t is intensity of transmitted light, T is transmittance, ε is molar absorptivity (also called the molar extinction coefficient) when c is in mol/L, l is path length, and c is analyte concentration.

In spectrophotometric analysis, Beer's Law is limited. The main factors that would make Beer's Law ineffective include the following: the light is not monochromatic, and the light spectrum band width is too large; the measured substance is uneven and contains tiny particles, and the light is scattered; the incident light is not perpendicular to the optical surface of the cuvette, the actual optical path length through the measured substance is greater than the thickness of the cuvette (This situation has little effect on linearity and is generally negligible). The most important factor is when the concentration of analyte is too high (generally 10^{-2}M), the analyte molar absorptivity will be a function of the analyte concentration, causing nonlinearities to occur and Beer's law to fail. This is because the analytes with high concentration are dissociated or associated with the solvent, or in other words, the solute-solute or solvent-solute interactions change. These will cause significant changes in the absorption curve, including the shape, position and strength of the absorption peak, and will cause deviation from the Lambert-Beer law [65, 66]. Beer's Law applies only to uniform,

non-scattering dilute solutions with a concentration less than 0.01M.

The three colorimetric tests used in this work have been studied with bench-top analyzer systems, but if these are to be performed on the digital microfluidics chip, the conditions will be different. The on-chip light sources are LEDs with peak wavelengths tuned to the specific analyte detection reactions. Each LED has a wide wavelength range, and the FWHM is about 20-60 nm (Figure 11). A filter is not used for on-chip measurements, whereas the spectrometer takes measurements at the wavelengths that have the largest molar attenuation coefficients (not at the leak wavelengths) for the three different tests. The light, after entering the chip from the bottom, passes through multiple interfaces in the entire light path. The refraction, scattering and reflection on each interface also affect the measured value of the transmitted light intensity. These may have an impact on light absorbance. This is studied in Chapter 5.

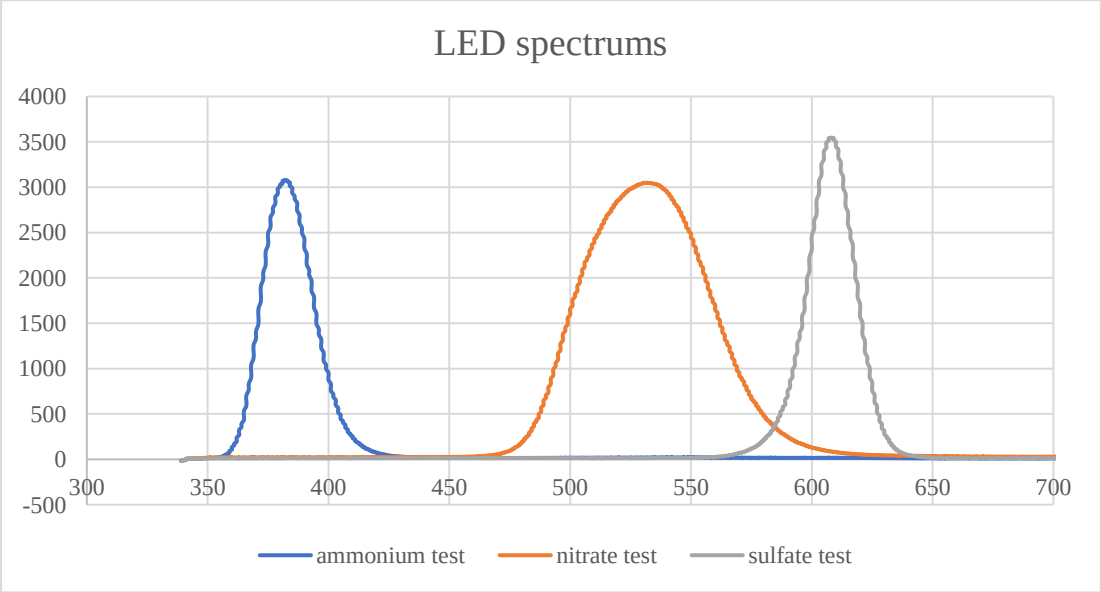

Figure 11: Three led luminescence spectra

2.3.1 Sulfate colorimetric method

The methylthymol blue (MTB) method was first used to detect sulfate concentration in rainwater by Madsen and Murphy [67] who reported the detection limit of 500 ppb. The methylthymol blue method is based on the following reactions:

$$xSO_4^{2-} + yBa^{2+} \rightarrow xBaSO_4 + (y-x)Ba^{2+} \qquad pH = 2$$

$$(y-x)Ba^{2+} + zMTB \rightarrow (y-x)MTB\text{-}Ba + (z-y+x)MTB \qquad pH = 12$$

MTB-Ba is methylthymol blue complexed with one barium ion. Uncomplexed MTB has an absorption peak at 460 nm, while the absorption peak of complexed MTB is at 608 nm. However, the sensitivity of change in absorbance as a linear function of MTB-Ba at 608 nm is three times larger than the sensitivity change with uncomplexed MTB at 460 nm [67]. So, the absorbance at 608 nm is measured to determine sulfate concentration.

EPA published method 375.2 for standard procedure of sulfate colorimetric method using MTB [68, 69]. A mixture of barium chloride and MTB is first prepared, then the sample containing sulfate is added to the solution, with the pH of the solution adjusted by hydrochloric acid. This will allow barium sulfate to form. Next, the pH of the solution is raised by adding sodium hydroxide solution, and the excess barium ions form a complex with MTB.

2.3.2 Nitrate colorimetric method

The rapid detection of nitrate can be achieved by the color reaction between nitrate and nitrate reductant and chromogenic reagent [70-72]. The Griess test from the year 1879

for detecting nitrite has been a mature experimental method, and has been used for detecting nitrite in drinking water and for detecting explosives [73,74]. The limit of detection can be as low as 125 μM. Nitrate ions do not easily form colored products. If the ions can be reduced to nitrite, then it is possible to use the Griess test for detection. In EPA standard method 353.2, copper-cadmium is used to reduce nitrate. However, cadmium is toxic, and the cost for dealing with the waste stimulated the search for an alternative. Campbell [75] found in plants that a natural biological catalyst can be used instead of cadmium. This nitrate reductase (NaR) extracted from corn leaves has been well studied and a manufactured test kit is now on market [76, 77].

The following procedure is the detection steps used in bench-top and on-chip experiments The first step is to add NaR and nicotinamide adenine dinucleotide (NADH) into the nitrate samples. Nitrate will be reduced to nitrite:

$$NO_3^- + 2H^+ + 2e \xrightarrow{NaR} NO_2^- + H_2O - 89.2\text{kj mol}^{-1}$$

Then the formed nitrite is measured using the Griess test. Griess reagent is the color reagent that produces a pink color when added to nitrite. It is composed of sulfanilamide and N-(1-Naphthyl) ethylenediamine dihydrochloride in acid condition. First, sulfanilamide and nitrite undergo a diazonium reaction. Then the N-(1-Naphthyl) ethylenediamine dihydrochloride is added and performs a coupling reation with the product from the previous step to give a colored azo compound.

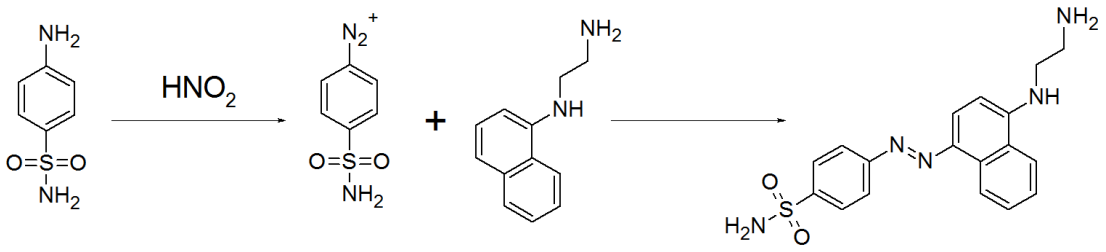

The absorption is measured at 540 nm. The color depth is linearly related to the concentration of nitrate from the original solution.

2.3.3 Ammonium colorimetric method

The most commonly used ammonium detection method is the indophenol blue method [78], and EPA method 350.1 [79] explains this standardized and automated colorimetric method. It is based on ammonium ions reacting with hypochlorite ions and phenolic compounds in alkaline solution, forming indophenol blue that absorbs at 690 nm. Sodium nitroprusside is added to intensify the color. Another very popular method is the Nessler method, when ammonium ions react with Nessler's reagent (composed of potassium tetraiodomercurate (II)) and turns the color of the solution from light yellow to deeper brown by forming a brownish precipitation [80].

However, although these two methods have been intensively used, they have caused controversy in terms of the sensitivity, reliability and difficulty of performance, especially the Nessler method [81, 82], where the blank has been reported to show a high and inconsistent blank absorbance. Both methods are prone to interferences including aromatic amines and amino acids. Both methods generate hazardous wastes (cyanide and mercury) that need to be treated before disposal. These two methods are gradually replaced by the orthophthaldialdehyde (OPA) method [83, 84]. The OPA method reaction is:

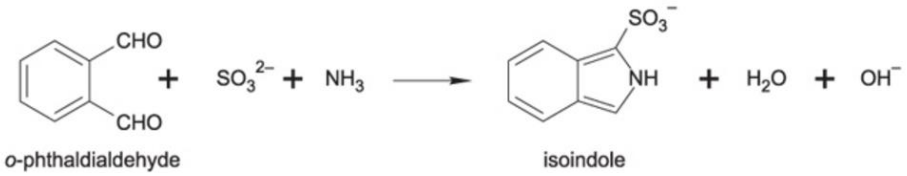

Ammonium reacts with OPA and sulfite to produce highly fluorescent isoindole derivatives. The maximum excitation wavelength is at 361-365 nm and the maximum emission wavelength at 422-425 nm [85]. Although the OPA method was first designed to be a fluorometric method, after testing and plotting the absorbance and emission curves in this work, it was found that the absorbance measurements generated highly linear results. The fluorescence signal was too strong for both off-chip spectrometer and on-chip measurement. The solution must be diluted 100 times to be in a readable range. For all on-chip tests, absorbance at 365 nm was measured. This will be discussed in Chapter 5.

2.4 Vertical and Horizontal Absorbance Measurements

All chemical reactions were done on chip by droplet mixing. To measure the absorbance of a droplet without moving the droplet out of the digital microfluidics chip, an optical detection system adapted to the chip structure needed to be constructed. There have been a few designs, as explained below.

The concentration of glucose can be measured by a colorimetric enzyme-kinetic method. Srinivasan et al [86] designed the measurement system shown in Figure 12. The light path is in the direction perpendicular to the digital microfluidics chip, the LED is used as the light source, and after passing through the layers of the chip and the droplet, the

light is received by a photodiode and converted into a voltage signal. In this experiment, the concentration of the light absorbing material (quinoneimine) in the droplet linearly increases with time, and the reaction rate at which the quinoneimine is produced is related to the concentration of glucose in the droplet, which can be calculated from a time-absorbance plot.

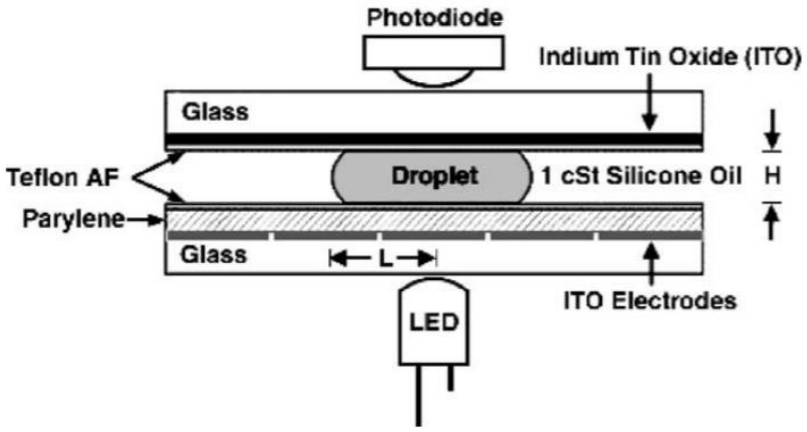

Figure 12: The vertical cross-section of the electrowetting chip along with the optical detection instrumentation [86]

In this way, with the vertical measurement, the distance the light travels through the droplet is only a few tenths of a millimeter. In another experiment (also a glucose concentration test) [87], the light path is longer, the change in absorbance is more pronounced, as shown in Figure 13.

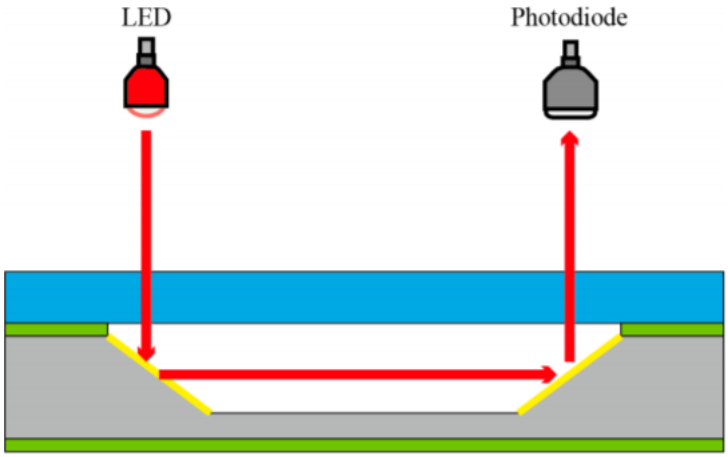

Figure 13: Absorbance measurement system on a continuous-flow microfluidics chip with a longer light path. The 45° surfaces (yellow) are cover by aluminum. [87]

This way of increasing the length of the optical path essentially is to change the optical path into a horizontal direction. There are several studies about how to design a waveguide in the horizontal direction of a channel for in-plane detection.

A proof-of-concept system to measure surface plasmon resonance of a droplet with a gold nanoparticle (Au NP) – saline solution system is shown in Figure 14 [53]. Epocore™ and Epoclad™ are used to build multi-mode optical waveguides that have a cross section of a square with 62.5 μm sides (core) (Figure 14). Other studies have used different materials for optical waveguides, such as polydimethylsiloxane (PDMS) [88][89] and SU-8 polymer [90].

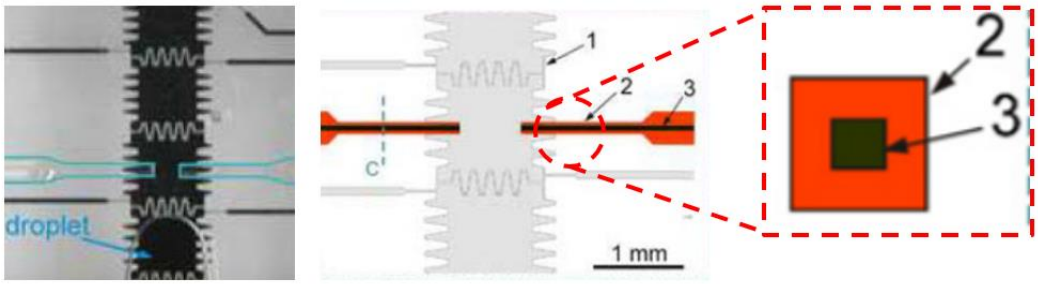

Figure 14: In-place optical fibers. Labeled numbers indicate: 1. actuation electrode, 2. waveguide cladding layers, and (3) waveguide core [53].

2.5 Conclusion

The main functions of the Lab-on-Chip (LoC) aerosol sensing system include collecting particulate matter, dissolving particulate matter and performing chemical reactions to generate a colored product and analyzing the absorbance. Section 2.1 introduced digital microfluidics as a method to control the liquid, and introduced the chip's planar layout (chip is divided into three parts: droplet dispense, aerosol collection, and colorimetric detection). The chip fabrication processes for the upper and lower plates were described. Section 2.2 analyzed the methods of aerosol collection and explained the method of impactor design based on traditional inertial impaction. Chapter 4 will introduce the prototype design of the impactor on the top plate. Section 2.3 described the detection methods of the three ions - sulfate, nitrate and ammonium, and three detection methods based on colorimetry with no toxicity, convenient operation, good linearity and limited limit of detection were selected.

Chapter 3 Core-shell droplet experiment

3.1 Transporting Droplets Across the Oil/Air Interface

The collection step mentioned before involves transporting droplets from silicone oil into air, and transporting them back from air into silicone oil. See overall description in Chapter 1. The reason for a two ambient system is that aerosol impaction has to be performed in a medium of flowing air while collection droplets are dispensed on the chip in silicone oil. Digital microfluidic systems typically use silicone oil, so that the droplet can be wrapped by a layer of oil film. The benefits of using oil are to prevent droplet evaporation, and to lubricate the insulator over which the droplet moves. After the aerosol collection is finished and the collection droplet is dispensed, the droplet first enters the air from the oil medium, scans across the impaction area, dissolves the collected aerosol, and then moves from the air to the oil medium, and mixes with other dispensed reagents. The resulting collection droplet is sent to the designated area for colorimetry detection of analytes. Thus, the collection droplet needs to pass through the oil/air interface twice. The transport process from oil to air is difficult. After the droplet enters an air medium, it will form an oil shell on the outside and will need to dissolve the collected aerosol in this core-shell form. Above the impaction area are the impactor nozzles, and it may be difficult for the droplet to pass underneath these holes. It is easier for the droplet to return from air to oil, which naturally happens when the droplet reaches the interface from the air side. This is because when a droplet is in contact with the oil medium, the oil-air interface is reduced, and the total interfacial free energy of the system is thus reduced.

3.1.1 Experimental results

A bare water droplet transported in an air medium quickly evaporates [91, 92] and is more difficult to actuate on an EWD chip [93] compared to a droplet in a silicone oil medium. However, a water droplet with an oil shell has been shown to actuate well and is suitable for impacted particle collection. Studies have shown that the actuation voltage of a water droplet in air (without oil shell) is 1.9-2.5 times [94] the voltage of a water droplet in ambient oil, while the actuation voltage of a droplet with oil shell is about the same as the voltage needed in an oil medium [95].

The most widely used technique to create a core-shell structure is to generate oil and water droplets separately and bring them together [95, 96, and 97] Silicone oil can be manipulated by dielectrophoresis at 250 V or above [97]. In most conditions, when a water droplet and oil droplet coalesce, the oil phase will spread around the water droplet until a complete shell is formed [95]. However, such a method brings in a new problem – the benefit of an oil shell in reducing the actuation voltage is lost, since the actuation voltage for dielectrophoresis is too high.

Thus, instead of creating droplets for separate phases, the approach adopted in this work was simply transporting a water droplet (dispensed completely in silicone oil) through an oil-to-air interface. It is helpful to notice that, as the droplet is pulled out from oil ambient, an oil shell is naturally formed. The only driving force is the electrowetting force, while two extra resistive forces are exerted on the droplet – surface tension introduced by increasing oil neck and Laplace pressure introduced by changing curvature, making it harder to activate the droplet at the interface. For this reason,

droplet dispensing must be done completely in the oil phase (away from oil-air interface), because it is much more difficult if the two resistive forces are also present. Since extra interfaces between oil and air are to be created across actuation electrodes, the electrowetting force must increase to catch and keep the droplet at the powered electrode side of the interface. Silicone oils with different viscosity (0.65 cSt, 1 cSt, and 2 cSt) were tested, and different channel widths that may result in different interface curvatures were also examined. It was found that both the channel width and the viscosity of the silicone oil medium barely influenced the resistive force during droplet transportation. However, the electrowetting actuation voltage must increase from 50 V to 80 V to overcome the silicon oil–air surface tension, and the movement is rather slow. Figure 15 shows the moments when a droplet passes through the interface across a series of electrodes. The droplet moves from left to right along the route of the electrodes. The left side of each picture is silicone oil, right side is air. When the droplet passes through the interface, it pushes the interface nearby forward as shown (figure a). As the droplet moves further, the local deformation of the interface forms a “bridge” between the silicone oil medium and the droplet (figure b – c). The farther the droplet moves, the longer and thinner the bridge. When the length of the bridge reaches three electrode lengths, it breaks from the thinnest point in the middle (figure d). Part of the bridge remains on the bottom plate in the air medium, and the air/oil interface changes back to a relaxed shape. A layer of oil film is automatically formed on the surface of the droplet, and this is shown with a thickened outline of the droplet (figure e).

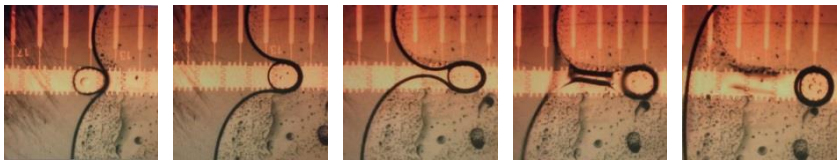

(a) (b) (c) (d) (e)

Figure 15: Water droplet pulled through the oil/air interface. The oil shell can be seen in the last picture. These five images from left to right show the different moments of the droplet crossing the interface.

3.1.2 Model of droplet resistive forces and velocity reduction

3.1.2.1 Laplace pressure from the curved interface

Initially, the oil/air interface prefers a large radius of curvature, as shown in Figure 15e. But when the droplet pushes the interface forward (Figure 15b, 15c), the curvatures of different sections of the interface become smaller.

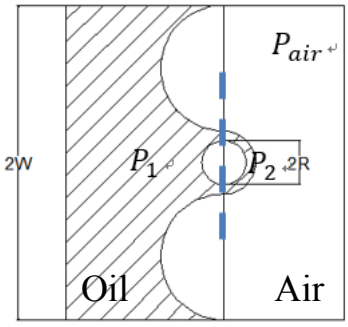

Figure 16: The shape of oil/air interface as the droplet exits the oil medium. This is a top view of the channel, the droplet is moving from left to right, left side (shaded area) is the oil medium, right side is air. Channel walls are not shown but should locate on the top and bottom sides of the picture.

Laplace pressure refers to the internal and external pressure difference of a surface [98]. This pressure difference is due to the surface tension at the air/liquid interface. From the Young-Laplace equation [30], the relationship of the pressure difference between the two sides of the curved interface and the curvature is

$$\begin{cases} P_1 = P_{air} - \gamma C_1 \\ P_2 - \gamma C_2 = P_{air} \end{cases} \quad (10)$$

P_1 is the pressure of the oil medium on the left side of the droplet, P_2 is the pressure of the oil medium on the right side of the droplet, C_1 is the concave curvature of the interface between the droplet and the channel wall, C_2 is the convex curvature of the part of the interface that protrudes due to the push of the droplet.

If the channel width is large and W indicates the distance from the droplet to a channel wall (as shown in Figure 16), then

$$\begin{cases} C_1 = \frac{1}{2(W-R)} \\ C_1 = \frac{1}{R} \end{cases} \quad (11)$$

The net pressure difference experienced by the droplet is

$$\begin{aligned} \Delta P &= [(P_2 - P_{air}) + (P_{air} - P_1)] \\ &= \gamma_{oil} * (C_1 + C_2) \\ &= \gamma_{oil}\left(\frac{1}{2(W-R)} + \frac{1}{R}\right) \end{aligned} \quad (12)$$

Integrating the net pressure over the right half of the droplet:

$$F_L = \int_0^{\pi/2} R\, d\theta\, h\, \Delta P \cos\theta = Rh\Delta P \quad (13)$$

This is the resistive force imposed by the oil/air interface on the droplet. The approximation is made where the left half of the droplet receives a uniform pressure

P_1 while the right half of the droplet receives P_2. This is a very rough approximation, and gives F_L an upper limit.

To calculate the actuation voltage which produces just enough electrowetting force to move the droplet across the interface, forces on the droplet are balanced:

3.1.2.2 Electrowetting force (Ren's actuation model [99])

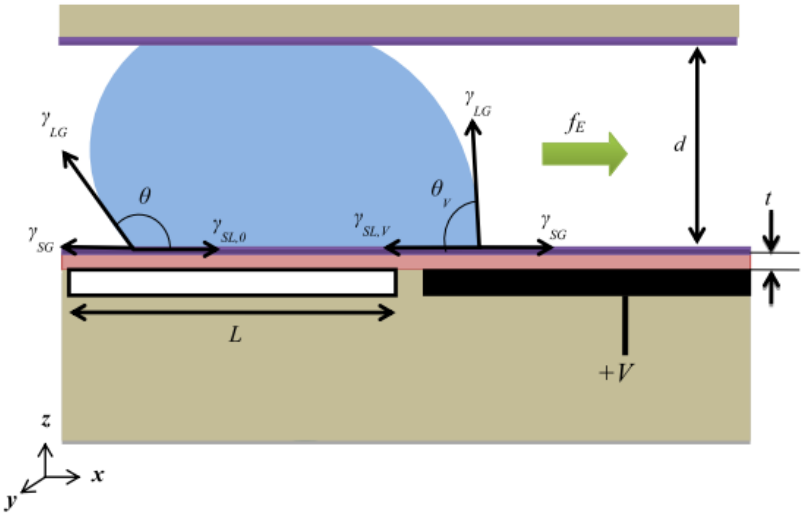

Figure 17: droplet actuation details with key angles and lengths

If the droplet is to be moved from left to right, the right electrode (black electrode in Figure 17) is activated by turning on the voltage, and the left electrode (white) is turned off. The contact angle where the droplet is in contact with the activated electrode ($\theta(V)$) is smaller than the contact angle where the electrode is turned off ($\theta(0)$). The net force added to the droplet is [94]

$$F_E = F_{Right} - F_{Left}$$

$$= \gamma_{lg}\cos(\theta(V) + \alpha) - \gamma_{lg}\cos(\theta(0) - \alpha)$$

$$= l_{eff}\left[\cos\alpha\frac{\varepsilon_r\varepsilon_0}{2t}V^2 - \gamma_{lg}\sin\alpha(\sin\theta_0 + \sin\theta_V)\right] \quad (14)$$

Integrating F_E over the contact line

$$= 2R\sin\varphi\left[\cos\alpha\frac{\varepsilon_r\varepsilon_0}{2t}V^2 - \gamma_{lg}\sin\alpha(\sin\theta_0 + \sin\theta_V)\right] \quad (15)$$

Where α is contact angle hysteresis, V is applied voltage between bottom and top plates on the activated electrode, θ_0 is initial contact angle $(V = 0)$, $\varepsilon_r\varepsilon_0$ is the dielectric constant of Parylene C, t is the dielectric layer thickness, γ_{lg} is the surface tension of water in silicone oil, l_{eff} is the effective length, φ is the angle indicating the extent of droplet and activated electrode overlap (Figure 18).

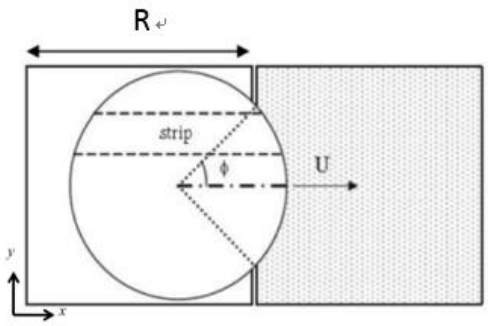

Figure 18: Angle φ indicating the extent of droplet and actuator electrode overlap

3.1.2.3 Friction drag force in oil medium (Beard and Pruppacher's classical drag model)

The assumption is that the droplet experiences the same drag force when it is away from the surface and when it is at the oil/air interface. The droplet experiences a drag force from the medium and drag forces from both plates. The drag force from the medium is [100]

$$F_D = C_D A_D \frac{1}{2} \rho_0 U^2 \quad (16)$$

C_D is the drag coefficient, A_D is the projected area of the droplet, ρ_0 is the droplet density, U is the droplet moving speed.

Reynold's number is defined as [98]

$$R_e = \frac{(2R)U\rho_0}{\mu} \quad (17)$$

Here R is the droplet radius, μ is the dynamic viscosity. When R_e is small [100]

$$C_D = 24/R_e \ . \quad (18)$$

By bringing the above two expressions into the formula of the drag force, $F_D = 6\pi R\mu U$

3.1.2.4 Shear stress between the droplet and the plates (model of Brzoska et al. [101])

This is the viscous drag force between the plate and the droplet, because when moving, the liquid inside the droplet will generate a velocity gradient. The force at the interface between the droplet and the plate is a result of the shear stress between laminar flows at different speeds inside the droplet, and it is [101]

$$F_V = 2U \frac{6\mu}{\theta_v} \ln\left(\frac{L}{a}\right) \quad (19)$$

Here θ_v is the contact angle at the activated electrode, L is the droplet diameter, a is a molecular size, and $\ln\left(\frac{L}{a}\right) \sim 10$ [101]

3.1.2.5 Force balance and the increase in actuation voltage

When the droplet is actuated, the electrowetting force and the resistive forces are

balanced:

$$F_D + F_V + F_L = F_E \qquad (20)$$

Since $F_D + F_V$ is a function of droplet velocity U, the equation can be written as:

$$kU + F_L = F_E \quad \text{or} \quad U = \frac{F_E - F_L}{k} \qquad (21)$$

When the droplet just starts to move from rest, the velocity is 0, and combining equations (12), (13), (15), (16), (19) and (21), the voltage applied is the threshold voltage V_T.

$$V_T = \sqrt{\frac{\left[h\gamma_{oil}\left(\frac{1}{2(W-R)}+\frac{1}{R}\right)\right]\frac{1}{2\sin\varphi}+\gamma_{lg}\sin\alpha(\sin\theta_0+\sin\theta_V)}{\cos\alpha\frac{\varepsilon_r\varepsilon_0}{2t}}} \qquad (22)$$

Constants used are: $\gamma_{lg} = 47\ \mathrm{mN/m}$, $\gamma_{oil} = 21\ \mathrm{mN/m}$, $\alpha = 4^{\circ}$, $\varepsilon_r\varepsilon_0 = 3.15 \cdot 8.85 \cdot 10^{-12}\mathrm{F/m}$, $t = 1.6 \cdot 10^{-3}$ mm, $\theta_0 = 110^{\circ}$, $\theta_v = 95^{\circ}$ (actuation contact angle) [102]. From experiment, h = 0.24mm, R = 0.5 mm. W is half channel width as in the calculation of F_L. The relationship of W and V_T is shown in Figure 19. It is important to check this relationship, because in the subsequent tests it was found that if the channel width was too small, the droplet was not able to break completely from the oil medium. Some oil stayed between the droplet and the gasket wall, and followed the droplet as it travelled through the air. Thus, it is better to make the channel wide (W>1cm).

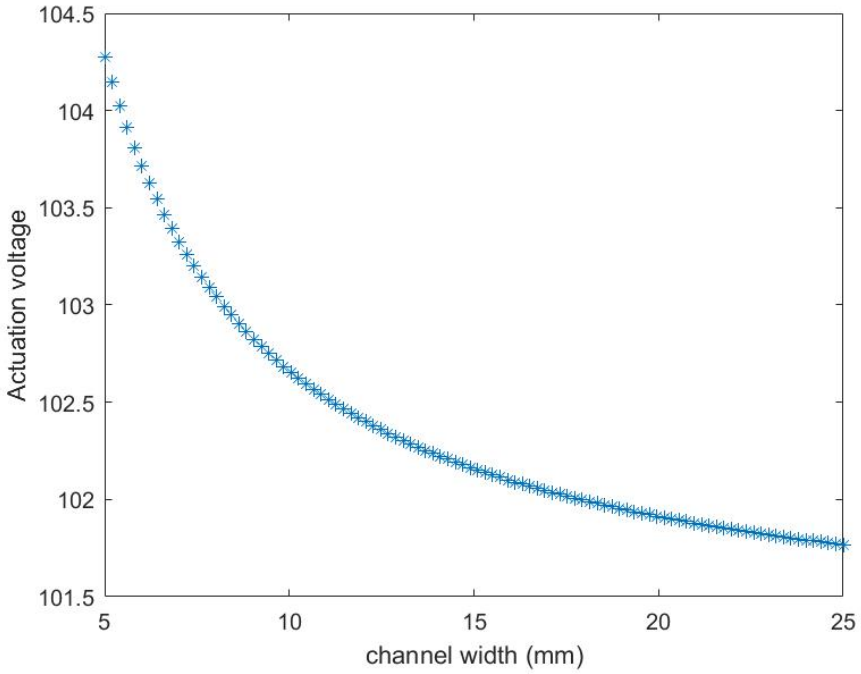

Figure 19: The change of V_T with respect to W is small

Although larger channel width helps lower the actuation voltage, but the voltage does not change much. Notice that the activation voltage without F_L is [94]

$$V_T = \sqrt{\frac{\gamma_{lg}\sin\alpha(\sin\theta_0+\sin\theta_V)}{\cos\alpha\frac{\varepsilon_r\varepsilon_0}{2t}}} \qquad (23)$$

and is about 33.1 V. However, the voltage required to transport a droplet across the oil/air interface based on this model is above 100 V. In the experiment, the minimum voltage to activate the droplet at the oil/air interface was 80V.

3.2 Droplet Scanning with Top Plate Openings

The impaction method has been tested on a digital microfluidic chip with a rectangular opening on the chip gasket layer with the inlet nozzle and the sidewall of the gasket as

the impaction plate [103]. Figure 20 (left) shows this early impactor design. However, the drawback to this approach was that the thickness of the gasket wall was an influential factor on collection efficiency, thus the choices of material and geometric design of the gasket were limited. Meanwhile, the scanning collection droplet does not contact all of the impaction plate, causing possible inefficient collection of particles. A better method is to have circular nozzles on the top plate and to use the bottom plate as the impaction plate. To guarantee smooth transport of a droplet under these circular impactor openings on the top plate and to avoid droplet pinning, the diameter of the nozzle must be small, and the nozzle walls have to be covered by a hydrophobic layer. With this design, the variables to be adjusted are the nozzle quantity, the nozzle diameter, the gasket thickness (which is the same as nozzle-to-impaction plate distance), and the flow rate.

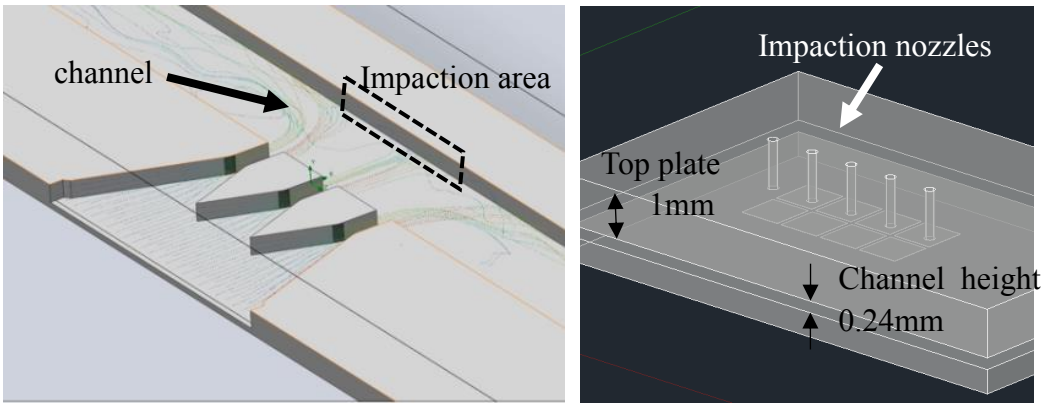

Figure 20: Impaction nozzles with different orientations. Left: Impaction nozzles in an early design were designed on the gasket layer, particles were impacted on the channel wall. There are three nozzles, each is 400 μm wide, the channel height is 280 μm, channel width is 1.5 mm. Right: Impaction nozzles designed on the top plate, and particles are impacted on the bottom of the chip. The eight squares are the electrodes in

the impaction area. The nozzle diameter is 0.241 mm, channel height is 0.24 mm, number of nozzles = 5. See Chapter 4.1 for specific dimensions and calculations.

3.2.1 Making top plate openings

To observe the movement of the droplet in the channel, and to measure the absorbance of the droplet in the vertical direction, the top plate must use a transparent material. The transparent, hard materials that are commonly used in microfluidics are glass or plastics. On the top plate, both the fluid injection holes above the reservoir and the impact nozzles should be made. However, it is difficult to drill holes of millimeters to nanometers on glass, since the glass is brittle and prone to cracks. The results of using CNC drilling, wet etching methods to make holes on glass will be explained below.

Commonly used glass fine drilling technology include laser cutting and wet etching. Laser cutting on glass (Fusion M2 60W CO_2 laser, Duke University Colab) was attempted, but since glass was too brittle, cracks could not be avoided. A solid-state laser with a galvanometer can make micro pores on glass and ceramics, but the cost is high. In later experiments, the chip often fails to perform electrowetting operations stably for various reasons. It would be better if the chip could be disassembled so the top plate could be reused. However, the gasket material is difficult to clean in physical or chemical ways while keeping the CYTOP and ITO layers in good condition, thus the top plate cannot be reused, making it not worthwhile to use expensive laser cutting on top plates.

For wet etching, borosilicate glass (Borofloat 33 from UniversityWafer, Inc, 500 μm

thick) and fused silica glass (UniversityWafer, Inc, 100 μm) have been tested using 49% HF solution as etchant and different masks. However, the etching rate was slow with the borosilicate glass, and it was possible to etch only about 100 μm before etching mask failure (amorphous silicon, or a combination of Cr/Au/Cr/Au), and even that would take a few hours. A top plate of 100 μm was too thin and not easy to handle, and was likely to break under the pressure drop in the airflow. For the silica wafers, the etch rate was good, but the etched holes had rough edges. Because wet etching is isotropic, even with lower HF concentration and slower etching rate, the edge of the etched holes was rough if it was desired to achieve deeper etching. Rough surfaces and edges can cause uneven coating of the hydrophobic film layer and the droplets may stop moving as they try to cross the impaction holes.

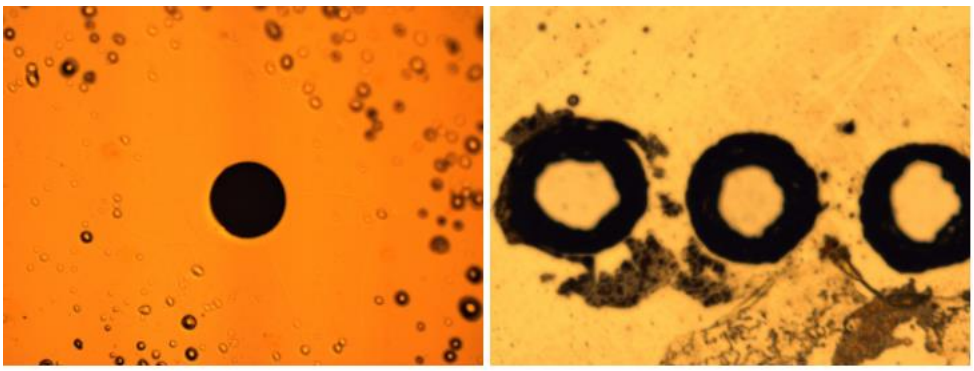

Figure 21: Chemical etching of glass holes. Left: an etched hole with 0.2 mm diameter and 100 μm depth; right: 500 μm thick glass etched all the way through

Since the methods of making holes on glass were not satisfactory, in the subsequent experiments, acrylic plates were used for the top plates. The problem with acrylic is

that the coefficient of thermal expansion is about ten times larger than glass, which makes the deposited ITO layer prone to cracks. Also, the acrylic will warp or even melt above 50℃, so the CYTOP layer cannot be baked above 190℃ as required, and the CYTOP is not resistant to corrosive chemicals or strong acid and alkali chemicals. However, since holes into acrylic can be drilled in the CNC machine with smooth edges and vertical walls, the collection efficiency of aerosol impacted particles will be better than using the glass top plate, and the edge of the hole will not pin the droplet as it passes under the hole.

3.2.2 Droplet scanning test

The nozzle openings on the top plate are circular with a diameter equal to 0.24 mm, which is about 1/3 of the EWD actuation electrode pitch. These openings serve as the impactor nozzles, and the aerosols are expected to deposit directly onto the CYTOP surface right under these openings. Figure 22 shows the position of the collection nozzles on the top plate and collection areas under the nozzles (left) and an ambient aerosol deposition pattern at the impaction area (right). The top plate is the ground plate during electrowetting, and having these openings may make the ground plate discontinuous and cause potential problems with electrowetting. After about ten droplets passed over the impaction area, it has been clearly shown that the loss of ground plate area greatly reduces the electrowetting force. In the meantime, two additional resistive forces were introduced: one was from the roughness of the edge of the holes and another was a result of the higher pressure in the droplet as it tended to

push the liquid upward through the nozzle holes.

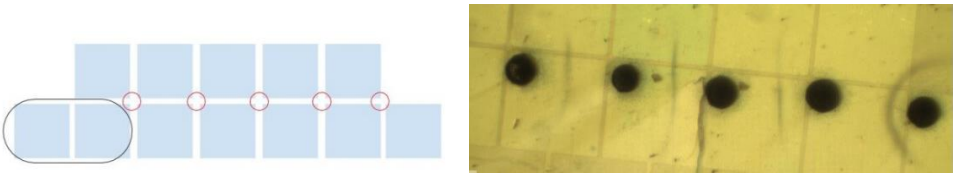

Figure 22: Aerosol impaction areas. Left: The impaction area is composed of ten electrodes arranged in two rows. A droplet covers two electrodes. Right: Deposited aerosol particles on the CYTOP surface covering the actuation electrodes.

Due to these difficulties, the negative effect of the holes is minimized when the area of the hole is only a small portion of the total electrowetting electrode area, and the position of the hole is not right on top of the electrode, but is offset from the electrode centers. Since droplet size is always slightly larger than the electrode, the edge of the droplet will swipe through the deposition area and collect deposited material. In addition, the droplet diameter covers two electrodes instead of just one electrode. This larger droplet has a larger contact area with the ground plate, and the loss of ground plate due to the holes does not have an effect as significant as that which a smaller droplet experiences. The arrangement of electrodes and impaction nozzles are shown in Figure 22 (left). The impaction nozzles are in the middle between two rows of electrodes, and by moving the droplet back and forth around these ten electrodes, the whole impaction area can be thoroughly scanned. The collection efficiency is unknown at this time because the chip was not weighed and there was undissolvable aerosol not collected.

Figure 23 shows the droplet moving under the nozzles across the impaction area. The droplet moved smoothly through an electrode array from right to left, and when passing through the top plate openings, the droplet covered the area underneath the hole (e.g. figure c). In figure d, the oil shell of the droplet was slightly stuck at the edge of the passed hole, but managed to move forward without activation voltage increasing.

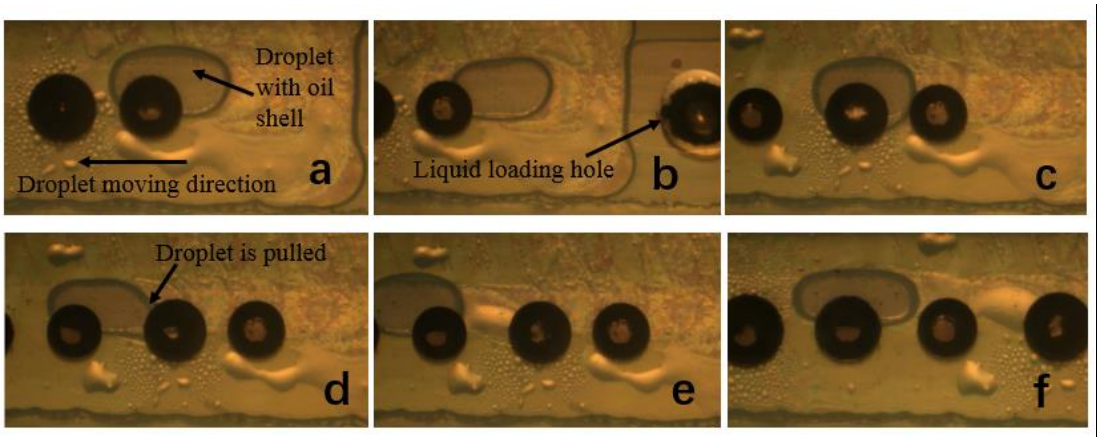

Figure 23: Water droplet with oil shell transported under impaction nozzles in air.

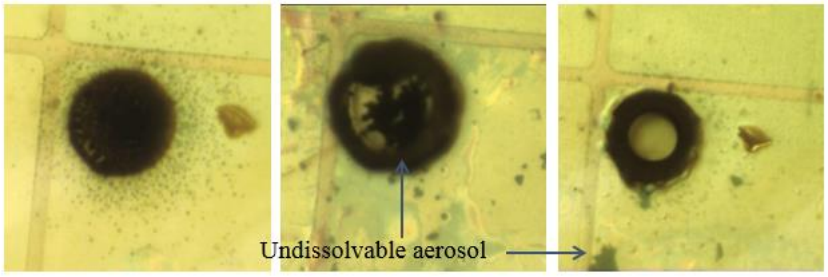

Figure 24: Collection of deposited aerosols.

Attempts to collect and dissolve outdoor particulate matter were carried out in the Dessert Research Institute (DRI) in Reno, NV, during Oct.15 – Oct.19, 2016. Four of

the chips collected ambient aerosols from the roof top of DRI for 12 hours. More details of the design of the aerosol impaction system is found in Chapter 4.

Figure 24 shows the collection of deposited aerosols. The left picture was taken before droplet scanning. The black dots were aerosol collected. The middle picture was taken after first droplet scanning, and the nozzle was clear except some black unsolvable particles. Most of these particles are expected to be carbonaceous aerosols. The picture on the right was taken after second droplet scanning. The nozzle was clear, which means all the aerosols were gone. However, the undissolvable aerosols was simply driven away by the water droplet, but not dissolved. Because residue other than soluble salts were present, it was expected that there were also elemental and black carbon deposits, each consisting of 10-30% of total aerosol mass [2]. The collection time was 12 hours, and the chip was purposefully overloaded. The reason was to make sure enough aerosols could be collected and to test if the excessive aerosol would hinder droplet movement or cause droplet pinning, which did not occur. The scanning droplets were collected with a pipette at the reservoir and diluted for ion chromatography testing. However, the concentration of sulfate was too low to be detected. The reason likely is that the concentration of sulfate in air was much lower than expected, and the chip reached collection saturation before a sufficient amount of sulfate was deposited.

Overloading may be due to 1) there is a significant quantity of particles in the air with large diameters, 2) particles due to air humidity and surface properties, are easy to adsorb onto each other, forming aggregates on the impact plate and blocking the air passage. For these two reasons, to study aerosol collection efficiency on the chip, lab-

generated dry aerosol of ammonium sulfate was used. A collection efficiency of 96% was obtained, and a closer look at the process and results can be found in Chapter 4.2. The problem of collecting airborne particulate matter directly from the natural environment may be solved with a filter that can be used to control the maximum particle diameter, or passing the air through a cascade impactor first, and recovering only the particulate matter on the first level impactor plate which collects the smallest particles.

3.3 Conclusion

This chapter focuses on the process that uses a droplet to extract the deposit on a digital microfluidic chip. After the impactor on the upper plate of the microfluidic chip collects the aerosol, the aerosol is deposited on the bottom plate surface. The steps include: dispense the collection droplet in an oil phase, transport the droplet into an air phase, move the droplet around to completely scan the collection area (under impactor nozzles), and then move the droplet back to an oil phase for colorimetric measurement of collected analytes.

Because the droplet changes the curvature of the oil/air interface during its moving from oil medium to air medium, there is an additional Laplace pressure pulling against it from this curved interface, making it difficult for the droplet to cross the oil/air interface to the air from the oil phase. Thus, the activation voltage needs to be increased (actual measured value increased from 50V to 80V). When the droplet leaves the oil phase, an

oil shell is formed on the outside of the droplet, which is helpful for the movement of the droplet in the air medium.

When the droplet scans the impaction area, since the upper plate has impactor nozzles, it is not a complete ground plate. If the droplet is located directly below one of the openings, it will escape from the opening because the pressure at the missing portion of the top plate is lower than the internal pressure of the channel. Therefore, the openings and the electrodes in the impaction area are designed to be misaligned, so that most of the surface area of a droplet is still in contact with the top and bottom plates, and only a small part of the liquid is directly under the top plate opening, ensuring that the electrowetting force is large enough to prevent the droplet from escaping from the holes or being pinned at the holes. It is also very important that the edges of the holes are smooth and infiltrated with CYTOP so that the walls of the holes are also hydrophobic, and the droplet can easily move across the impaction area.

Chapter 4 Impactor efficiency test

4.1 Design of digital microfluidics impactor

An inertial impactor was designed following Marple and Rubow's rules [46]. The constraint of Re is 500-3000 to make equation $d_{50} = \left[\frac{9\pi\eta L^3(Stk_{50})}{4\rho Q}\right]^{\frac{1}{2}}$ valid. The top plate had its impactor nozzles made by a drill press. The drill size was #88 and the diameter was 0.2413 mm. This was the smallest drill bit available at Duke. According to the definition of Reynolds number,

$$Re = \frac{\rho L v}{\eta} = \frac{4\rho Q}{\eta \pi L n} \qquad (24)$$

where ρ is the air density, v is the airflow velocity at the end of the nozzle, L is the diameter of circular nozzles or the width of rectangular nozzles, η is the viscosity of air, and Q is the flow rate, n is the number of nozzles. With n=5, Re is calculated to be 1954.

It is worth checking the criteria mentioned in chapter 2 to make an effective aerosol impactor. If the nozzle diameter is L, the distance between nozzle end and impaction plate S, and the nozzle length T, we have L=0.241mm, S=0.24mm, T=1mm. S/L ~1, T/L>1, and Re = 1954. The cutoff diameter d_{50} is calculated to be 0.113 μm. The target inorganic aerosol diameters are 0.08-1 μm as shown in Figure 1. All criteria were satisfied.

4.2 Ammonium sulfate aerosol collection

To evaluate the collection efficiency of the impactor design and to check the deposition pattern on the bottom plate, a chip-to-world chamber was designed. The chamber had

two parts, both made with aluminum. The top part had an inlet from the top and two lateral outlets on both sides. The inlet and outlets were designed to fit 1/4-inch polyurethane tubing. The top inlet was designed to be directly above the impaction area of the chip after the chip was placed in the holder, and the two parts were held together with four screws. The airtightness was guaranteed by O-rings and was tested by placing the box in water. For each aerosol collection experiment, a chip was placed inside this chamber box. When the collection step finished, the chip was taken out to the electrowetting chip setup for aerosol extraction.

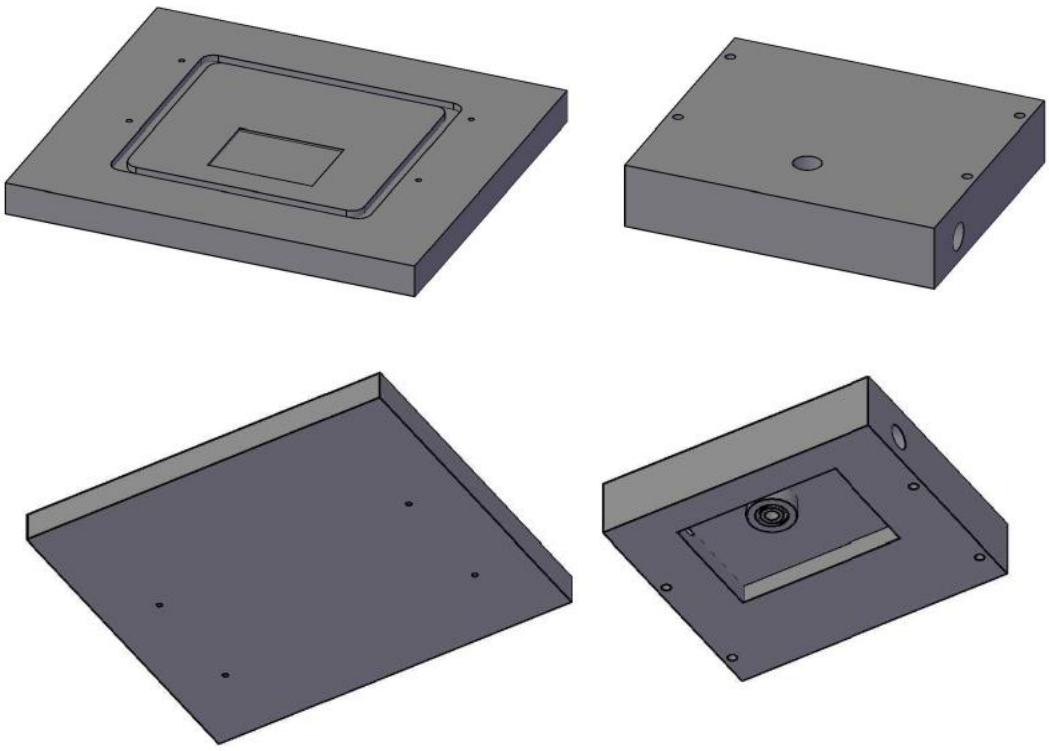

Figure 25: Chip-to-world Chamber. Left two figures: two views of the bottom piece of the chamber. The rectangular slot in the middle is designed to fit the 500 μm thick bottom plate of the chip. Right two figures: two views of the top piece of the chamber.

The position of the circular nozzle in the middle matches the impaction nozzles on the top plate of the chip.

In addition, an aerosol generator and collector system were used that included an atomizer for generating ammonium sulfate aerosols, a differential mobility analyzer (DMA) and condensation particle counter (CPC), and an oil-less pump (Welch Vacuum 2014B-01) that was adjustable in flow rate (0-2 L/min in experiments). The airflow is shown in the following diagram. First, switch 1 was closed for all directions and switch 2 was open, and ambient air through a filter was pumped through the chip to purge any interfering particles that may have deposited during the setup (Polyurethane(PU) tubing for example). Then switch 2 was closed, and switch 1 was turned in the direction to allow aerosols from the aerosol generator to flow directly to the particle counter. At this time, none of the particles propagated through the chip. Then switch 1 was switched to measure the aerosols that came out of the chip. The difference of these two measurements was the aerosol concentrations deposited on to the chip.

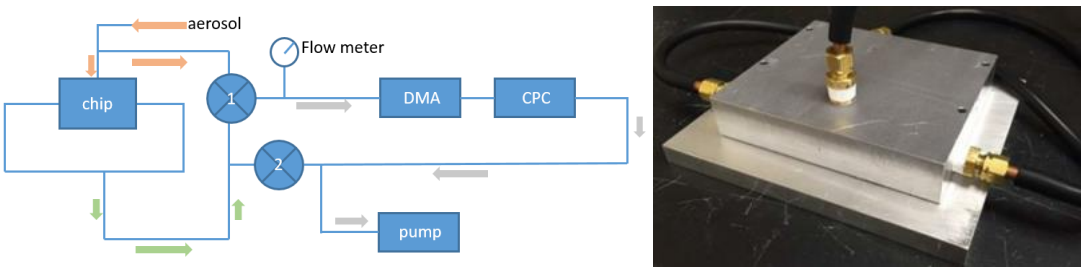

Figure 26: The diagram of aerosol collection test

Three different flow rates were tested: 1L/min, 1.5L/min and 2L/min, and 1L/min was

repeated. For every test a new chip was used. There was not a significant difference in collection efficiency. The cutoff size for 50% efficiency was less than 100 nm (66.1 nm ad 55.2 nm) for flow rates greater than 1L/min and slightly larger than 100 nm (105.5 nm and 109.4 nm) for a flow rate 1L/min. This cutoff size agrees with the theoretical calculations, and 1L/min was a suitable flow rate. The pressure drops between the inlet nozzles and the outlet were measured to be 0.037 atm, 0.086 atm and 0.111 atm for flow rates 1L/min, 1.5L/min and 2L/min. If aerosol collection was repeated without cleaning the chip, then the collection efficiency would increase due to particle overloading. In fact, 1 minute of collection time would be enough. Overloading would cause significant increase in pressure drop, which means less efficiency of the pump.

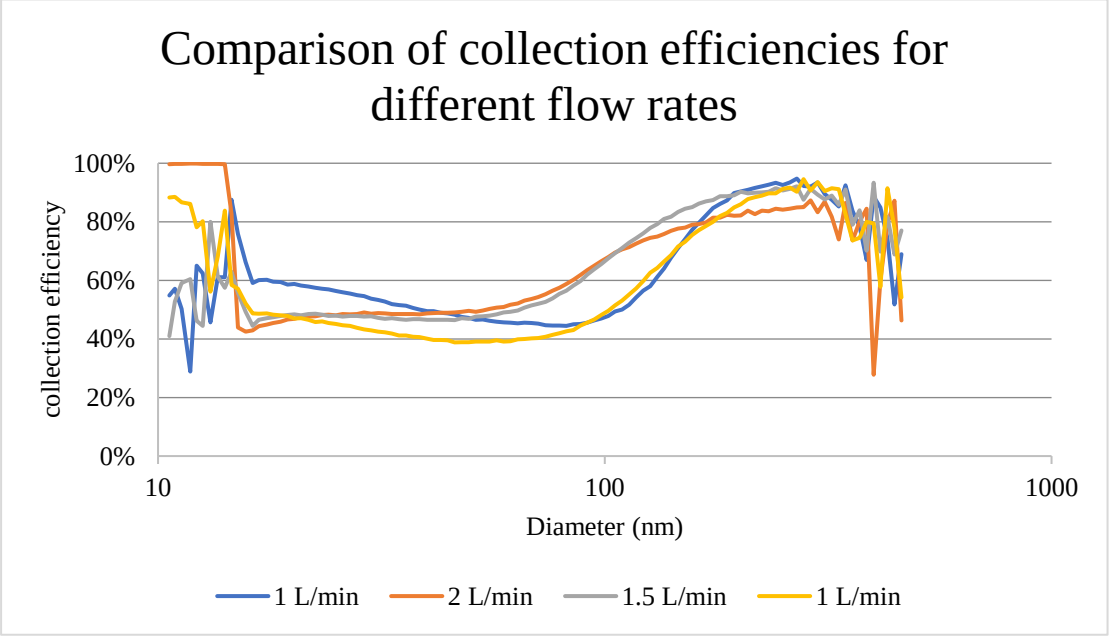

Figure 27: Collection efficiency as a function of particle diameter for four different flow rates.

The collected aerosol particles formed separate white deposits directly under the five top plate openings. These deposits were distributed with equal distances across six electrodes. After aerosol collection, the chip was carefully removed from the chamber box and transported to the electrowetting station for aerosol extraction. The aerosol particles would be collected by scanning a droplet by electrowetting over the collection area to dissolve the impacted particles. The droplet would scan the impaction area twice. For this experiment, a deionized water droplet was used to dissolve these aerosols, and then the droplet was collected by pipette at the reservoir openings. The collected droplet was dissolved in 4ml of DI water and sent for analysis using ion chromatography. Some of the silicone oil that surrounded the water droplet might be collected together with the droplet, thus the samples collected from the ports were further treated to remove silicone oil. Samples were sent to the Desert Research Institute[1] where silicone oil removal and ion chromatography tests were done. In addition to this main collection area, some of the particles were also deposited above the top plate or in the O-ring grove, and those areas were washed with deionized water. The sulfate concentrations in these samples were measured with ion chromatography, too. In this way, the aerosol collection was performed on four chips, each collection time was 2 minutes (which is also the time required for CPC to do a particle size scanning). It was found that $96 \pm 5.9\%$ of the total deposited aerosol was inside the chip and collected by droplets. Here, both impaction efficiency and droplet collection efficiency were considered.

[1] The study is a continuation of an NSF-funded project in collaboration with Desert Research Institute (DRI). Ambient aerosol collection, lab-generated aerosol collection and ion chromatography were done at the DRI Reno Campus, Nevada.

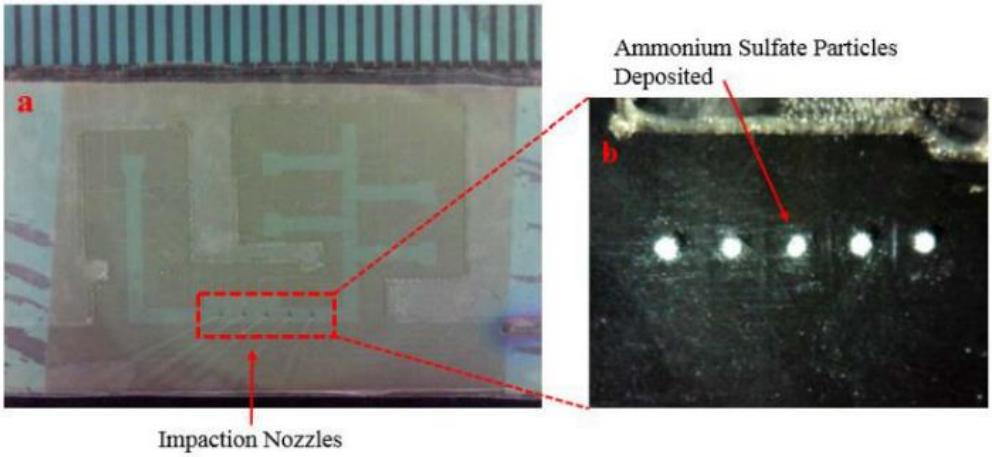

Figure 28: Impaction nozzles and lab-generated aerosol collection. Left: the five impaction nozzles. Right: top plate is removed, and the lab-generated sulfate aerosol particles deposited directly under the impaction nozzles can be seen.

4.3 Conclusion

Following the artificial inertial impactor design method of Marple and Rubow, five impaction nozzles were designed on the upper plate. The physical dimensions related to nozzles were: single nozzle diameter is 0.241 mm, channel height (nozzle-to-plate distance) is 0.24 mm, and the throat-length diameter is 1 mm. The cut-off diameter of aerosol particles (50% collection efficiency) is 0.113 μm. For an air flow rate of 1.3L/min, the inlet-to-outlet pressure drop is 0.037 atm. Because the impactor nozzle and the channel are very small and cannot be directly connected to the pump, a chip-to-world chamber was designed. The air inlet of the chamber faces the impactor nozzles on chip, and the two outlets on the left and right side of the chamber faced the outlets of the air flow path of the chip channel. Both the inlet and the outlet of the chamber

could be connected to a 1/4 inch tube. Using this chamber for lab-generated sulfate aerosol collection experiments, it was found that the white powdered aerosol was deposited just below the impaction nozzle. After collecting the aerosol deposited in the channel with a scanned droplet and the aerosol deposited outside of the channel (above the top plate and in O-ring groves) with deionized water, the samples were sent for an ion chromatography test. Results shows that $96 \pm 5.9\%$ of the aerosol was effectively collected inside the channel.

Chapter 5 Colorimetric Assay Experiments

In this chapter, all three colorimetric tests were performed on a Tecan multimode plate reader spectrometer (infinite 200Pro) to verify that the chemistry to form the final colored solutions was as expected, and the measured concentration range was within the allowed range of Beer's Law. In other words, based on analyte absorption measurements it was necessary to determine if a linear relationship existed between absorbance and the concentration of each analyte. For situations where the linearity was acceptable, more concentration points were introduced for a specific range.

Two testing procedures were performed according to the colorimetric experimental methods described in Section 2.3. Off-chip testing used the product color solutions obtained in 1.5ml tubes (analytes of six concentrations were used in each experiment, repeated several times). 200 μL of each solution was filled into a well plate and the absorbance was measured with a plate reader. To ensure the stability of the product absorbance, these solutions were repeatedly measured at 12, 24, and 48 hours after the reaction to detect fading.

On-chip tests for the three analytes were performed on chip, and the results were compared with the Tecan plate reader results. Absorbance experiments were performed on a digital microfluidics chip using the final product solutions from the well plate experiment. The first testing approach was to build two aligned fibers in the vertical direction of the chip as the light in and out paths. This test approach proved to be incapable of stably measuring the absorbance of the droplet. The reason will be explained later. After that, the fibers were changed to test in the horizontal direction,

whereby two fibers were sandwiched between the upper and lower plates of the chip. Horizontal measurements were compared with vertical measurements, and the latter were found to return more consistent measurement results. The lowest concentration tests were repeated 50 times for each assay, and the standard deviations in absorbance were calculated to find the limit of detection concentration. Limit of detection in this study is calculated from standard deviations and linear regression slopes: 3× standard deviation of the lowest concentration / slope of the linear fit.

5.1 Validation of Detection Chemistries with Benchtop Methods

The three colorimetric tests described in Chapter 2 include the sulfate-barium-MTB color reaction, the ammonium-OPA-sulfite fluorescence reaction (where absorbance is measured instead of the fluorescence intensity), and the nitrate reduction and Griess test (detection of nitrite) were performed with traditional off-chip chemistry methods. The absorption spectrum of the final solution and the absorption intensity of the absorption peak wavelength were measured. In the ammonium and nitrate experiments, the absorption peak wavelength of the final solution is different from those of the reactants, thus good linearity can be obtained for each measurement. However, in the sulfate experiment, the absorption peak of the MTB-Ba complex coincides with the absorption peak of uncomplexed MTB at the same pH, but the absorption coefficients are different. Thus, although the linear relationship between sulfate concentration and absorbance can be detected, it is greatly affected by error. The stability of absorbance over time was later measured. The interfering ions of these three colorimetric reactions have been

thoroughly studied previously in the literature and there is no need to specifically design a test here. The interference of these three ions among themselves will be described later.

5.1.1 Plate reader results for all three tests

Tecan Infinite 200 Pro plate reader (in You lab, Duke Biomedical Engineering) was used for absorbance measurement. Wavelength scans in the visible light wavelength range (300-900 nm) were done for each sample. 96 Flat Bottom Transparent Polystyrene well plates were used, and each well was filled with 200 μL analyte liquid. Six different concentrations of standards were chosen nonuniformly for each assay, the concentrations are listed below.

sulfate stock solution :120 ppm						
nitrate stock solution: 44 ppm						
ammonium stock solution: 15 ppm						
solution #	stock solution (μL)	DI water(μL)	dilution factor	final sulfate (ppm)	final nitrate (ppm)	final ammonium (ppm)
1	1000	0	1	120	44	15
2	750	250	0.75	90	33	11.25
3	500	500	0.5	60	22	7.5
4	250	750	0.25	30	11	3.75
5	100	900	0.1	12	4.4	1.5
6	50	950	0.05	6	2.2	0.75

Table 1: The dilution ratio and concentrations of standard solutions

5.1.1.1 Sulfate

First, the peak absorption wavelengths of complexed and uncomplexed MTB (as

described in Section 2.3.1) were verified by measuring uncomplexed MTB and complexed MTB samples with the spectrometer. The uncomplexed MTB was made by dissolving MTB powder in DI water (250 mg in 1L, then diluted 100 times to 2.5 ppm). Uncomplexed MTB is a reactant in the sulfate detection test, and the absorption spectrum should be distinguished from the absorption spectrum of the product. To obtain a steeper slope in the concentration-absorbance plot, several experiments were performed, however, it was found that something in the final solution other than MTB-Ba was absorbing at 610nm.

The concentration of uncomplexed MTB used in the first mixed solution was 25 μmol or 2.5 ppm, with pH = 7, and showed a yellow color. The concentration was adjusted and set to 2.5 ppm due to the range of the Tecan spectrometer and its ~0.4 cm light path from the fill of plate wells. Higher concentrations (listed in Table 1) were later used for on-chip tests because the light path length of the chip equals to the gasket height, which was about 0.24 mm. The absorption spectrum is shown in Figure 29. The peak absorption is at 440 nm (it is close to the 460 nm peak absorption wavelength in literature).

Then barium chloride (72.3mg in previously 1L MTB solution, then diluted 100 times) was added to the previous solution of uncomplexed MTB. MTB and barium now coexisted in solution. They should form uncomplexed ions in an acidic environment and would become an MTB-Ba complex in an alkaline environment. The wavelengths of the solution at different pH values were obtained. The concentration of barium was the same with the concentration of MTB, in order to form a solution of 1:1 Ba-MTB

complex. Then a tiny amount (about 1% of the total volume) of 1M HCl was added to reduce its pH. At this point, MTB and Ba should not be able to form a complex. This means the absorption peak should be at the same wavelength of 440 nm (as if barium is not in the solution), which ensures that if sulfate concentration is to be measured, then sulfate that was to be introduced in the next step will combine with free barium ions without being interfered by MTB. The final solution was orange, and the absorption spectrum is shown in Figure 29.

An excess amount of 1M sodium hydroxide then was added to the solution. The solution turned blue right away. This means the MTB and barium formed a complex, and the wavelength of the peak absorption changed from 440 nm to 610 nm.

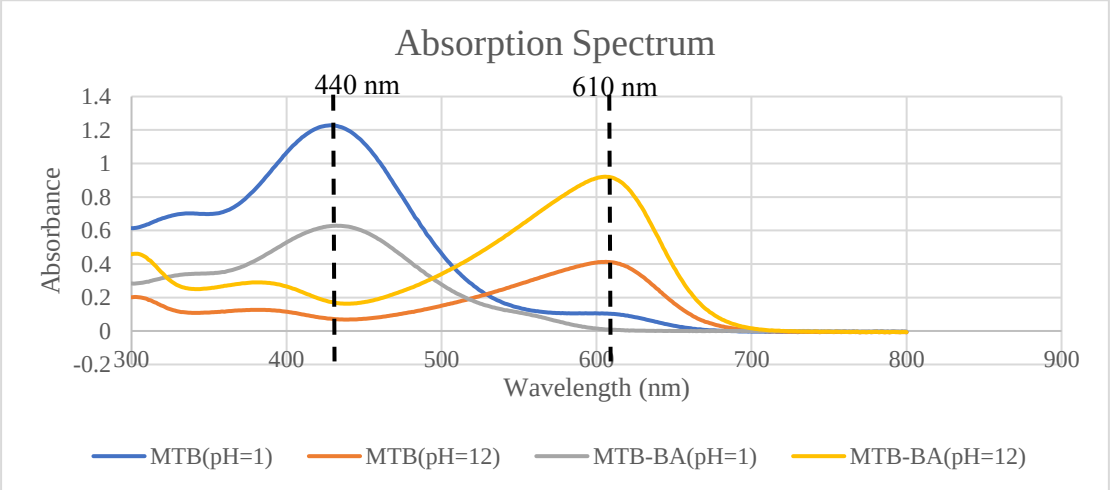

Figure 29: The absorption spectrum of uncomplexed MTB and MTB-Ba with different pH values. Uncomplexed MTB (blue, orange) and MTB-Ba complex (grey, yellow) have the same peak absorption wavelength at certain pH values (440 nm when pH=1, 610 nm when pH=12).

Theoretically, if sulfate ions use barium ions to form barium sulfate precipitation, then less MTB-Ba complex will form, and the absorbance should decrease with sulfate concentration in the sample. In the literature, uncomplexed MTB should have a grey color [104], although its absorbance wavelength was not reported. However, uncomplexed MTB with pH = 12 was scanned with a spectrometer, and it too showed a blueish color with an absorption peak at $\lambda = 610$nm. It is proved that the complexed MTB and uncomplexed MTB have the same absorption peak in basic conditions. Previous studies do not have information about the interference of uncomplexed MTB when measuring MTB-Ba. It is postulated that uncomplexed MTB has a smaller extinction coefficient than MTB-Ba. Even though uncomplexed MTB is positively related to sulfate concentration and thus absorbance, the sum of the absorbance due to both uncomplexed MTB and complexed MTB will still show a linear relationship with sulfate concentration but with a negative coefficient, because complexed MTB, which has a larger extinction coefficient, is negatively related to sulfate concentration. However, this means that the range of absorbance from the lowest concentration of sulfate to the highest concentration is small, and the absorbance does not change much with different concentrations of sulfate. The absorbance is more dependent on the total amount of MTB used and will vary slightly based on the MTB-Ba complex concentration in the solution. When the final mixed solution contains 1 mM MTB and 0.68 mM barium and detects 0 – 0.63 mM sulfate, sulfate with the highest ion concentration forms precipitation with almost all barium ions. At this time, the concentration of the MTB-Ba complex is almost zero. The absorbance range obtained

is about 0-0.1. When the concentration of MTB, barium, and sulfate is increased by 10 times, the highest concentration of sulfate still makes the concentration of MTB-Ba close to zero, but the obtained absorbance range is 0.8 – 0.9, not 0 – 0.9. This is because the MTB-Ba complex has the same absorption peak as the umcomplexed MTB, so even when the range of the sulfate concentration is increased, the range of absorbance is still 0.1.

It was noticed during subsequent on-chip tests that the droplet that contained the final solution shrinks in silicone oil. Thus, plate reader results with different alcohol as the primary solvent should be compared. Here the droplet shrinking is briefly mentioned before the discussion of plate reader results. Silicone oil is DMS-T00-100GM purchased from Gelest Inc. and the droplet contained 70% ethanol. The loss of droplet volume was probably because ethanol dissolves in silicone oil. In earlier studies, ethanol was used as the solvent to intensify the color product, and was reported to achieve higher sensitivity. According to Madsen and Murphy [67], the higher the concentration, the better the sensitivity.

To solve this problem, methanol was tried as a substitute. In fact, McSwain [105] had demonstrated methanol as the solvent for the MTB test. 100% and 80% ethanol and methanol droplets were tested. As soon as the chip reservoir was filled, a droplet was dispensed, and a photo was taken. After 15 seconds, a second picture was taken. This procedure was done on all four different droplets with different concentrations of ethanol or methanol. The only solute in the droplets was food coloring to enhance the photos.

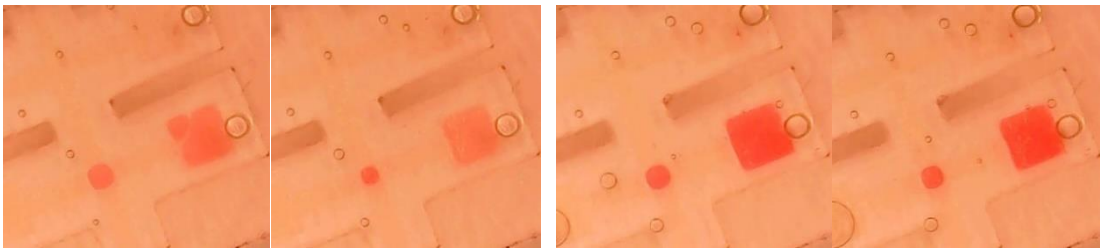

Figure 30: Ethanol droplet shrinking in silicone oil. Left two figures: 100% ethanol droplet shrinks in silicone oil. Right two figures: 80% ethanol droplet shrinks in silicone oil.

From Figures 30, 32 and 33, it is obvious that 100% ethanol droplets shrank dramatically. In fact, the droplets became too small over time to overlap with adjacent actuation electrodes, thus preventing actuation to the next activated electrode. The 80% droplet did not shrink as much, but it can be seen that the volume of both the droplet and the liquid in the reservoir was less over the test time. If the contents of the droplet are replaced by methanol, in Figures 31, 32 and 33, the 100% methanol droplet also experienced a volume reduction (10%) in 15 seconds, but the volume of 80% methanol is not substantially reduced in a few minutes, while 80% ethanol was reduced to 60% of its original volume at 6 minutes.

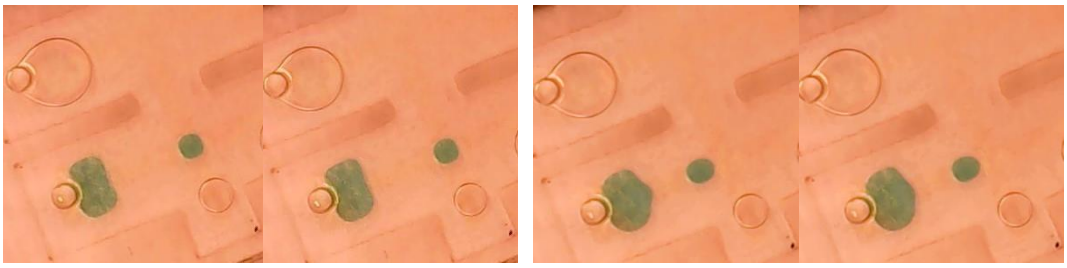

Figure 31: Methanol droplet shrinking in silicone oil. Left two figures: 100% methanol droplet shrinks in silicone oil. Right two figures: 80% methanol droplet shrinks in silicone oil.

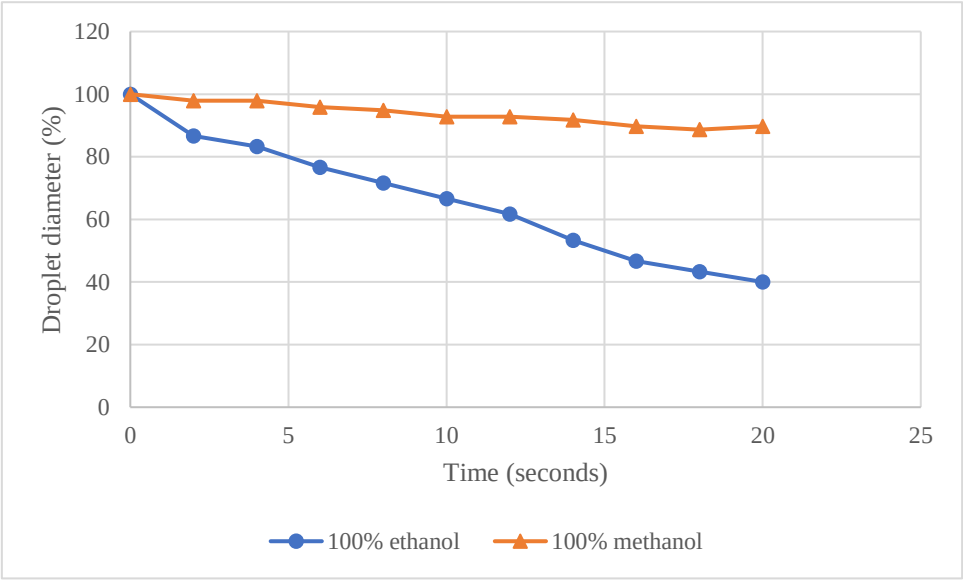

Figure 32: The diameters of 100% ethanol and 100% methanol droplets in silicone oil over time. The diameter of the droplet is represented as the percentage of the droplet diameter at time = 0.

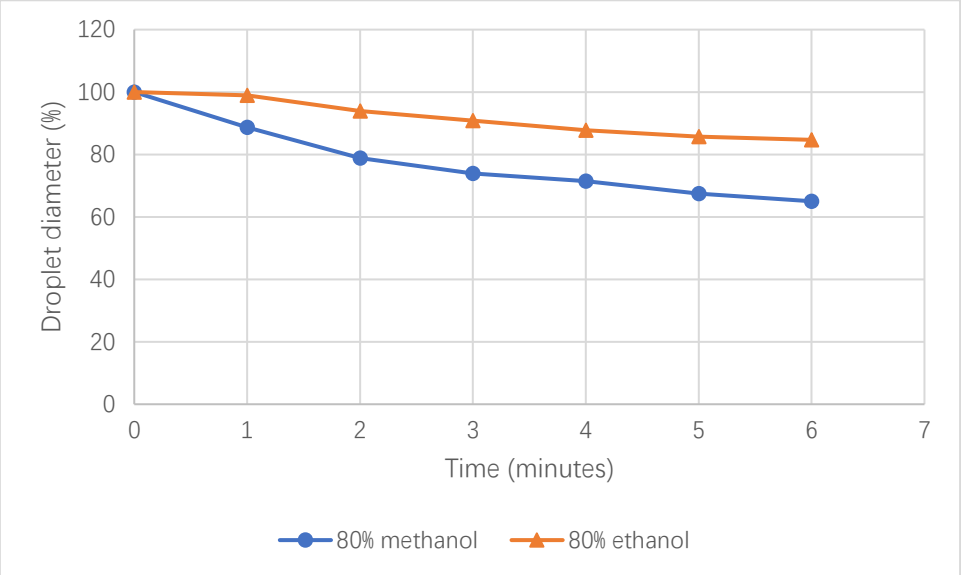

Figure 33: The diameters of 80% ethanol and 80% methanol droplets in silicone oil over time. The diameter of the droplet is represented as the percentage of the droplet diameter at time = 0. Because these droplets are more diluted, they shrink slower than 100% ethanol and methanol. The time unit of measurement is minute.

To study the effect of solvents on sensitivity of absorbance to MTB-Ba complex , methanol and ethanol containing droplets were compared. 70% ethanol and methanol were used as the solvent for the MTB test. Six concentrations of sulfate were studied as listed in Table 1, and the solutions were diluted with 70% methanol to 1/4 of its original concentration before they were filled into the Tecan plate reader for absorbance measurement. The dilution step was required to make the absorbance not too high, but fall into the measurable range of the Tecan plate reader. The same six concentrations of sulfate would also be used for on-chip test later without dilution, because using higher concentration could make the light absorption not too low while the light path length is much shorter on chip. Sulfate standard solutions were added to the acidic MTB-Ba

solution and mixed thoroughly before sodium hydroxide solution was added. The results are plotted in Figure 34.

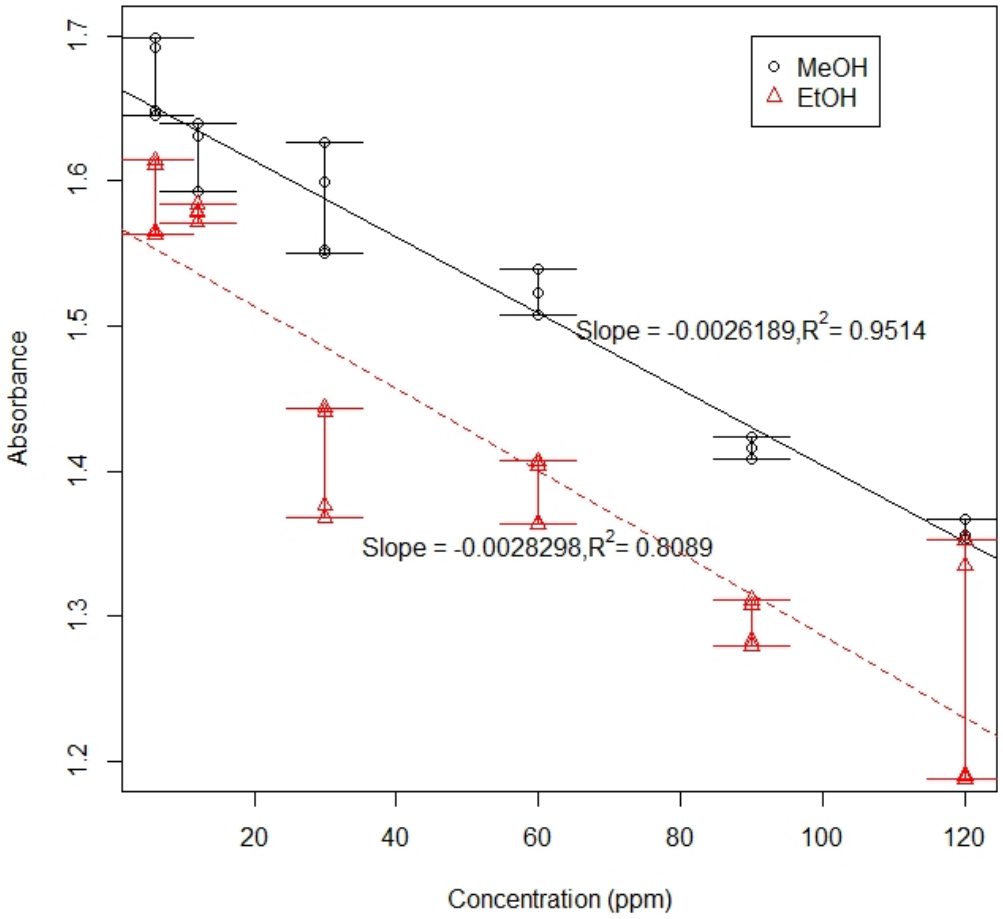

Figure 34: Comparison of absorbance and linearity of the sulfate assay with ethanol or methanol as the solvent.

	Methanol	Ethanol
Slope absolute value	0.0026	0.0028
Y-intercept	1.6662	1.5701
R2 value	0.9514	0.8089

Table 2: Parameters of the linear regression with methanol or ethanol as the solvent

The horizontal axis of Figure 34 is the concentration of sulfate standard solutions in ppm, and the vertical axis is the absorbance. According to Beer's Law, absorbance should be linearly related to analyte concentration, and the two linear regression fits of the six points with coefficient of determination values of 0.9514 and 0.8089 proved this linear relationship. To compare the performance of methanol and ethanol, the slope of methanol measurements is close to that of ethanol, which means methanol and ethanol do not make a difference in absorbance dependence on concentration. The fitness of the regression equation for methanol is acceptable with an R^2 value larger than 0.9. After repeated tests, methanol showed a slightly higher R^2 value and f value, which means the experimental data from methanol-based tests are more consistent with Beer's Law. The standard deviation of six measurements of the smallest concentration is 0.0061, corresponding to a limit of detection that equals to 7 ppm.

5.1.1.2 Nitrate

Potassium phosphate buffer was used to keep the pH of nitrate reduction reaction (mixture of nitrate, nitrate reductase and NADH) at ~7.5. Stock solutions of 100 ppm nitrogen (or 44 ppm nitrate) solution or 440 ppm nitrate solution where made by dissolving sodium nitrate powder into DI water. 0-44 ppm nitrate standards where made from the stock solution. First, nitrate, nitrate reductase (NaR) and dried NADH were added to the buffer and well mixed. For the enzyme to completely reduce all of the nitrate, the mixed solution was set aside for 20 minutes. Meanwhile the two color reagents – sulfanilamide and N-(1-Naphthyl)ethylenediamine dihydrochloride

solutions were made separately by dissolving these color reagents in powered form into DI water. 3M hydrochloride acid was added to the sulfanilamide solution. The final solution was made by adding the previous mixture with the two color reagents, which forms a pink color.

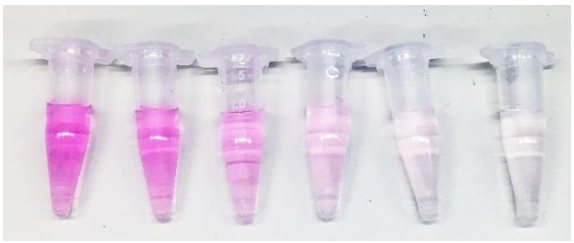

Figure 35: The colors of six different concentrations of nitrate are well developed

Six different concentrations of nitrate standard solutions were used for absorption measurements. The absorbance wavelength scan was performed with 5 nm step size, and the results shown in Figure 36 clearly show that the absorption peak wavelength was at 540 nm, which was the wavelength where the absorbance changed the most with the different concentrations. Each concentration was measured six times. The results in Figure 37 showed that using bench-top spectrometry, the absorbance measurements were in the range 0.04-0.18, and the R^2 value was 0.996, which indicates that the nitrate concentration has a significant linear relationship with absorbance. By analyzing six measurements of lowest concentration (2.2 ppm), the limit of detection based on the standard deviation was 0.1 ppm, which corresponds to 0.06 ppb in air.

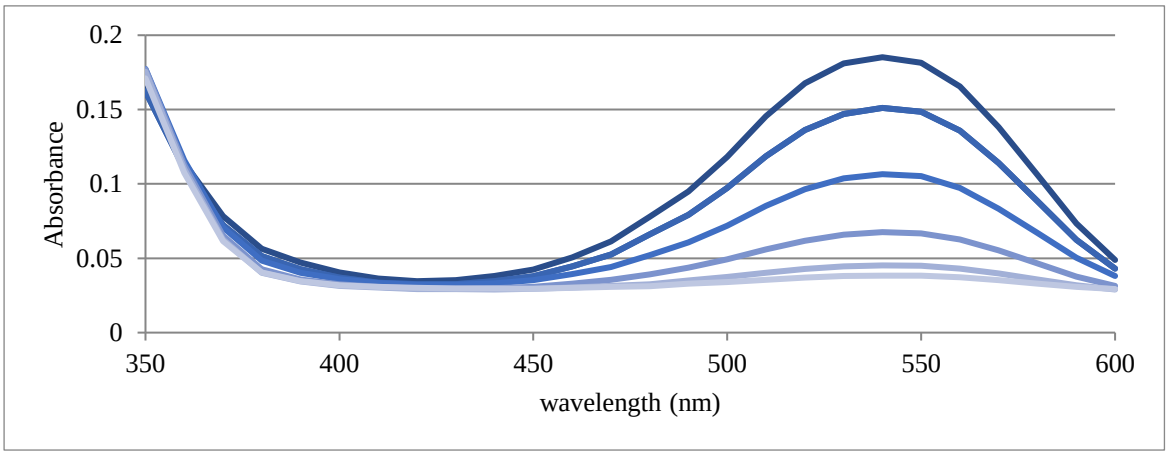

Figure 36: The absorption spectrum of the final product of the nitrate assay (6 concentrations)

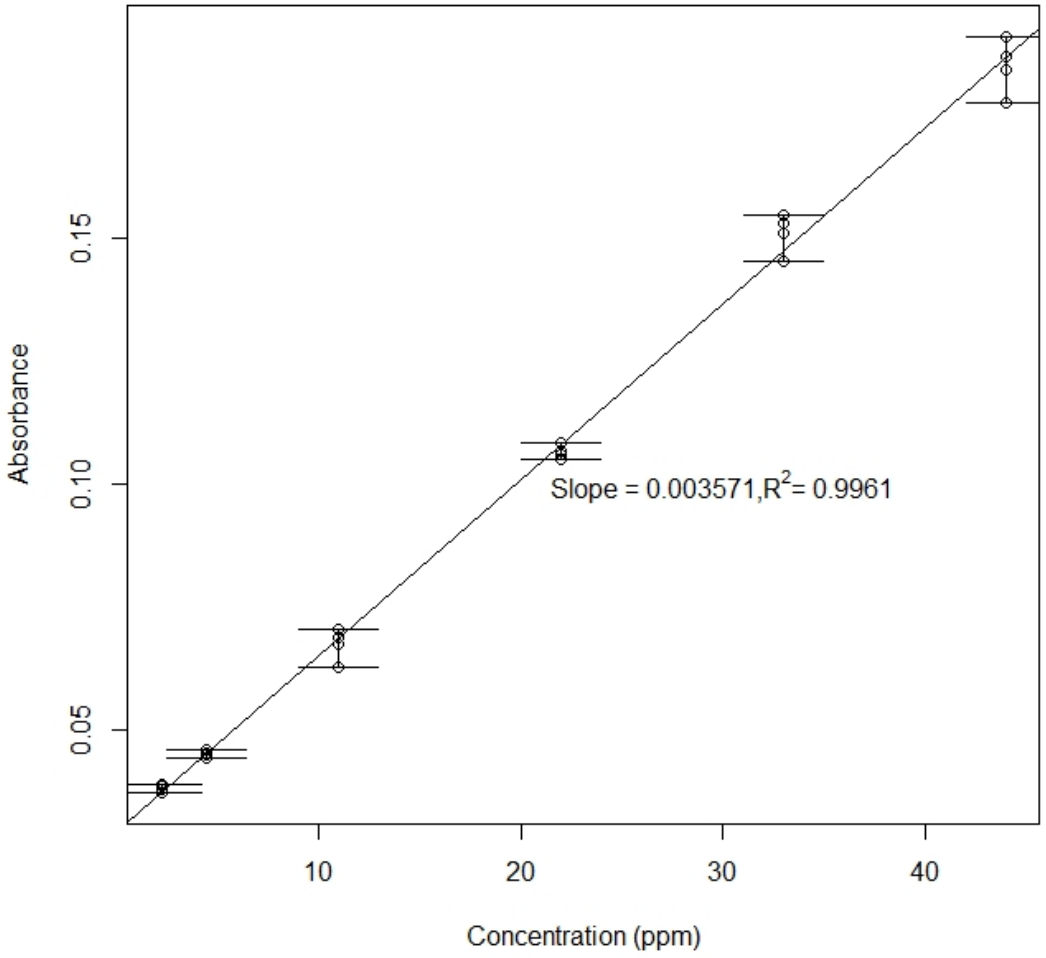

Figure 37: The linear regression of nitrate absorbance at 540 nm.

5.1.1.3 Ammonium

Stock solution of 1000 ppm ammonium chloride was made, and ammonium standards were made from it. Due to the toxicity of reactants in the other two methods (indophenol blue method and Nessler method, Chapter 2.3.3), only the OPA method was used.

The stock solution was prepared with sodium phosphate dibasic heptahydrate (0.1M), sodium hydroxide, and formaldehyde. Although in some studies the buffer solution (sodium phosphate dibasic heptahydrate) would reduce the useful life time of this stock solution, and was not recommended, the buffer stock solution was used in this study to keep the pH at 11 for better sensitivity, since NH_3-OPA-sulfite was found to be pH dependent [106]. The stock buffer solution can be kept in room temperature and lasts for months.

The color reagent solution was activated right before tests by adding sodium sulfite and would remain activated for a few hours in room temperature or longer at 4℃ in a refrigerator. OPA was first dissolved in 25% methanol and was well mixed. Meanwhile sodium sulfite was added to the buffer solution. The color reagent was made by combining the OPA solution with sodium sulfite buffer solution in 1:1 ratio. Finally, ammonium standards were added to the color reagent in 3:2 ratio, and the product solution was transferred to the Tecan plate reader for absorbance measurement. The results are shown in Figure 38. Each concentration was measured six times, and the limit of detection based on the standard deviation was 0.0565 ppm, as inferred from the data in Figure 39.

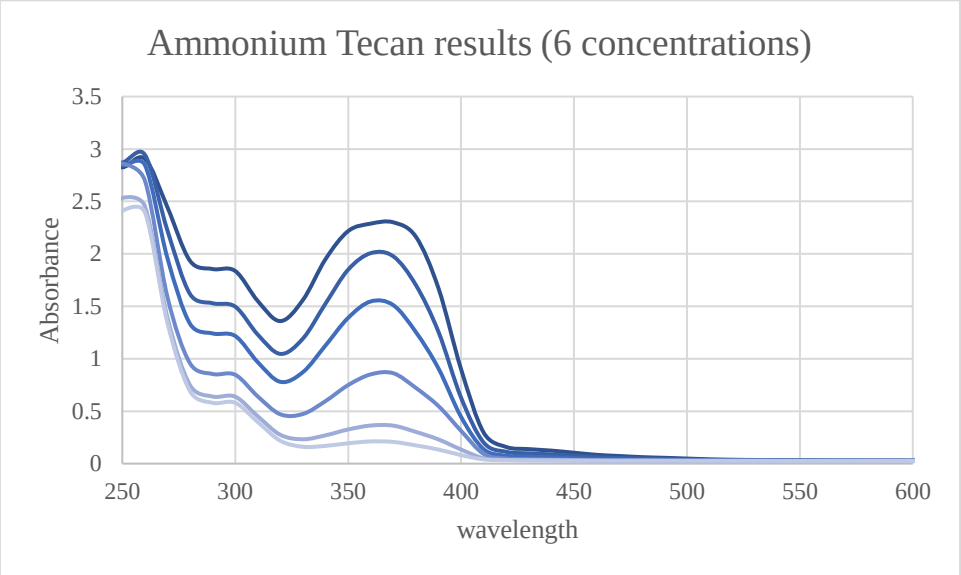

Figure 38: The absorption spectrum of the final product of ammonium assay (6 concentrations)

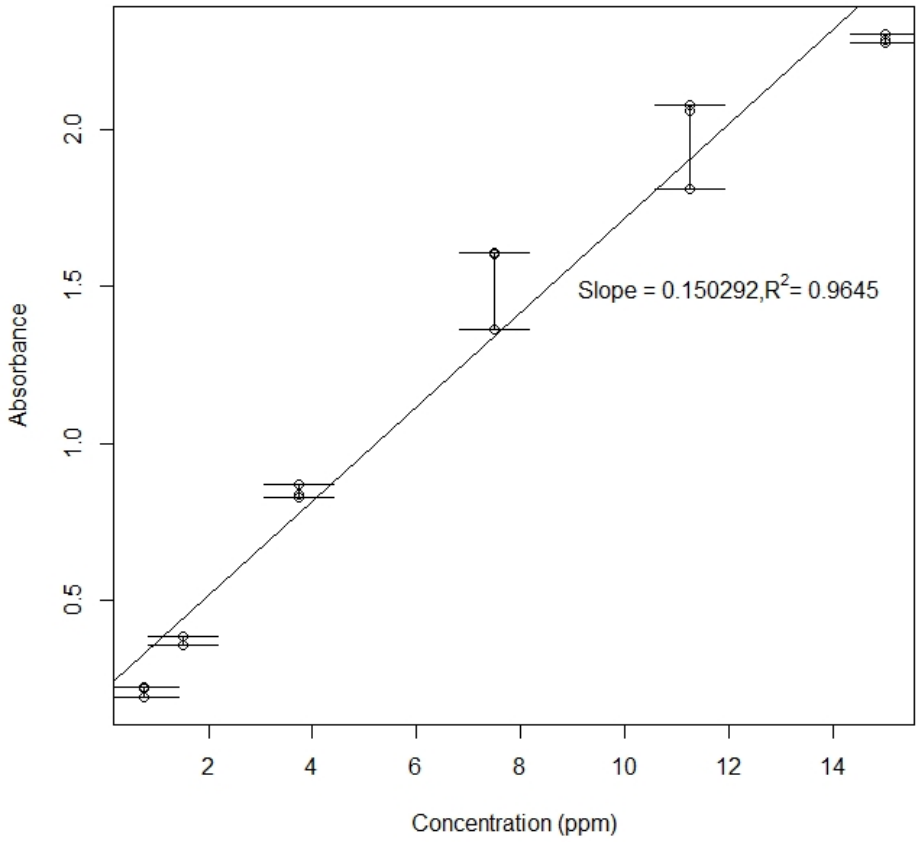

Figure 39: The linear regression of ammonium absorbance at 365 nm

5.1.2 Plate reader results over time

The absorbance stability of the resulting light absorbing sulfate solution was tested over time. By checking the absorbance after 12 hrs, 24 hrs and 48 hrs for all six solutions, it was found the MTB-Ba complex solution was stable and the absorbance barely changed. The sulfate-MTB final solution is dark grayish blue, the nitrate final solution is light pink, and the ammonium final solution is slightly yellow when it contains a higher concentration of ammonium. After a few days, the latter two solutions will have visible fading and a decrease in absorbance. As shown in Figure 40, within 48 hours, the

absorbance values of the three colorimetric tests decreased over time, and the maximum analyte concentration reduced the absorbance the most. The final solution obtained with 120 ppm sulfate reduced the absorbance by 5%, 44 ppm nitrate by 12%, and 15 ppm ammonium by 17.5%. However, in the first 12 hours, the change in absorbance was very small, less than the error of the measuring instrument, so it can be concluded that the absorbance of the final tested solutions of these three experiments are stable within 12 hours.

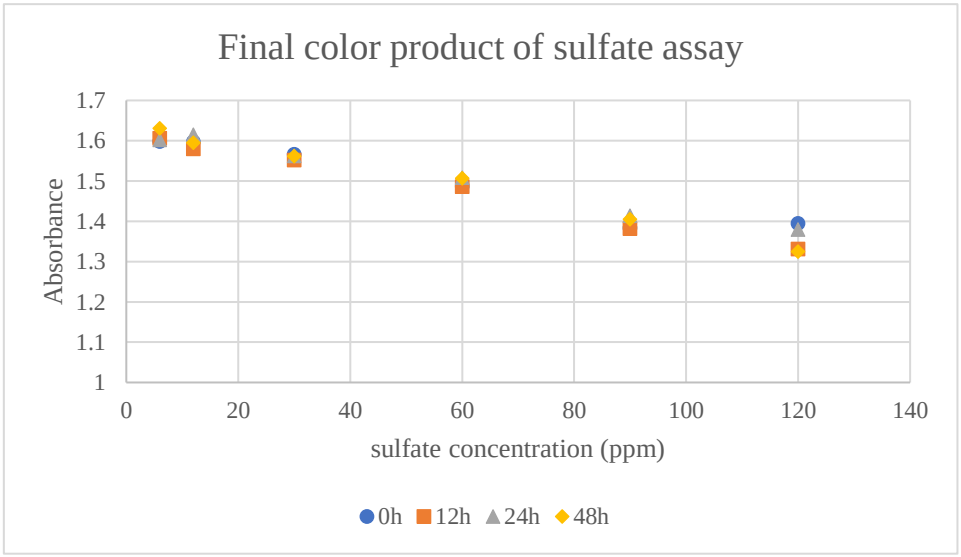

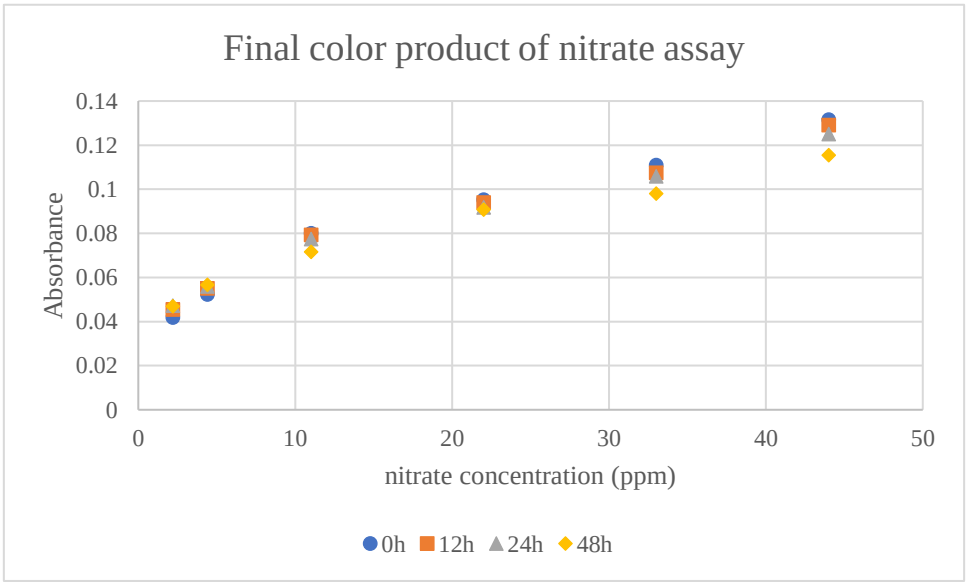

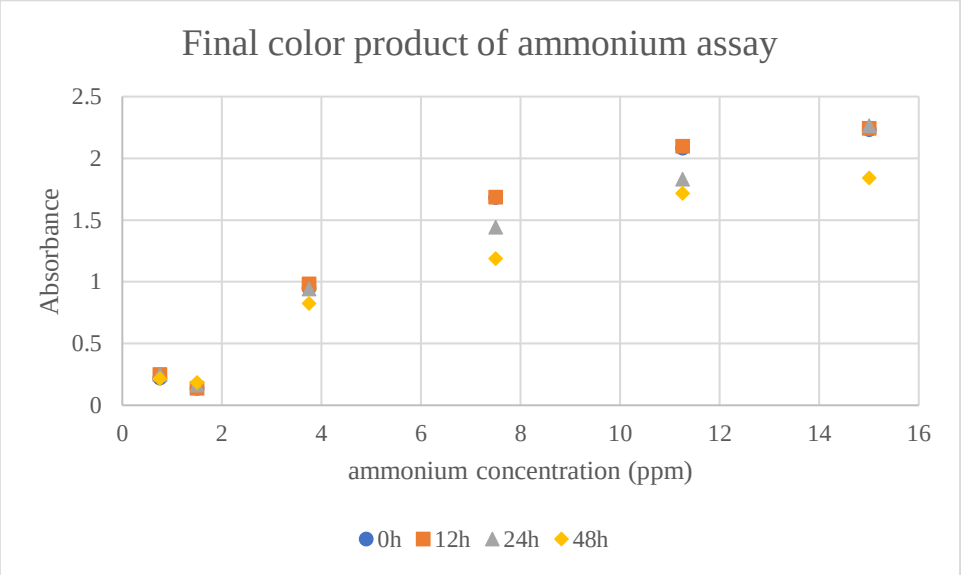

Figure 40: The change in absorbance of all three tests over time.

From the stability of the reagents, the acidic solution containing barium and MTB used in the sulfate experiment should be prepared daily. This mixed solution after one month exhibited a very clear precipitate. Using the supernatant would compromise the linearity and sensitivity in the sulfate assay.

5.1.3 Ion interferences

The conventional methods for preparing analyte standard solutions usually use a cation exchange column to remove interfering ions. Metallic cations are likely to complex with MTB in the same way as barium [107]. The sulfate MTB test is widely used for water quality monitoring, thus molybdenum, which is used for water treatment, shows a strong positive bias [108]. Sulfide and tannic acid must have a concentration three times that of sulfate to make a difference in absorbance. However, the same amount of sulfite will produce the same light absorption effect as sulfate, and these two ions seem to have the same extinction coefficient (molar absorptivity, Chapter 2.3). It was reported

that the concentration of sulfite complex with metal ions is 10 to 30% of sulfate concentration in primary aerosols close to industrial areas [109]. Nitrogen oxides promote the conversion of sulfur dioxide and sulfite to sulfate in air, and in PM2.5, the total amount of sulfur in non-sulfate form varies, and can be up to about 2% [110]. Depending on the location of measurements and the composition of particulate matter, the impact of sulfite needs to be estimated.

For the OPA-sulfite-ammonium assay, sulfite is used as the reducer (instead of using mercaptoethanol or N-acetyl-cysteine), which helps reduce the primary interference amine to <0.5% [111]. There are no other reported interference ions. For the nitrate test, because the reaction of nitrate reductase and nitrate is specific, the interference ions may come from the Griess test. EDTA in the buffer is effective in reducing the impact of other ions. The most common interference, chloride and sulfate, have negligible effect even when the concentration is 600 times higher than nitrate. Among metal ions, if the concentration is less than 10 times the national water-quality-laboratory median value, then the effect is kept within $\pm$2%. Calcium with 100 times the national water-quality-laboratory median value of calcium concentration (~3600 ppm) makes 15% difference, but this level of calcium is very unlikely to be found [112].

When three ions coexist, the effects of each of these three ions on absorbance are listed in Table 3 based on reported results [107, 112] and lab results. The marked results were from previous studies which used the same chemical methods, the unmarked results are derived from the new experimental results generated using the Tecan plate reader and is represented by the average of five repeated measurements. The table lists the effects

of the two other coexisting ions on the measured analyte ion concentration. The interference ion concentrations, the actual concentrations of the analyte ion, and the measured values are listed horizontally in the table. The table shows that the excess interfering ions do not make a difference between the measured concentration and the actual concentration.

		sulfate		
		interference concentration	analyte concentration	measured value
interference	sulfate			
	nitrate	48mg/l *	30mg/l *	30mg/l *
	ammonium	75mg/l	30mg/l	30.2mg/l

		nitrate		
		interference concentration	analyte concentration	measured value
interference	sulfate	2287mg/l **	2.5mg/l **	2.51mg /l **
	nitrate			
	ammonium	75mg/l	25mg/l	25.2mg/l

		ammonium		
		interference concentration	analyte concentration	measured value
interference	sulfate	90mg/l	25mg/l	25.1mg/l
	nitrate	75mg/l	25mg/l	25mg/l
	ammonium			

Table 3: The effects of sulfate, nitrate, and ammonium on three colorimetric methods when they interfere with each other. * is from Adamski [107], ** is from Patton

[112]. Since these references used higher concentrations, it would be helpful to show their results here. Less concentrations of interference ions have been used in my study and showed similar results (not shown).

5.2 Validation of Detection Chemistries with On-chip Methods

To measure absorbance on chip, a light path must be developed that directs light through the droplet containing the analyte to be measured. Both a vertical light path (perpendicular to the chip surface) (see Figure 41) and a horizontal light path (parallel to the chip surface) (see Figure 42) were made by aligning two optical fibers in different directions. One optical fiber is connected to the light source, the other to a spectrometer (Ocean USB2000). The details of both setups are presented in Sections 5.2.1 and 5.2.2.

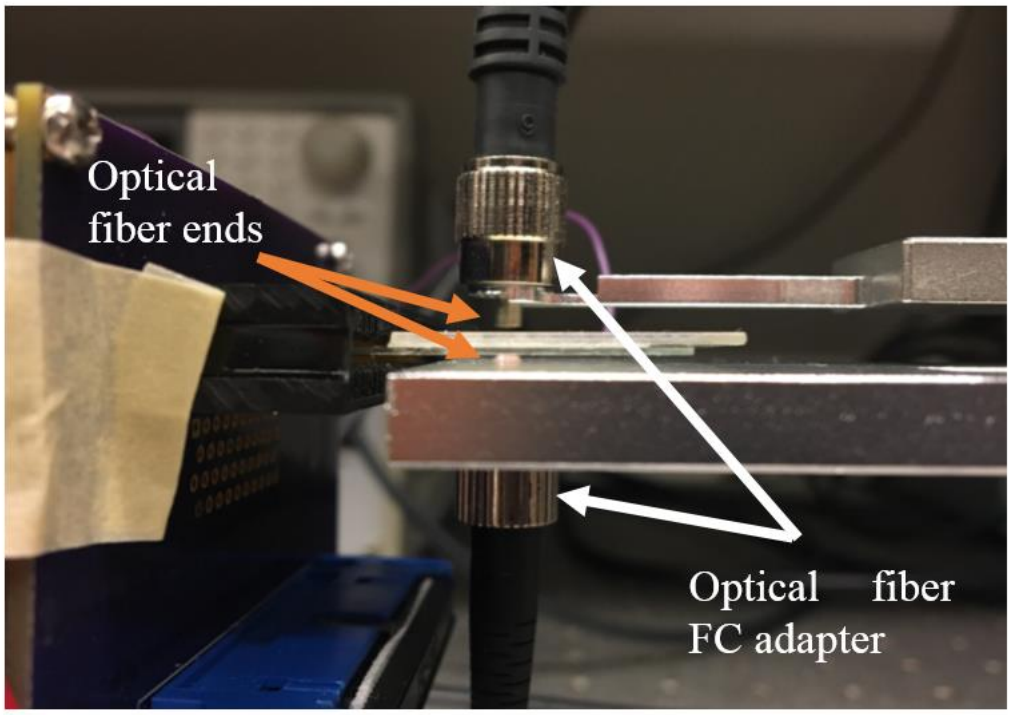

Figure 41: A side view of the relative position of the vertical optical fibers and the chip

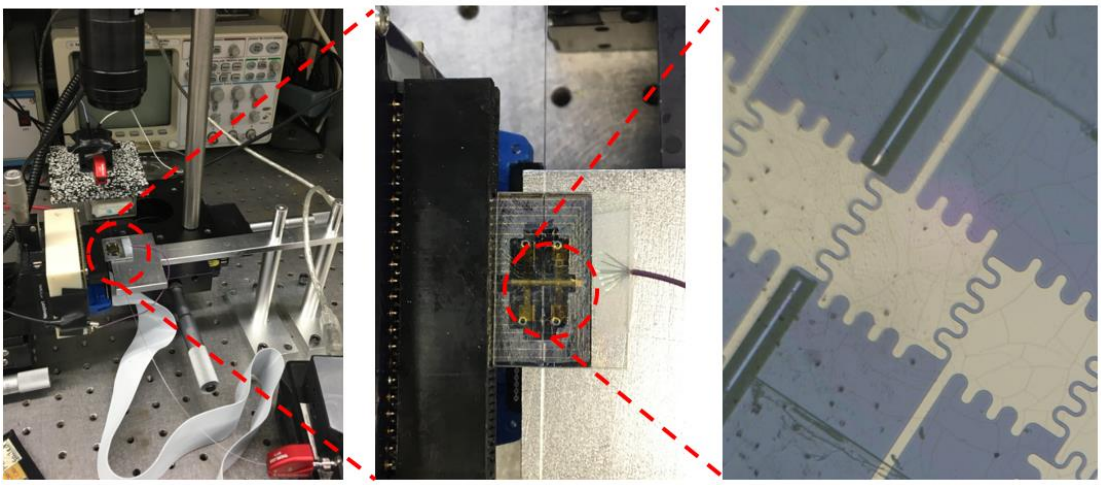

Figure 42: Top view of the horizontal optical fibers

5.2.1 Vertical light path

In this experiment, the bottom plate of the chip used glass and indium tin oxide electrodes, so light could pass through the chip from source to detector. Light was provided by an LED, and was directed by an optical fiber (bottom optical fiber in Figures 41 and 43, Thorlabs FG200UEA, 200 μm core diameter) to the bottom plate. The transmitted light was captured by another optical fiber (top optical fiber in Figures 41 and 43, Thorlabs M35L01, 1000 μm core diameter) from the top of the chip, and was measured by a spectrometer.

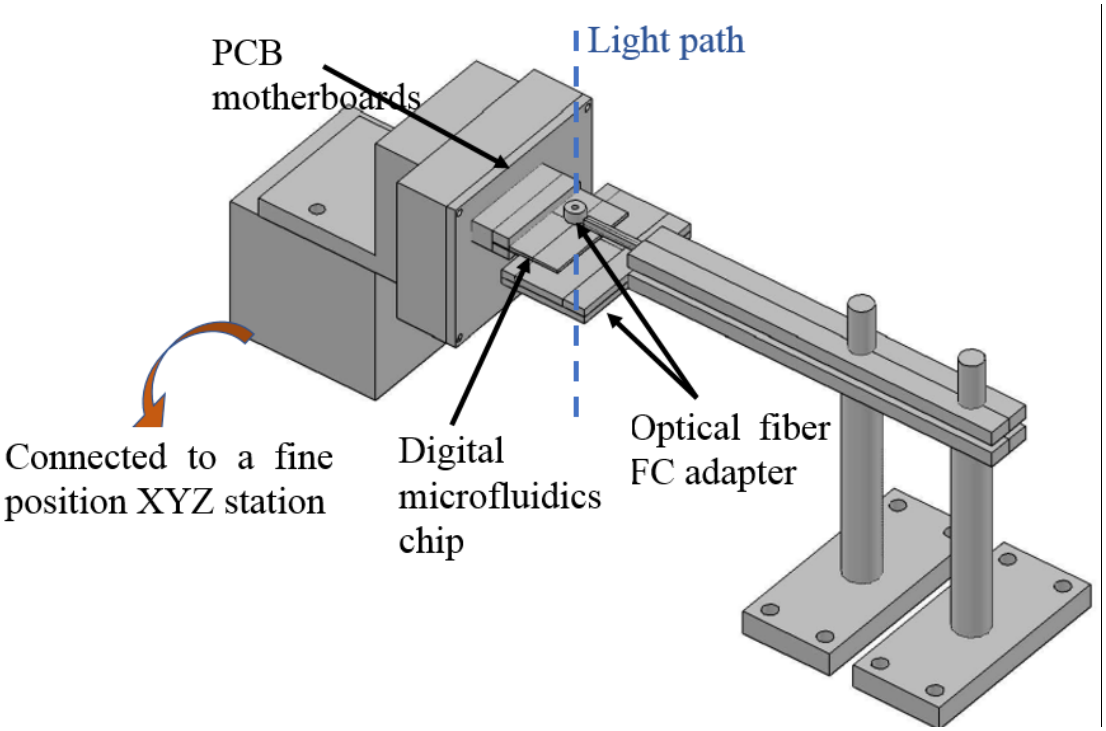

Figure 43: The system setup of the vertical measurement experiment.The box on the left is connected to an XYZ axis station, and the droplet is placed in the middle of the light path by fine-tuning the chip position. A PCB card edge slot connector is mounted on the motherboard in the vertical direction, and the connector pads of the chip are correspondingly inserted into the card slot, and through the motherboard and a connected ribbon cable (not shown). They are connected to the controller PCB. The two arms on the right side fix the optical fibers, and the two vertical rods ensure that the two optical fibers are vertically aligned.

The alignment of the two fibers was guaranteed by fixing the two fiber ends onto two machine-shopped aluminum arms. Both fibers had FC connectors which screwed onto the two FC adaptors at the end of the aluminum arms. The aluminum arms were aligned by two punched holes that tightly fit into two fixed vertical rods. The error from the

CNC drilling and milling machine was less than 20 μm. It was very important to align the two optical fibers, and the alignment would be better if the fixture was made from a single optical fiber. However, the top optical fiber needed to be removed sometimes so that the microscope camera could take photos from the top for observational purposes.

The diameter of the optical fiber (0.2 mm) for the incoming light was chosen to be much smaller than the droplet diameter (1 mm) and the fiber head positioned at the center of the droplet, as shown in Figure 44. This was to avoid any lens effects caused by non-uniform solutions over the diameter of the droplet. In this case, most of the light that came out of the optical fiber head passed through the droplet, even though it was not collimated. However, the smaller the optical fiber diameter, the harder it was to align the input and collection fibers. Thus, based on experimentation a 0.22 mm cladding diameter was selected. The digital microfluidics chip was held by a card edge connector and was mounted on a precision positioning stage. Figure 44 shows the relative sizes of the input fiber and the droplet.

The electrowetting control parts, shown in Figure 45, were the same for all experiments. An Arduino processor was programmed to output serial signals for 32 electrodes for the smaller testing chip or 57 electrodes for the complete chip. A 74HC595 shift register was used to change the serial signals to parallel signals, and each signal controlled a MOSFET relay (LCC110 OptoMOS®). Each relay output a voltage signal which was either ground (0V) or high (0V $-$ 350V_{rms}). These outputs were connected to the legs of the card holder correspondingly, and the spring pins inside the card holder pressed

firmly onto the gold or indium tin oxide connection pads on the chip. Every voltage path could be individually controlled, and an Arduino graphic user interface was created by MegunoLink with clickable buttons to turn any individual electrode on and off.

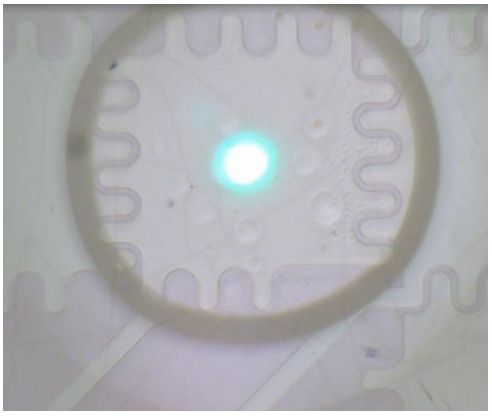

Figure 44: The relative size and position of the optical fiber and the droplet

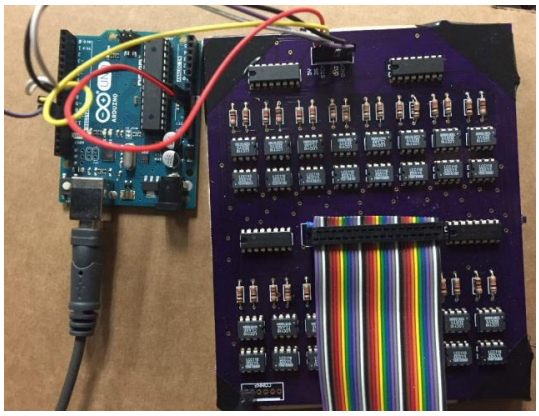

Figure 45: The Arduino controller outputs a serial signal to a PCB board that converts to parallel high output voltages

5.2.2 Horizontal light path

Chips utilizing a horizontal light path were fabricated by fixing two bare optical fibers inside the chip between the top and bottom plates. To keep the optical fibers in place, a step was added before parylene deposition to build an SU-8 channel of ~150 μm, as

shown in Figure 46. Both optical fibers used had 220 μm cladding diameters, which was lightly less than the channel height. The optical fibers were carefully cleaved to create a flat end surface and were coated with CYTOP, so that droplets could easily pass between the fibers without being pinned. During chip assembly, the optical fibers were placed in these pre-made channels, as shown in Figure 47. The 0.24 mm gasket shape was redesigned to have the SU-8 area and the optical fiber area cut out and was used to connect the upper and lower plates as well as keeping the optical fibers in place. The fibers were coupled with the LED holder and the spectrometer using a Thorlab BTF1 bare fiber terminator with 230 μm SMA905 ferrule, as shown in Figure 48.

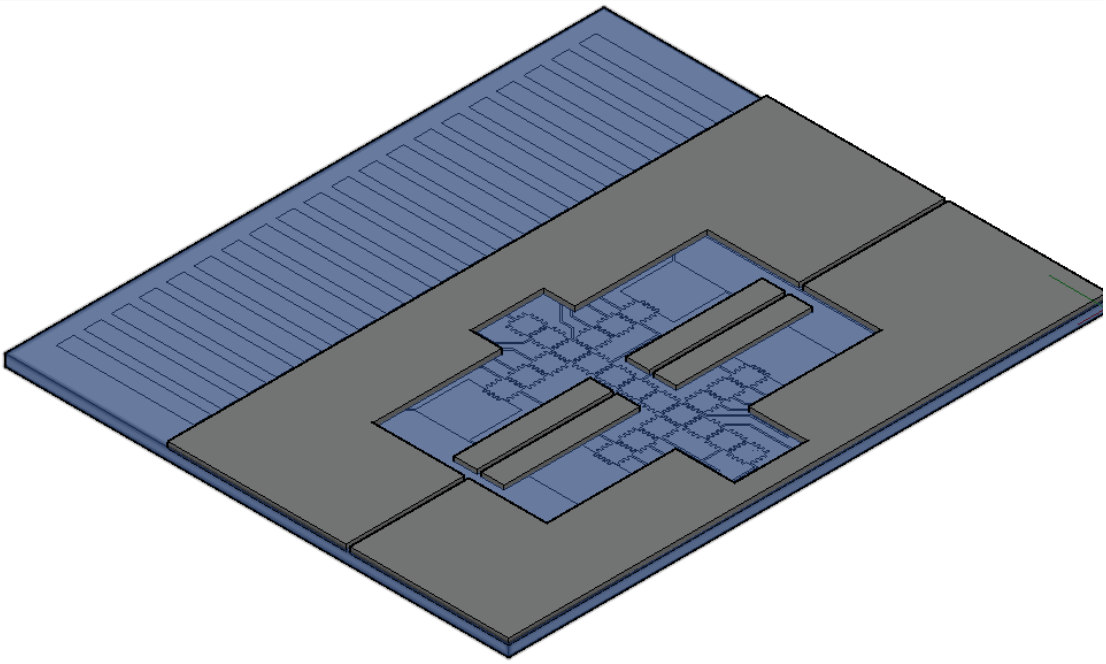

Figure 46: A channel from SU8 to fix the optical fibers in place

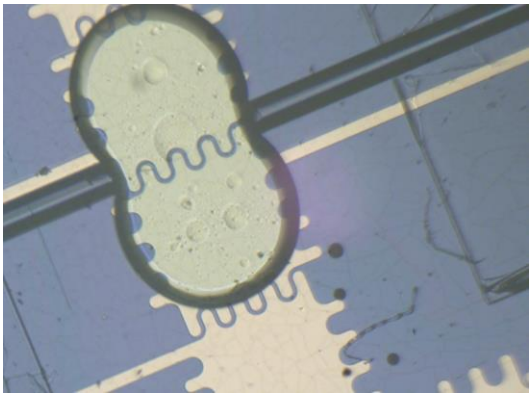

Figure 47: A droplet held by two activated electrodes between horizontal optical fibers.

Figure 48: Bare fiber terminator used to fix the optical fiber and the spectrometer

Because the channel for holding the optical fiber was patterned by photolithography and the channel was a tight fit for the fiber, the fiber alignment was good, and the incoming and outgoing light paths were aligned. A second advantage of the horizontal light path was that the light path length was as long as the electrode pitch (0.7 mm) instead of being limited by the vertical channel height (0.24 mm). Beer's Law applies to low concentration analytes in solution, and the horizontal light path resulted in a longer light absorption path, which means Beer's Law is more likely to be valid, and the signal to noise ratio of the absorption measurement should be increased too.

5.3 On-chip Absorbance Test

The results from vertical and horizontal measurements were compared in terms of linearity based on R^2 values, reproducibility based on standard deviations of different droplets and different measurements with the same droplet, and limit of detection based on standard deviations and slopes: 3x standard deviation of the lowest concentration / slope of the linear fit.

5.3.1 Vertical light path measurements

Several tests were designed to evaluate the performance of the vertical light path of absorbance measurements. Initially, pre-mixed solutions of MTB-Ba sulfate were introduced onto the chip. The absorbance of these pre-mixed solutions had already been tested with the plate reader, and the linear relationship between the absorbance and sulfate concentration had been verified. To reproduce this linear relationship on chip, it must be verified that the shortened light path length (from 4 mm (plate reader) to 0.24 mm (on chip)) would not appreciably change the signal-to-noise ratio.

The first test was to introduce each MTB-Ba sulfate pre-mixed solution on chip and measure the absorbance. The solution was filled with a pipet into a reservoir of the chip. A droplet was dispensed and moved to the detection electrode. It stayed on the detection electrode for 20 seconds, moved away for 20 seconds, and moved back to the detection electrode for another 20 seconds, and this process was repeated several times. During the entire experiment, absorbance measurements were taken every 100ms and plotted. This process was repeated for all six MTB-Ba sulfate final solutions. Figure 49 shows

an example of test droplet dispensing and transporting to the detection electrode. The camera was located at the top right of the chip to stagger the position of the optical fiber. This angle causes the light transmission point of the LED to look very small, which is a yellow dot in Figure 49f. Figure 50 shows the absorbance measurements for six sulfate concentrations. Each sulfate concentration corresponds to a time-absorbance plot. These figures can be used to compare the measured absorbances of the same droplet, or to compare the absorbance between different droplets to obtain the relationship between absorbance and sulfate concentration.

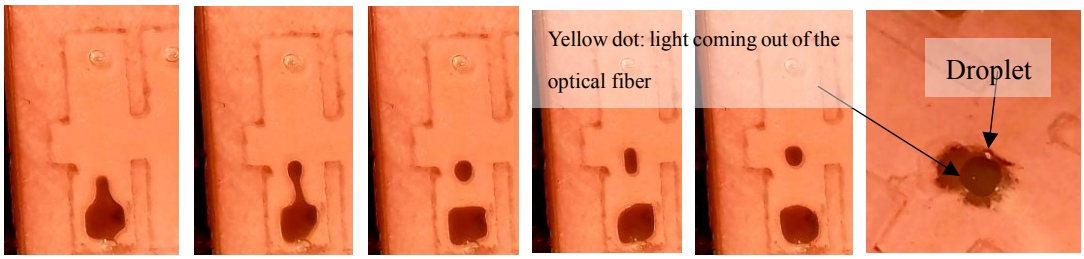

(a) (b) (c) (d) (e) (f)

Figure 49: (a)-(e) Droplet dispensing. (f) Droplet transported to detection electrode. The small orange dot shows the light coming out of the optical fiber. The area of light is completely covered by the electrode.

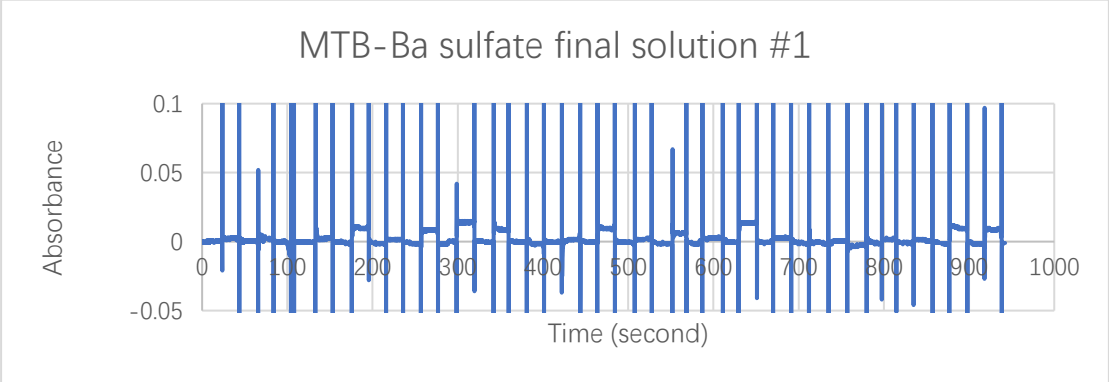

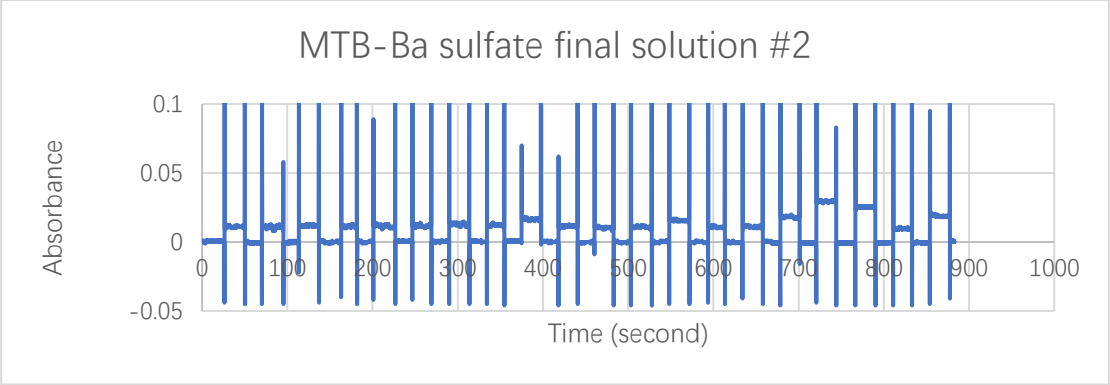
MTB-Ba sulfate final solution #2
Absorbance
0.1
0.05
0
-0.05
0
100
200
300
400
500
600
700
800
900
1000
Time (second)

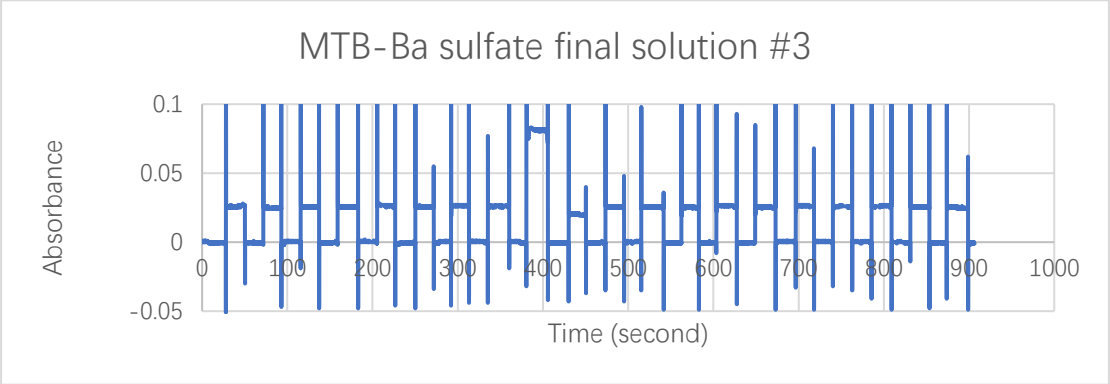
MTB-Ba sulfate final solution #3
Absorbance
0.1
0.05
0
-0.05
0
100
200
300
400
500
600
700
800
900
1000
Time (second)

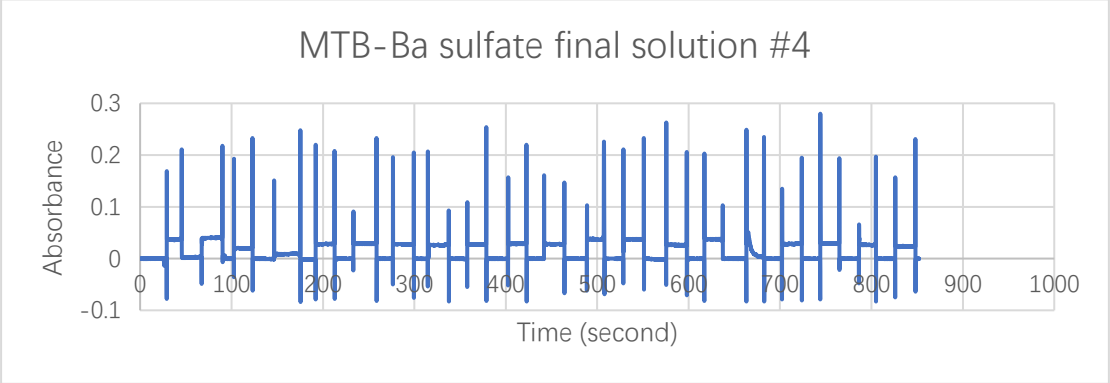
MTB-Ba sulfate final solution #4
Absorbance
0.3
0.2
0.1
0
-0.1
0
100
200
300
400
500
600
700
800
900
1000
Time (second)

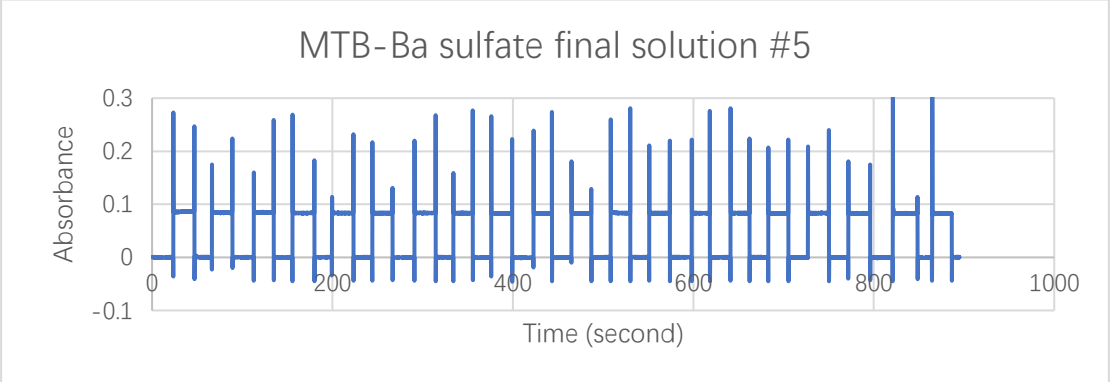
MTB-Ba sulfate final solution #5
Absorbance
0.3
0.2
0.1
0
-0.1
0
200
400
600
800
1000
Time (second)

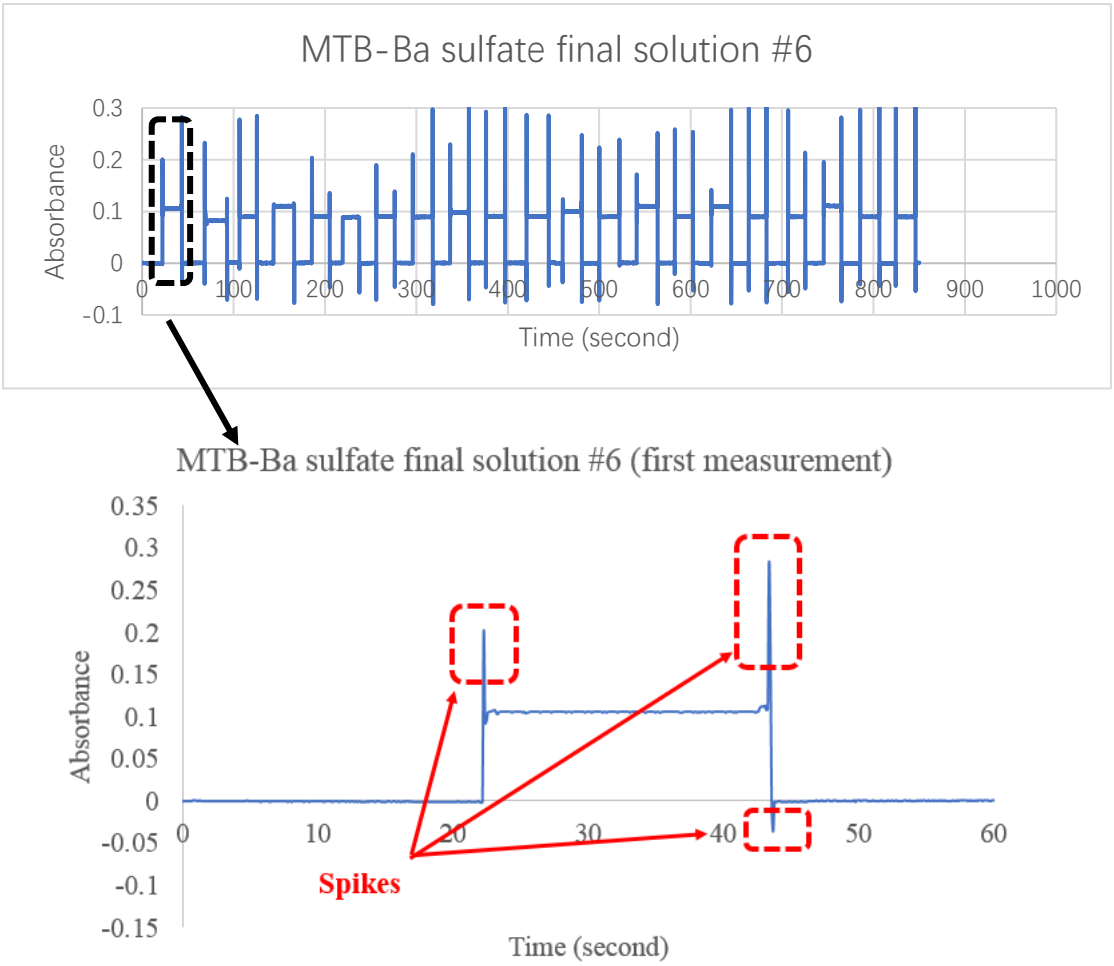

Figure 50: The absorbance measurements of six concentrations of sulfate overtime with a vertical optical detection path on chip. The last picture magnifies the first measurement of solution 6, and it is clear that the edge of the droplet caused the absorbance to suddenly rise as the droplet entered and left the range of the light path. Spikes of different heights appear in the figure (the value may be negative)

Some spikes can be clearly seen on these absorbance-time plots, and these spikes indicate the moment when the droplet was moving onto or out of the measurement electrode, and the edge catches the light. These spikes are very helpful to distinguish if the droplet is in position or not, especially for lower concentration solutions, when the

absorbance was very close to zero.

The spectrometer parameters were set as follows: integration time: 3 milliseconds, scans to average: 5, moving average: 5 nm. The dark noise correction was on, and the dark spectrum was taken before turning on the LED and was automatically subtracted from later measurements. The reference bright spectrum was taken each time before introducing the MTB-Ba sulfate solution, or in other words, it was the light intensity received by the spectrometer with only silicone oil inside the channel. This reference spectrum was kept the same during the droplet movements and was used to calculate the absorbance every time a droplet moved to the detection position. When a droplet moves away, the absorbance should return to zero. The results show that when the droplet was moved away from the detection electrode, the absorbance always read in the range 0 ± 0.003, and this zero reading did not increase over time. This means the LED brightness was stable, the setup was stable, and the droplet did not leave any residue while moving away. However, if the testing chip was touched and maybe slightly moved each time when the solution in the reservoir was changed, the reference light spectrum had to be taken again for calibration.

For each concentration, 20 measurements of droplet absorbance were taken, each for 20 seconds. The absorbance spectrum was taken every 100 milliseconds, and the absorbance at 608 nm was extracted and plotted (Figure 50). The results show several interesting things:

1, The absorbance is much smaller than the absorbance measured with the plate reader, even without diluting the final solutions. This was expected since the light path was

reduced on chip.

2, During each of the 20-second periods, the absorbance was stable, except for one measurement with solution #4.

3, The absorbance measured in different periods can be very different. For example, the absorbance measured with solution #3 shown in Figure 50 in the period around 400 seconds was more than 100% larger than the absorbance measured in other periods.

To evaluate the absorbance changes from different periods, the average of 200 data points in each period was taken, representing the absorbance level in that specific period. Thus, each solution had 20 averaged data points of this averaged absorbance. These points are plotted in Figure 51. The solutions with higher sulfate concentration (lower absorbance) were more affected by the variance between measurements. Solution 1 in Figure 50 had the lowest average absorbance, and its standard deviation was 95% of the average value.

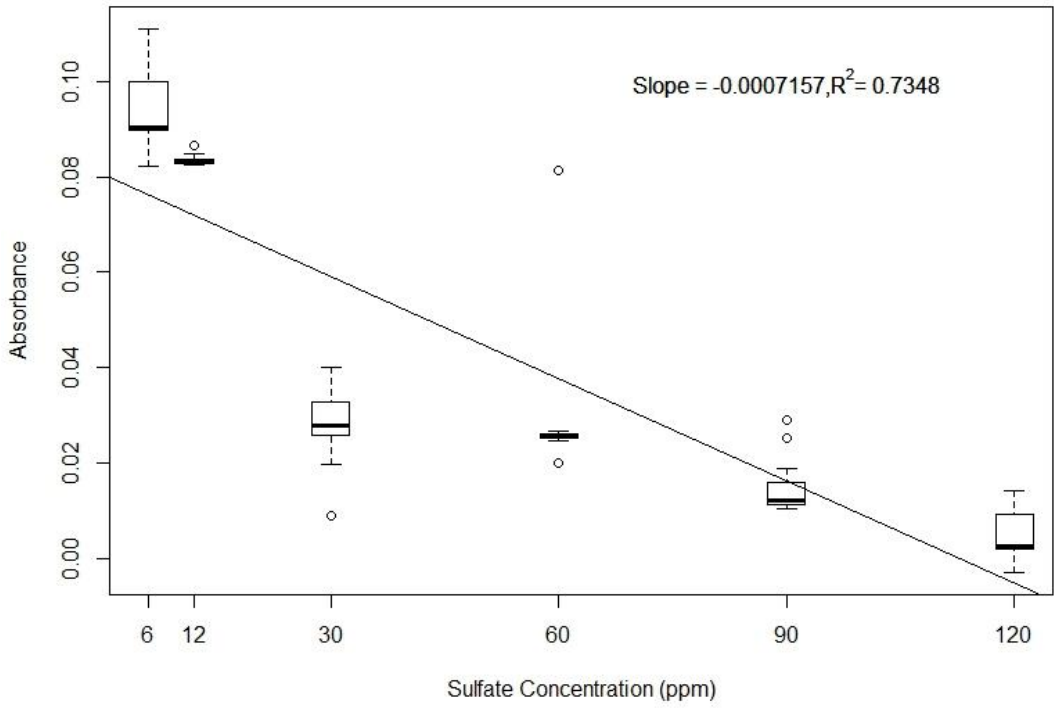

Figure 51: The 20 absorbance measurements (averaged over the measuring period) for each of the six sulfate concentrations. The solution number starts from the highest sulfate concentration, so in the figure from the right to the left is solution 1-6, corresponding to Table 4

solution #	1(120ppm)	2(90ppm)	3(60ppm)	4(30ppm)	5(12ppm)	6(6ppm)
Average of 20 measurements	0.0052	0.0143	0.0282	0.0276	0.0835	0.0950
Std of 20 measurements	0.0049	0.0051	0.0126	0.0083	0.0009	0.0088
std/average (%)	95.4	35.5	44.5	29.9	1.1	9.2

Table 4: Statistics of the absorbance measurements from Figure 51.

In Figure 51, linear regression was done with all 120 data points, and the R^2 value was

0.7348, indicating that the absorbance obtained from on-chip measurements and the sulfate concentration were somewhat linearly related, but the error could be large when measuring sulfate solutions with unknown concentrations. From the graph, 12 ppm and 60 ppm had more consistent absorbance measurements, but 6 ppm also had outlier points. Outlier points were a common situation during several repeated tests.

It was suspected that the cause for the poor linear relationship came when the loading pipette touched the chip during solution changing and the incident light intensity was updated and recorded. A test was designed with three different concentrations of droplets introduced all at the same time, and the chip was never touched or moved during the measuring period. Three droplets of different concentrations were measured in turn. Still, the result clearly showed that each measurement could be quite different.

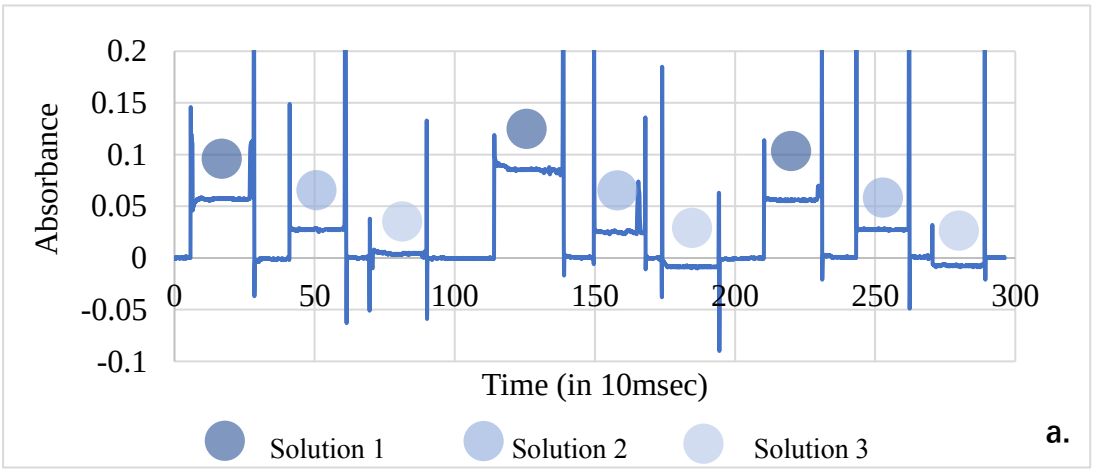

a.

b.

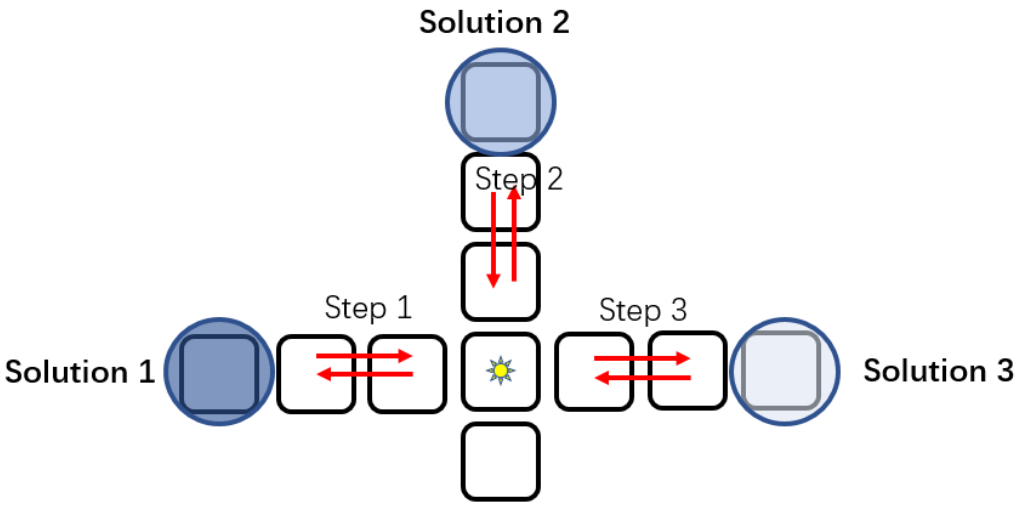

Figure 52: Measurements of droplets with different concentrations on the same chip. Figure a (upper): three different concentrations of sulfate droplet were measured in turn. The three measurements of absorbance with the highest concentration droplet (solution 1) are quite different (0-30s, 110-140s, 210-240s). Figure b (lower): the position and route of the droplets on the chip

The purpose of this experiment was to test whether it was possible to measure the linear relationship between droplet concentration and absorbance according to Beer's law, when systematic errors caused by the change in the relative position of parts were removed. Such changes were due to the pipette tip touching the top plate and the subsequent compression of the gasket (the gasket is a resilient material) during reservoir loading. The test chip was designed with four reservoirs that could simultaneously measure up to four different concentrations of analyte. Before the absorbance was measured, the four solutions were injected into the chip separately, avoiding any

displacement or tremor of the chip during the test. However, since the difference between the multiple measurements was too large, and the measurement of the absorbance of the low concentration solution was often negative (which indicates that the shape of the droplet had a light converging effect), the results obtained were not reliable.

To find the cause of these variations in measurements, two tests were designed and explained in detail in the following sections.

5.3.1.1 droplet moving from different directions

Since the whole experimental setup including the chip was not the cause for the variation in readings and the variation seemed to occur randomly with the movements of the droplet, it would be interesting to try moving the droplet in different directions and find out if this would cause the readings to be different. A DI water droplet with red food dye was used. Figure 52 shows one droplet being moved to the detection electrode and away for three times from different directions.

Thin films of oil have been observed between the droplets and the upper and lower plates in an electrowetting device [113-115]. In these oil layers, oil lenses can form due to the presence of capillary waves in the oil film during the movement of the droplet. When the droplet stops moving, the local oil film thickness is uneven. This happens near both the upper and lower plates. A recent study showed that the morphology and duration of the oil lenses are related to the activation voltage, actuation frequency and the use of a surfactant, and at some critical conditions the oil film is broken [114]. In

this work, the oil lens appeared frequently and did not disappear with time.

The present work experimentally found that when a droplet stopped moving and stayed on an electrode, the position and size of the oil lenses were also fixed. However, the size and position of the oil lenses changed after the drop moved away from and back to its original position (Figure 53). Arrows point to some of the larger oil lenses. It is not clear if these lenses occurred on the bottom plate or the top plate, because the depth of field of the optical microscope was larger than the thickness of the channel, and interference microscopy should be used to determine the accurate height of these lenses. Figure 54 [114] shows the formation of oil lenses at the oil film under the top plate. The oil lenses of the upper and lower plates are basically indistinguishable. In both positions, large diameter lenses and small and dense lenses can be formed. Figure 55 [114] from the previously mentioned study shows the interference patterns of upper and lower oil lenses. Unlike this study, the oil lenses did not change over time in 0 to tens of seconds time range.

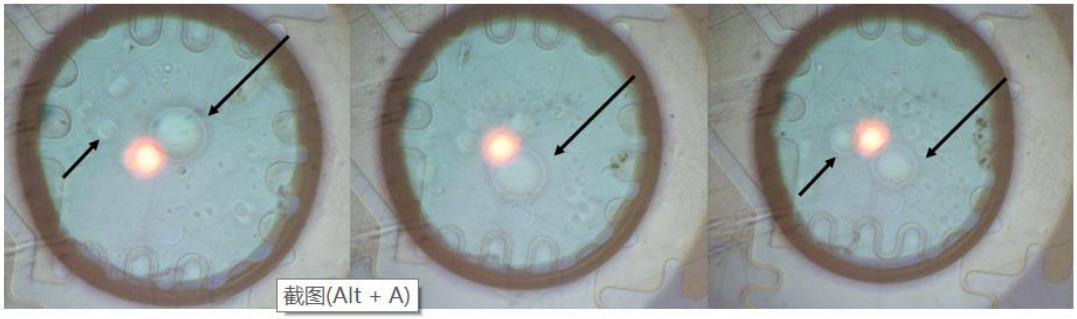

Figure 53: The oil lens position and size changes with every movement.

Figure 54: Side-view photos showing the formation of oil lenses [114]

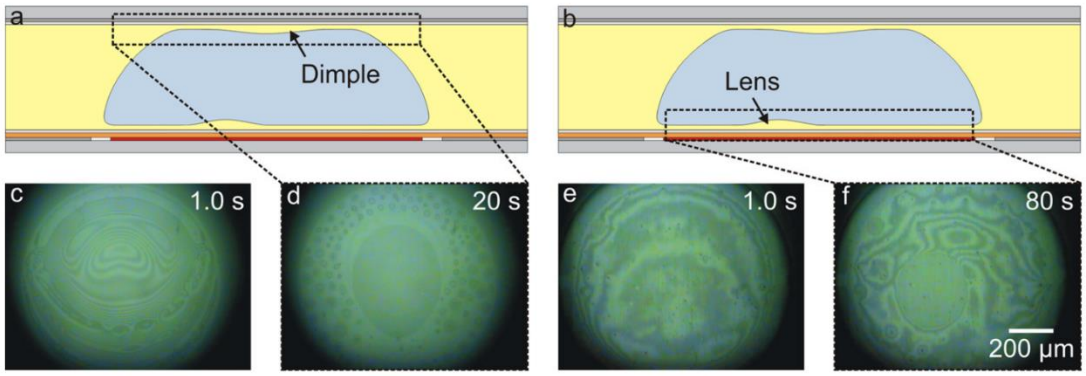

Figure 55: The oil lenses on both surfaces. Electrowetting condition: 100V 100Hz AC, translational droplet speed 1.5mm/s [114].

5.3.1.2 Voltage polarity switch

From the previous experiment, oil lenses were observed in the experimental setup used to measure analyte absorption. These lenses could be a local area where the oil films above or under the droplet were thicker, or even the oil film could be ruptured at that point. Earlier studies showed that turning on/off the electrode or changing voltage polarity can change the capacitance between the electrodes with a droplet between them. [116] The change was sometimes repeatable but sometimes semi-random, and it was suspected that the only possible explanation was the thin oil layers [116]. More viscous silicone oil makes the rise in capacitance of the droplet slower and changing voltage may cause the droplet to displace oil around it differently. This suggests that changing voltage may also cause a different absorbance measurement.

The polarity switching experiment was designed as follows:

1. The power supply to the actuation electrodes outputs 50V and the chip starts with the top plate connected to ground. By turning on electrodes sequentially, a

droplet was moved to the detection electrode;

2. A droplet of 6 ppm sulfate was dispensed. The droplet stayed on the detection electrode for 30 seconds, then the voltage polarity was switched, with the bottom plate detection electrode grounded and the top plate connected to 50V.
3. After 30 seconds the voltage was switched back and the absorbance was measure for another 30 seconds before the droplet was moved away. This was repeated for several times. The absorbance over time was plotted. In the first five tests, the conversion of voltage polarity did not result in a change in absorbance. In the sixth and seventh test groups, the change in voltage polarity caused a significant change in absorbance. In the last three test groups, at the moment the polarity changed, the absorbance increased briefly, probably because the voltage was briefly zero during the voltage conversion, and the shape of the oil film changed briefly. When the reverse voltage was added, the oil film shape resumed.

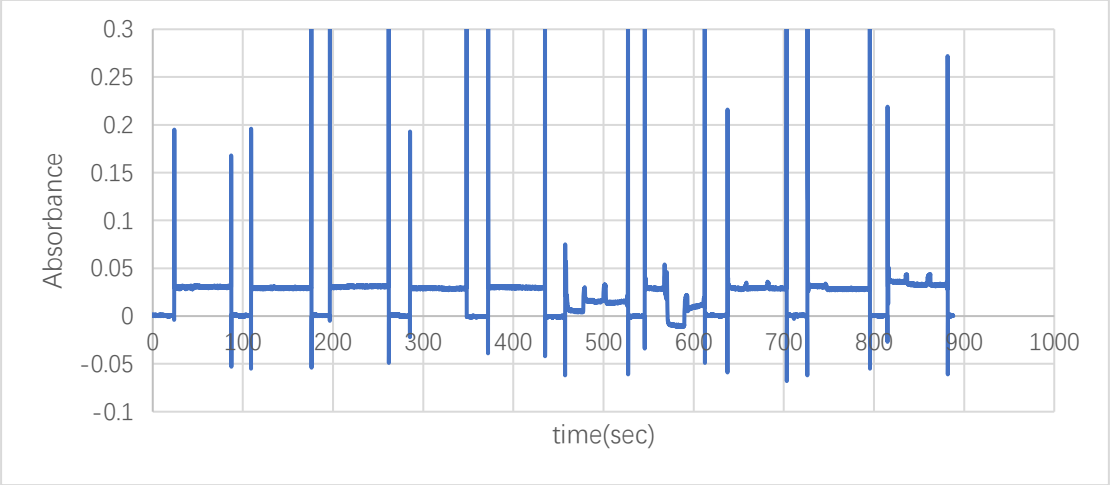

Figure 56: The absorbance changes with voltage polarity switches. The spikes indicate the droplet moving in and out. Between two spikes (90s), the polarity switching happens

at 30s and 60s, while the droplet did not move. In the first five tests, the voltage polarity switch points were not obvious. In the latter groups of tests, the point of the polarity switch was shown by a significant change in absorbance, which is easy to see in the figure.

Figure 56 shows the first experiment run with 10 measurement groups. It shows that voltage polarity switching does not always affect absorbance, but there is a 25% chance that it does. This experiment was repeated two more times. In a total of 30 sets of polarity switch tests, 7 groups of tests clearly show that after the voltage polarity changed, the absorbance of the sulfate-MTB-Ba droplet also changed significantly. It is still unclear under what circumstances this may happen. Woo [116] did an experiment to test the effect of the voltage polarity switch on the capacitance between the top plate conductive layer and the bottom plate conductive layer, with DI water droplets. He found that the polarity switch was always accompanied by a sudden rise in capacitance, and the capacitance could change even when the droplet was stably positioned in the center of the electrode. The reason for the change in capacitance with polarity switching was that when the voltage changes, it causes the droplet to deform and displace the oil film above and below the droplet.

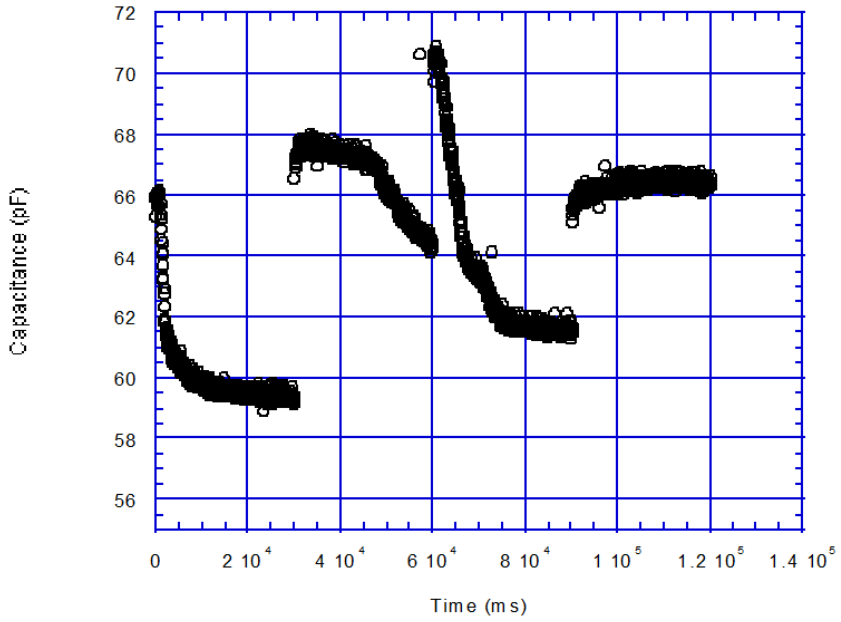

Figure 57: Polarity switching every 30s in oil. Capacitance increased when polarity changed [116].

5.3.1.3 Simulations of oil lens effect on vertical light path

The parameters of an oil lens include its position, size, curvature and thickness. Duke ECE professor Jokerst's lab has the necessary software Zemax (Radiant Zemax LLC,) for ray tracing simulations. A non-sequential model was built and is shown in Figure 58. Objects on the vertical light path are shown from left to right in the horizontal direction, they are bottom plate, water droplet, silicone oil lens, top plate and a circular detector which has the same diameter as the optical fiber. The vertical light path is turned -90 degrees in the figure for easier illustration. Simulation and material parameters are listed in Table 5 The light exiting angle was physically measured. The lens is modeled by a spherical cap, and its center is located on the light path. The round cross section is perpendicular to the light path.

Parameters	
Wavelength (nm)	610
# Analysis rays	10000
Light source power (Lumens)	10
Optical fiber light exiting angle (degree)	8

Materials	Refractive Index
Borosilicate glass	1.47
Silicone oil	1.38
Water	1.33
Acrylic	1.49

Table 5: Parameters used in non-sequential Zemax simulation

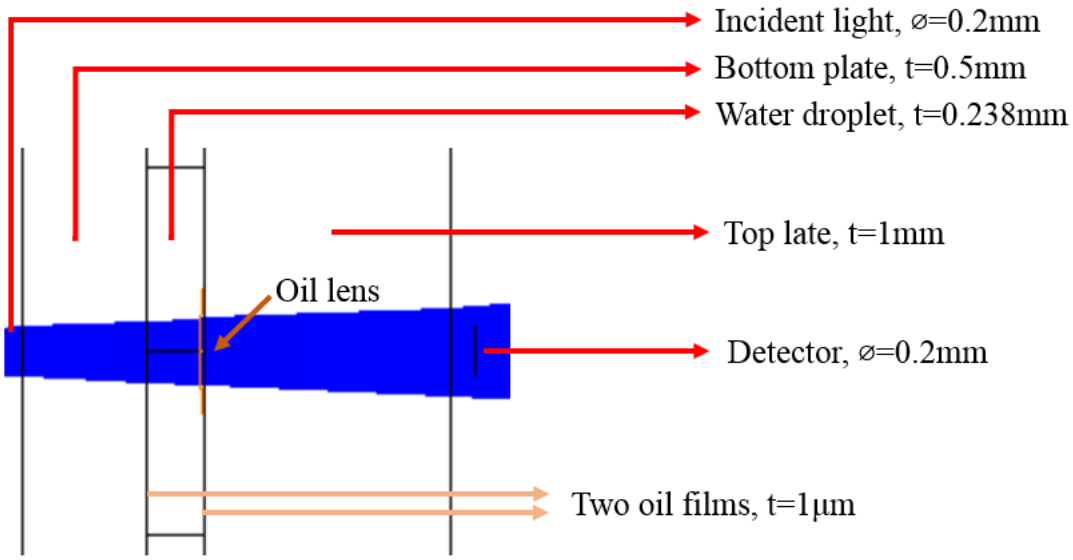

Figure 58: The schematics of the Zemax simulation

Four simulations were designed as follows: simulation1 kept the oil lens diameter at 0.6mm, and varied the oil lens thickness from 0.02 to 0.08 mm; Simulation 2 kept the oil lens diameter at 0.2 mm, and varied the oil lens thickness from 0.005 mm to 0.05 mm; Simulation 3 kept the oil lens diameter at 0.6 mm and thickness at 0.02 mm, and varied the oil lens position (the displacement of the center of the oil lens from the light

path) from 0 to 0.3 mm; Simulation 4 kept the oil lens diameter at 0.2 mm and thickness at 0.02 mm, and varied the oil lens position from 0 to 0.2 mm. Because silicone's refractive index is slightly larger than water, the oil lens has a converging effect and will cause an increase in the total power received by the detector. The amount of this increase is shown as a percentage relative to the power received when there was not any oil lens. Figure 60 shows the results.

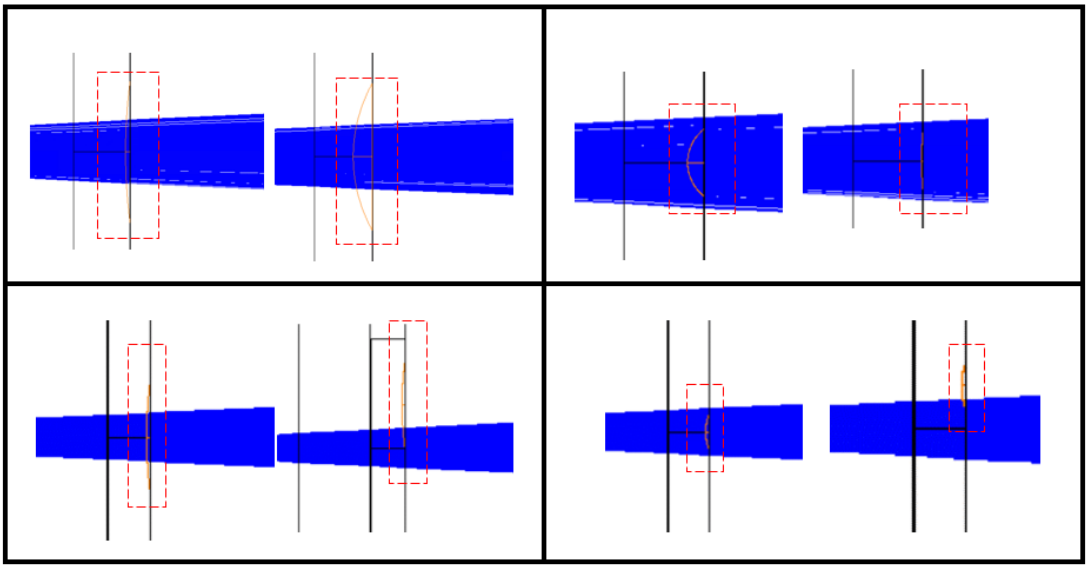

Figure 59: The relative size and thickness of the oil lens. Upper-left: simulation1; upper-right: simulation 2; lower-left: simulation3; lower-right: simulation 4. The orange dotted squares enclose the oil lenses that are also marked with orange lines. The two graphs in each quadrant represent the two extreme situations of the changing variable in the simulation and comparing the two figures reveals how much the thickness or position of the oil lens changes.

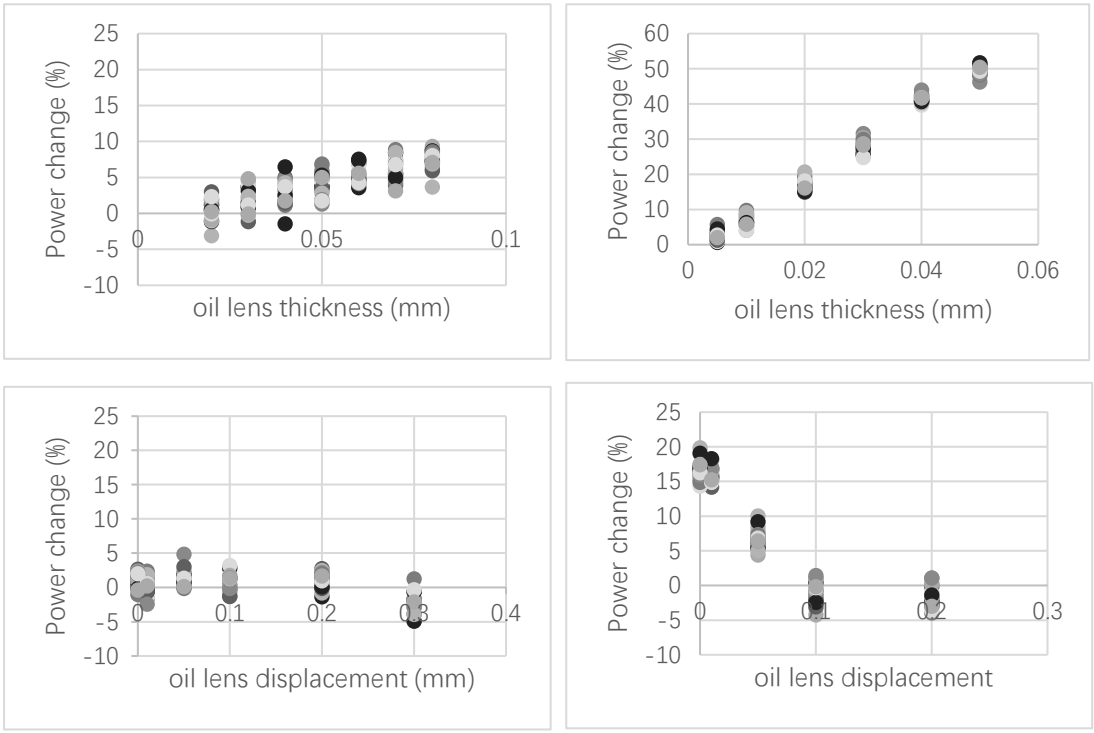

Figure 60: The change of power (in percentage) received by the photo detector plate. Upper-left: simulation1; upper-right: simulation 2; lower-left: simulation3; lower-right: simulation 4.

Several conclusions can be drawn from the results, the most obvious of which is from the largest change in power in simulation 2, where oil lenses with small diameter and large thickness have a great influence on the optical path. A 0.06 mm thick oil lens with 0.2mm diameter can lead to a 50% change in the output light intensity. The second largest power change happened in simulation 4, which shows that the position of the oil lens can make a difference of as much as 20%. It is also important to notice that large flat oil lenses do not affect the output light intensity that much. During previous on-chip absorbance measurement experiments, more than one oil lens had been observed, and the overall effect of oil lens size and position can explain the inconsistency of

absorbance readings between different measurements.

In the vertical direction, the light passes through multiple layers of different media and passes through the oil lens from the center, so the light intensity received at the detector is low and easily affected by the position and surface conditions of these materials. If the optical path is in the horizontal direction, these interferences are eliminated.

5.3.1.4 Simulations of oil lens effect on horizontal light path

To test the feasibility of a horizontal light path, two simulations were performed. For both simulations the oil lens was placed in the center of the surface over the droplet. Simulation 1 kept the oil lens diameter at 0.6mm, and varied the thickness from 0.02-0.08 mm, while simulation 2 kept the oil lens diameter at 0.2mm, and varied the thickness from 0.005-0.05 mm.

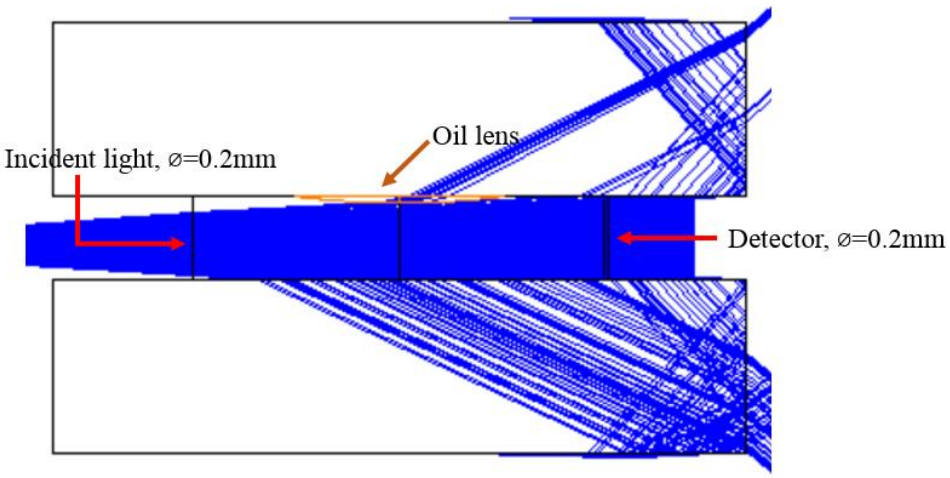

Figure 61: The front-view schematics for horizontal light path simulation.

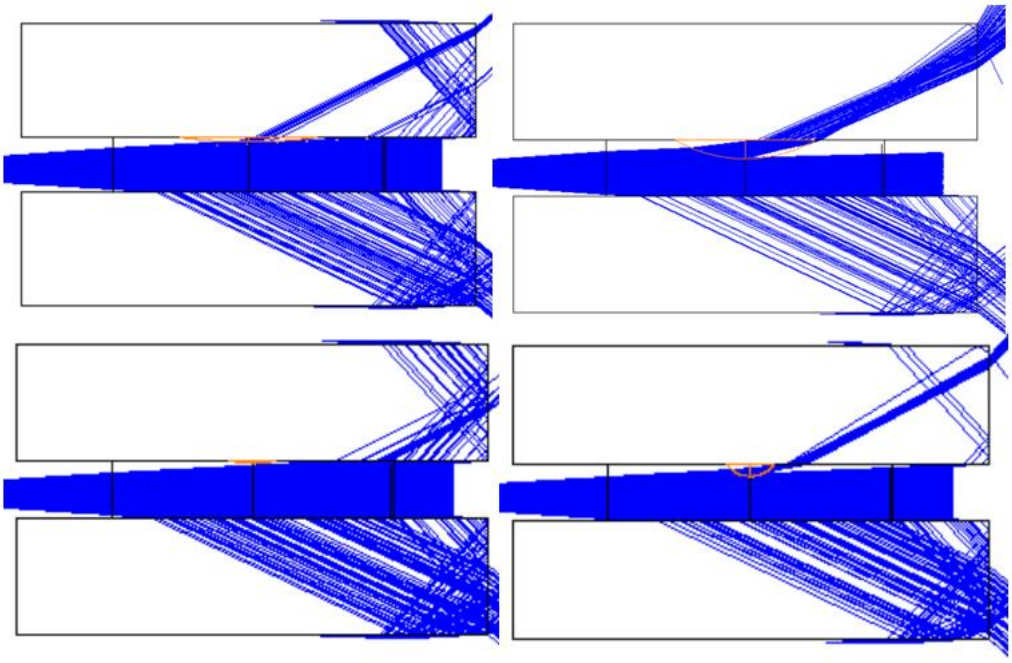

Figure 62: Horizontal light path simulations.

Upper two figures: horizontal light path simulation 1. Lower two figures: horizontal light path simulation 2. These two sets of graphs show the range of changes in the size and position of the oil lens in these two simulations.

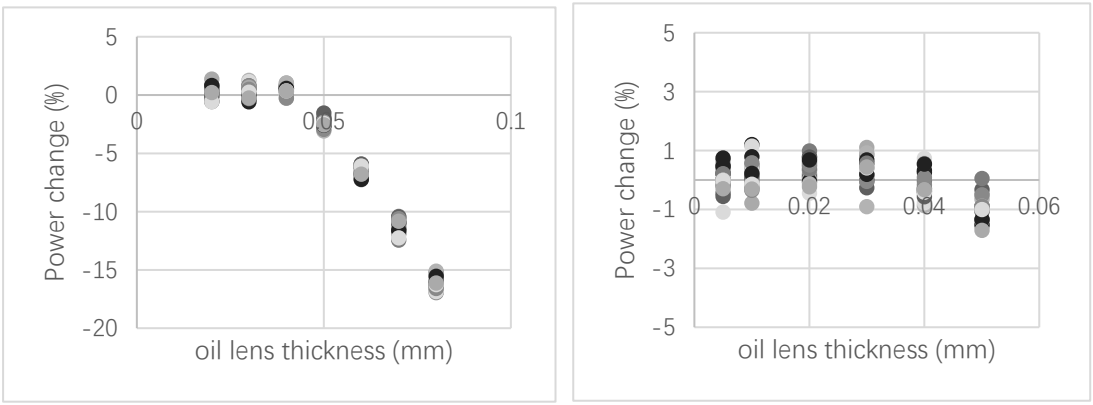

Figure 63: The change of power (in percentage) received by the photo detector plate. Left: simulation 1; right: simulation 2.

The simulations show that the power change caused by oil lens size and thickness was smaller. Therefore, although the appearance and shape of the oil lenses are uncontrollable, these factors do not affect the measurement of the droplet absorbance during a horizontal measurement. Also, smaller oil lens size seems to have less effect. If most of the oil lenses are small, horizontal measurement provides more stable results than vertical measurements. In addition to this, it was found that on average about 80% of the incoming light intensity reached the detector with horizontal measurements, while 45% reached the detector with vertical measurements. Later experiments also confirmed that the light intensity received by the spectrometer in the vertical measurement is much smaller than the light intensity received in the horizontal measurement. This may be because the measurement in the vertical direction requires light to pass through two different materials of the top and bottom plates and the light intensity is reduced by the refraction and reflection at the interfaces.

5.3.2 Horizontal light path measurements

In the previous sections, it was shown that random variation in absorbance measurement was a fatal problem for vertical measurements, and the reason may come from an uneven oil film. To avoid excessive influence of the oil film on the light path, the two optical fibers were moved to the sides of the droplet. There are two advantages to this measurement method: the light path increased from 0.24 mm to 0.7 mm and the uneven oil film between the droplet and the top and bottom plates was no longer in the center of the light path. First, horizontal path measurement stability was tested. MTB-

Ba sulfate solutions were made as in 5.1.1.1 and a final droplet (90 ppm is used) was tested. The droplet was moved in and out of the optical path twenty times, and results showed much more consistent readings than the vertical measurement results, as shown in Figure 64.

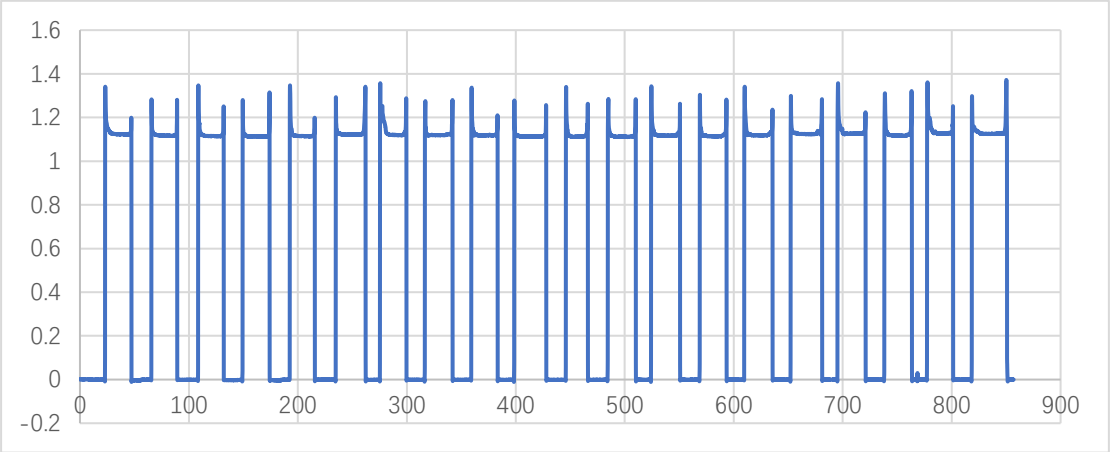

Figure 64: Consistent absorbance readings with horizontal light path for MTB-Ba sulfate solutions

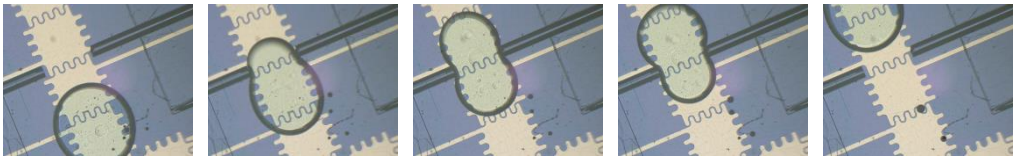

Figure 65: The movement of an MTB-Ba sulfate solution droplet during a measuring period.

Unlike the vertical measurement method, the droplet was maintained between two electrodes. By turning on individual electrodes, it was easy to adjust the droplet position relative to the optical fibers. The entering and exiting movements of the droplet created spikes in absorbance measurements in the graph, and when the droplet was kept at the

detecting position the absorbance values were stable. The optical fibers were in fixed positions, and the droplet deformed to pass between the ends of the fibers, as shown in Figure 65. The ends of the optical fibers must be covered by a hydrophobic coating, so the fibers do not penetrate through the droplet. Otherwise the droplet would be pinned by the hydrophilic fibers, stopping further droplet actuation. It is not recommended to keep the optical fibers spaced apart to create a gap and not touch the droplet, as has been described previously by Wheeler et al. [118], because the round droplet shape will have a lens effect, and the absorbance will be affected by slight change in droplet size and shape.

As expected, the absorbance values from the horizontal measurement path were much higher relative to vertical path measurements due to longer a light path, and the absorbance measurements made after sequential droplet movements were more consistent. Standard deviation of the 20 measurements' averaged is 0.00513, which is at the same level as most vertical measurements (Table 4), but since the average of these 20 measurements for a sulfate concentration of 90 ppm is much higher (1.119), the std/average ratio is 0.459%.

5.4 On-chip Colorimetric Test (with mixing on chip) with Horizontal setup

Up to this point, the horizontal on-chip measurement method produced stable absorbance values using pre-mixed solutions. The final functions of the chip include performing the entire assay on chip, and therefore the next step was to perform the mixing step on chip. To do that, the concentrations of solutions needed adjustment, and

the mixing ratio should be 1:1, since two droplets with the same volume would be moved to the same electrode and mixed. The droplet mixing can be completed in a few seconds and transported to the detection position as soon as the mixing finishes. Even if several measurements are taken to reduce random error, the measurement time takes at most a few minutes. Therefore, the change in solution absorbance over time (Chapter 5.1.2) during the on-chip test can be neglected.

5.4.1 Sulfate colorimetric tests with horizontal setup

The sulfate assay was adjusted to the following steps:

1. Sulfate standard solutions were mixed as in Table 1. The maximum concentration was 120 ppm.
2. 38.15 mg barium chloride powder was added to 25 mL DI water. 18.12 mg methylthymol blue and 0.06 mL 1M hydrochloride acid were added to 2.184 mL of the previously mixed barium chloride solution, and approximately 7 mL methanol was added to bring the final volume to 10 mL.
3. The pH value of this solution was 2.2. In an acidic environment methylthymol blue and barium ions did not form a complex. This solution was mixed with sulfate standard solutions in 1:1 volume ratio on chip. If an aerosol collection step will later be integrated on chip this step can be replaced by dissolving sulfate-containing aerosols.
4. The two droplets must be well-mixed by driving the droplet back and forth in different directions for 10 times. Insufficiently mixed solutions would cause the

final solution to fail to show a linear characteristic. The solubility of MTB is 0.00031g/100g water and MTB is even less soluble in methanol.

5. After the reaction was complete, barium sulfate formed stable precipitates, and the two-electrode-size droplet was then split in two. One droplet was discarded, and the other droplet was mixed with a 1N sodium hydrochloride droplet in 1:1 volume ratio, and the mixture was brought to the detection position.

The pH value of this final droplet was 13.6, and the concentrations in both ion forms and complex forms were:

Sulfate (0-120ppm)	0-0.3125mM
MTB	0.536 mM
Barium	0.341mM

Different ratios of MTB and barium had been used in previous studies. The molar absorptivity of the binuclear complex peaks at the same wavelength but is significantly lower [117]. To prevent binuclear complex forming, the optimal barium-MTB concentration was less than 1.0 [117].

The same sulfate standards where used (Table 1). Each concentration went through the procedures described. The final droplet was moved to the detection position and measured 12 times. Results are shown in Figure 66. The averages and standard deviations for each solution's 12 measurements are shown in Table 6. Compared to previous vertical measurement results, the horizontal absorbance value range increased from 0.005-0.2 to 0.8-2 due to longer light path length. The R^2 value did not change

much, indicating that the low linearity is from the chemistry, not the setup. However, the standard deviation is much smaller, and the ratios of standard deviation to average for six concentrations are less than 3%.

solution #	1(120ppm)	2(90ppm)	3	4	5	6
Average of 12 measurements	0.834	1.076	1.23	1.644	1.942	2.075
Std dev. of 12 measurements	0.00879	0.00386	0.0061	0.011	0.0138	0.0554
Std. dev/average (%)	1.05	0.359	0.496	0.67	0.71	2.67

Table 6: Statistics of horizontal light path absorbances (averaged over measuring periods) for six concentrations of sulfate

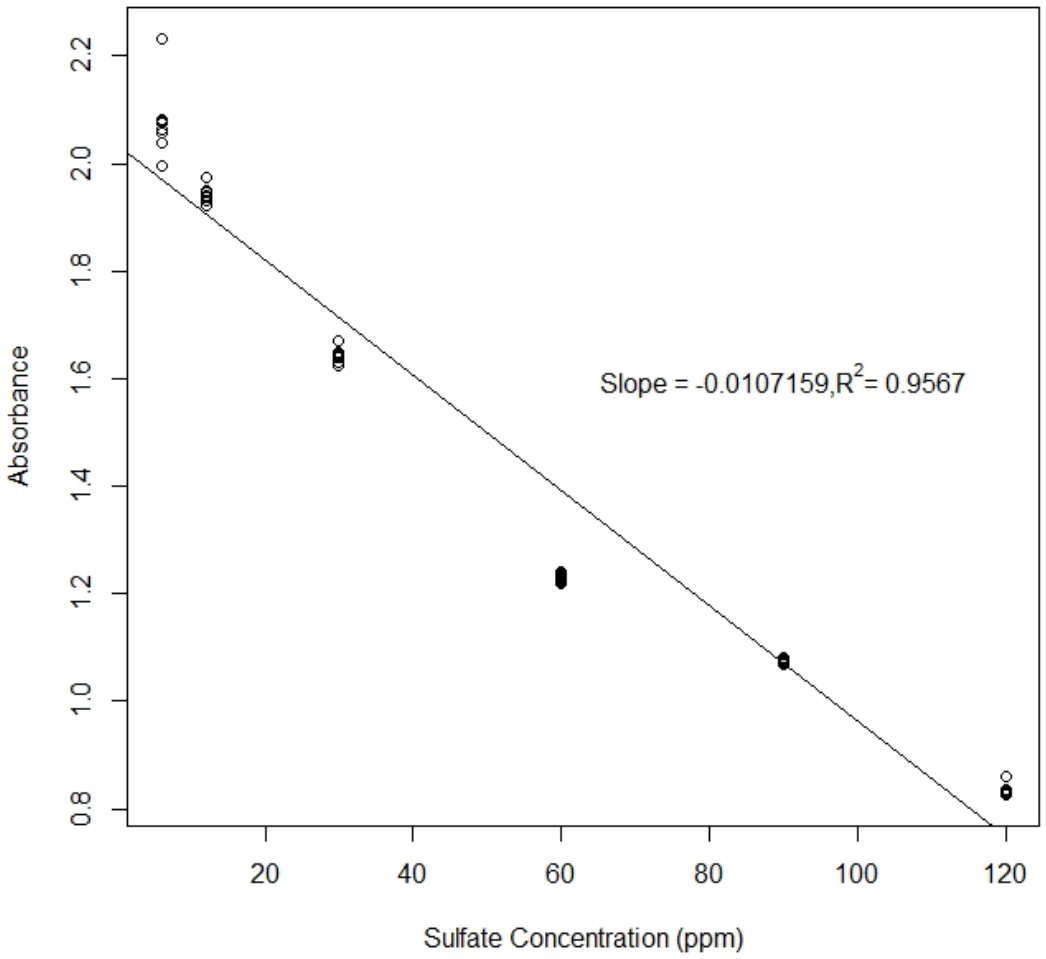

Figure 66: The 12 measured absorbance (averaged over measuring periods) for six concentrations of sulfate

To find the limit of detection, the lowest concentration of MTB-Ba or the highest concentrations of sulfate (120 ppm) was used. The concentration of sulfate was slightly less than barium, thus after these two ions formed precipitates in the reactions, there was very little barium ions left to form MTB-Ba complex in later steps. Measurements were taken for five mixed droplets, each with eight points. The result is shown in figure

67. The standard deviation of all 40 points is 0.041, corresponding to a limit of detection of 11 ppm sulfate.

In comparison with the (off-chip) plate reader results, the on-chip results had a larger slope due to the use of a solution that was not diluted, although the horizontal optical path lengths were substantially the same. The detection limits of the two are at the same level, 7 ppm for off-chip and 11 ppm for on-chip.

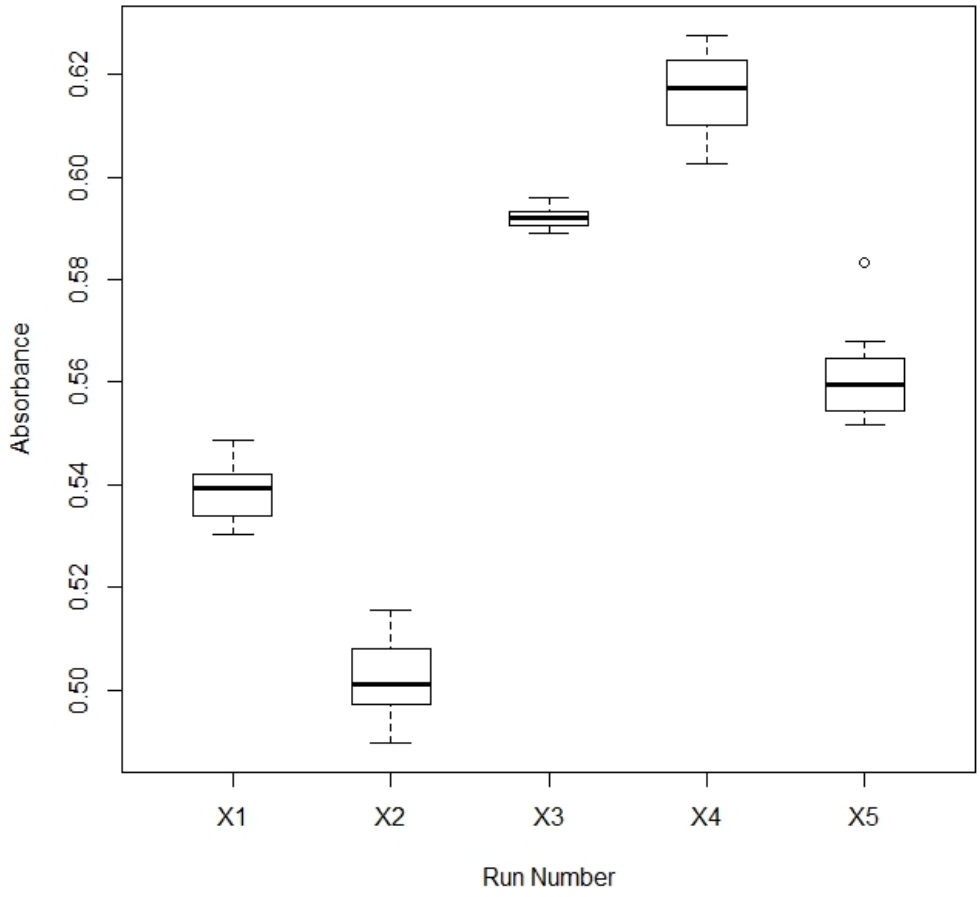

Figure 67: The absorbances by the lowest concentration of sulfate were measured five times, each time 8 measurements (the average over measuring periods) were taken

In this test the methanol results seemed to show two linear ranges, one is 0-60 ppm, another 60-120 ppm, which might indicate that the extinction coefficient based on Beer's law is different. More concentrations were tested to get more points for the linear fit. The results in Figure 68 did not show separate linear regions.

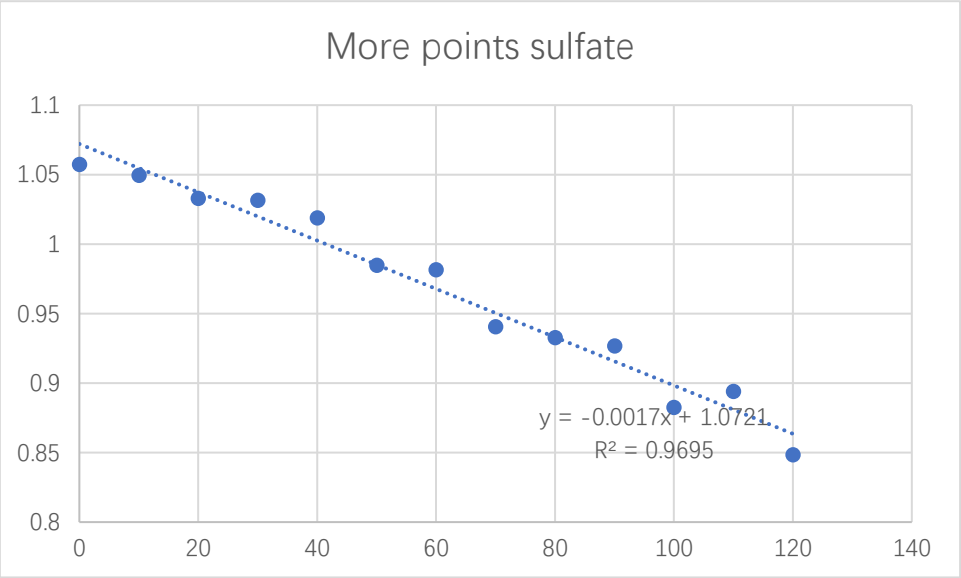

Figure 68: More sulfate concentrations were used to confirm that there are not two linear regions

5.4.2 Ammonium colorimetric tests with horizontal absorbance setup

The ammonium colorimetric tests were adjusted to prepare for equal-volume mixing on chip. The adapted method is as follows:

1. 1000 ppm ammonium chloride stock solution was prepared. Buffer stock solution was prepared by adding 26.8 g sodium phosphate dibasic heptahydrate, 1.5 mL sodium hydroxide, 200 µL formaldehyde solution (37%) and water to make final volume 1L. This buffer solution would last indefinitely.
2. This buffer solution was activated daily by adding 0.138 g of anhydrous sodium

sulfite in 200mL buffer stock solution and would last for weeks.

3. 100 mL OPA solution was prepared by adding 0.143 g OPA, 6.7 mL methanol and DI water to 100 mL. It was sonicated for approximately 1 hour to ensure homogeneity. The ammonium standard solution, the activated buffer solution, and OPA solution were added to three different reservoirs on chip and mixed with 1:1:1 ratio, thus the final droplet covered three-electrodes. When the droplet was moved to the detection place, the droplet did not pass through, but formed an extended part and was measured, as shown in Figure 69. Another way to do this is to split the droplet into smaller sizes so that one droplet is easy to pass between the fibers. Since this is also the case where the liquid completely covers the space between the fibers, the resulting measured absorbance is the same. Only measuring the extension of the droplet here can eliminate the hassle of moving huge droplets (requires at least 5 electrodes) and splitting.

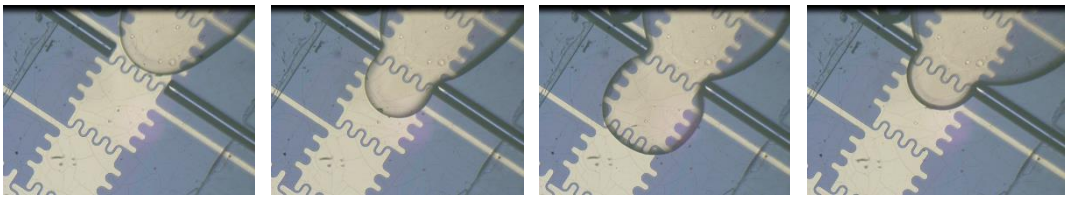

Figure 69: The final droplet of ammonium test covered three-electrodes. During the horizontal measurements, only an extrusion of the droplet is measured.

The ammonium standard concentrations were 0.75, 1.5, 3.75, 7.5, 11.25 and 15ppm. Instead of measuring fluorescence intensity at 422 nm, an absorbance measurement at

365 nm was taken. Each concentration was measured 10 times, and the result is plotted in Figure 70. Absorbance was measured rather than fluorescence, because previous tests in this study were based on absorbance measurements. Also, the intensity of fluorescent emission light was so high that an Ocean Optics spectrometer used to measure the emission saturated, even with the shortest integration time of 3ms.

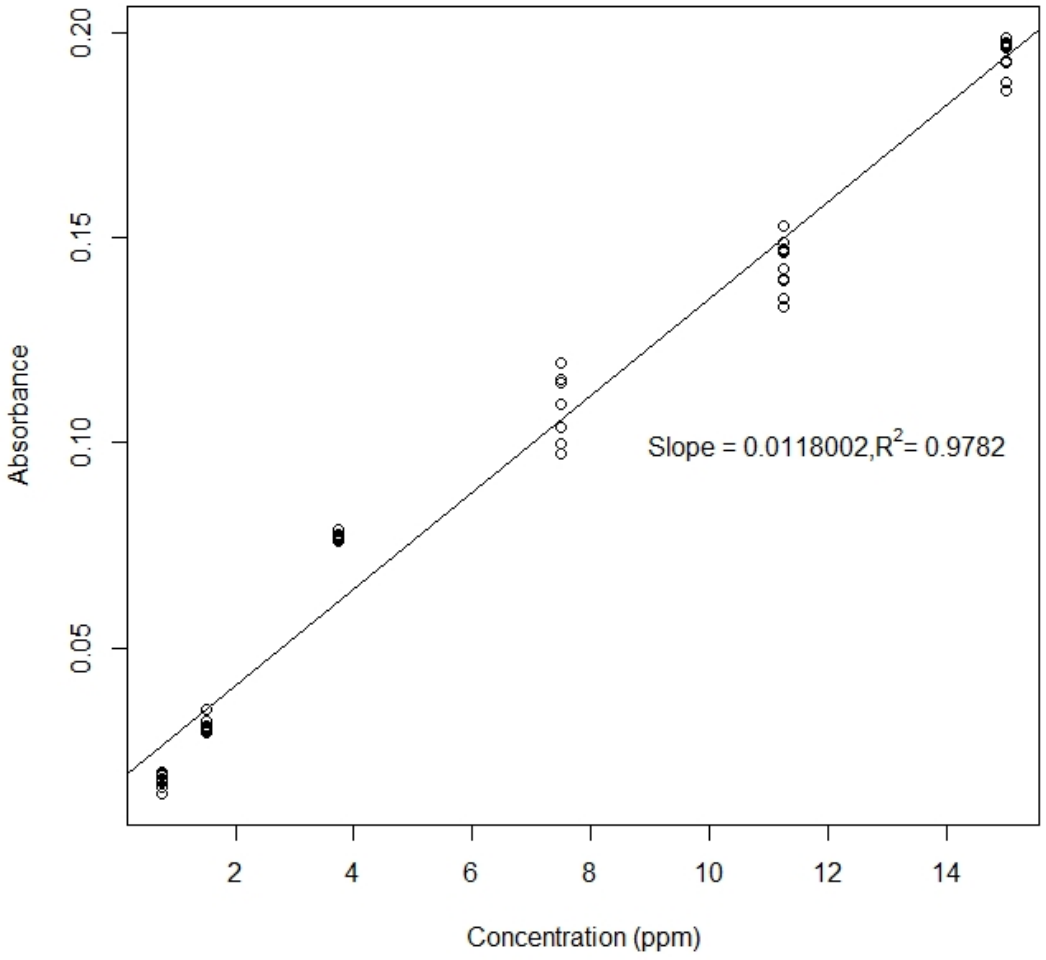

Figure 70: 10 measured absorbance (averaged over measuring periods) for six concentrations of ammonium

The limit of detection test was performed by mixing with the lowest concentration, 0.75 ppm, 5 times, and each mixed droplet was measured 8 times, to get a total of 40 points. The result shows that the standard deviation of all 40 points was 0.0066, corresponding to 0.256 ppm for the limit of detection. This limit of detection and the smallest concentration are of the same order of magnitude, which means that the test was properly designed. Although the plate reader and on-chip methods had similar optical path lengths, the slope obtained on-chip was much smaller. Even though the variance of the measured values by the plate reader measurement method was similar to that of on-chip, the on-chip limit of detection was affected by the slope and was much larger than off-chip (0.0565 ppm). The reason for the small slope is not clear, which may be related to the alignment of the left and right optical paths and the position of the fibers during chip assembly.

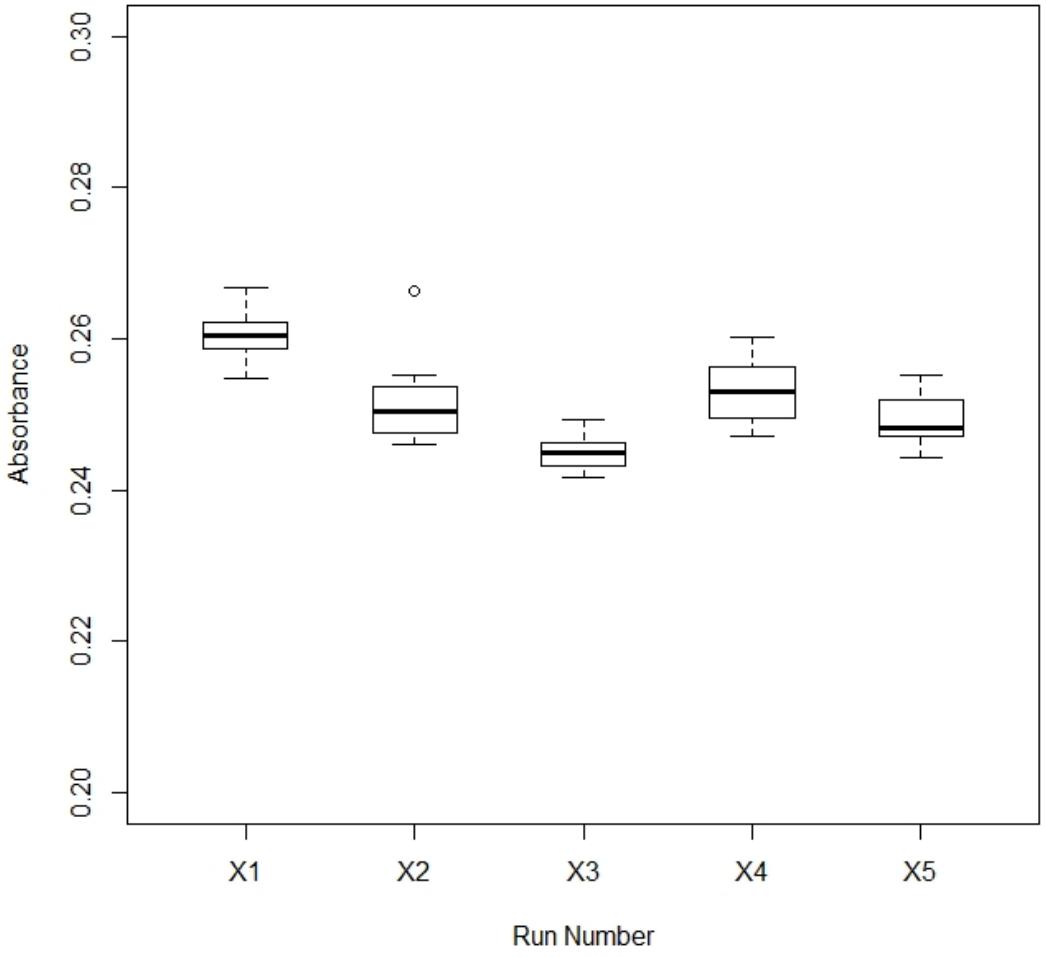

Figure 71: The absorbances by the lowest concentration of ammonium were measured five times, each time 8 measurements (the average over measuring periods) were taken

5.4.3 Nitrate colorimetric tests with horizontal setup

Few changes were made for adapting the nitrate colorimetric test to the last equal-volume mixing step. 440 ppm sodium nitrate (100 ppm nitrate-N) solution was kept as the nitrate stock solution. It was diluted 10 times before use, which would give the

highest concentration of the standard solutions. Further dilution based on Table 1 made the six concentrations 2.2, 4.4, 11, 22, 33, and 44ppm. The reagent chemicals were purchased from NECi nitrate test kit. The assay buffer was 28 mM monopotassium phosphate and 0.025 mM EDTA. 2mg NADH powder was dissolved in 1.5 ml d-I water to form a 2 mM solution. 1 enzyme unit of nitrate reductase and approximately 1ml of diluent was mixed and kept cold during the experiment. The solution that was filled into the first reservoir was mixed with 25 µl nitrate standard solution, 450 µl buffer solution, 25 µl NADH solution and 10 µl nitrate reductase solution. The challenging part was that this solution needed 20 minutes in room temperature for the reduction reaction to complete. For later tests with on-chip aerosol collection, the nitrate standard solution could be substituted with DI water, and the mixed solution would be used to dissolve impacted aerosol particles. This should be followed by a 20 minute on-chip mixing step. With the current set up, the silicone oil evaporated fast through the reservoir top plate openings and needed to be refilled every 5 minutes. 0.15 g sulfanilamide powder was dissolved in 15 ml 3N hydrochloride acid and thoroughly mixed, 30 mg N-Naphthylethylenediamine powder was dissolved in 15 ml d-I water and thoroughly mixed.

The two color reagents (sulfanilamide and N-Naphthylethylenediamine) were introduced to two reservoirs of the chip, and from each a droplet was dispensed. These two droplets mixed with the previous droplet with completely reduced nitrates and the final droplet was sent for absorbance measurements.

However, it was impossible to get stable measurements. As soon as the three solutions

were mixed, dark spots in the droplet were observed, which looked like precipitation. These dark spots seemed to suspend in the droplet and flowed around with the current inside the droplet. The number of dark spots increased significantly during the first three or four minutes after mixing. Although these dark spots were not observed during plate reader tests, they did not disappear when the electrowetting voltage was turned off. Figure 72 shows the process. Figure 73 shows a closer look at the dark spots. Gas bubbles were also observed, but it is not clear where they came from.

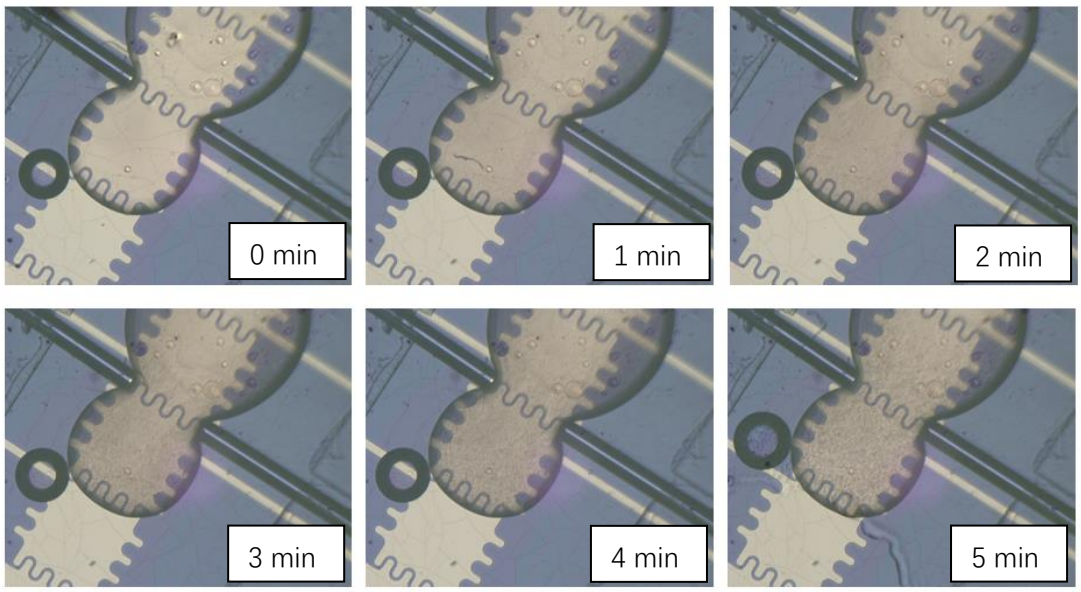

Figure 72: A picture was taken every 1 minute from time=0. The dark precipitation gradually forms during the first several minutes

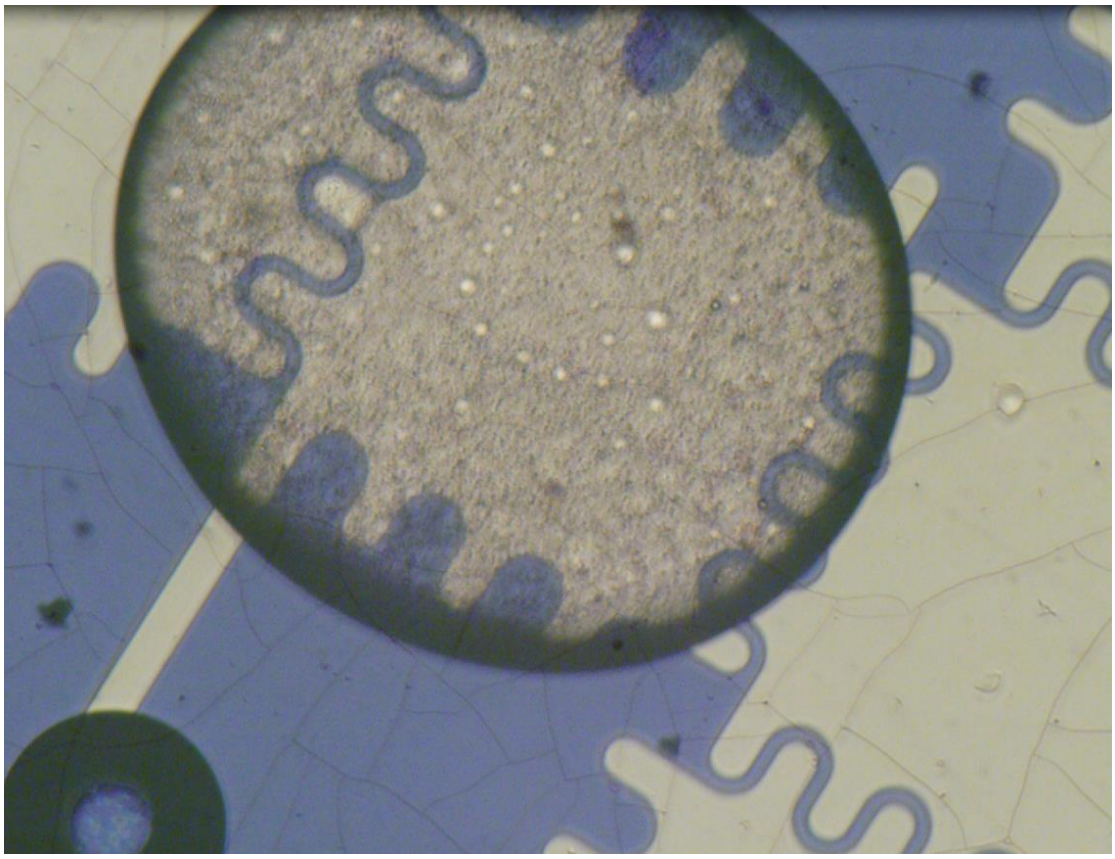

Figure 73: A closer look of the dark precipitation suspended in the droplet. The transparent circles are probably gas bubbles.

The absorbance measurement over time slightly increased during the first three or four minutes. This made it difficult to determine when the Griess test was completed. Otherwise if the readings were the same for several consecutive measurements, the reaction would be complete. However, why the absorbance dropped back after about 150 seconds is not clear. If the five more stable measurements after 150 seconds are plotted, the absorbance and concentration seem to follow the linear relationship of Beer's law, but the R^2 was not as good as non-electrowetting plate reader tests, which means the precipitation phenomenon undermined the sensitivity of this nitrate detection

method. Interestingly, if the first measurement is plotted, which was when the droplet was clear and before forming of the precipitations, a linear relationship is obtained, meaning the droplet was mixed very fast.

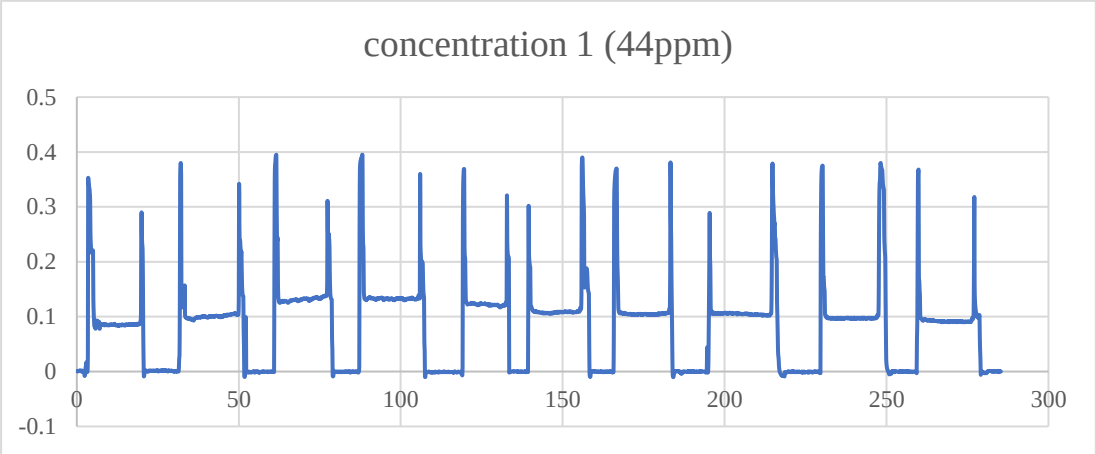

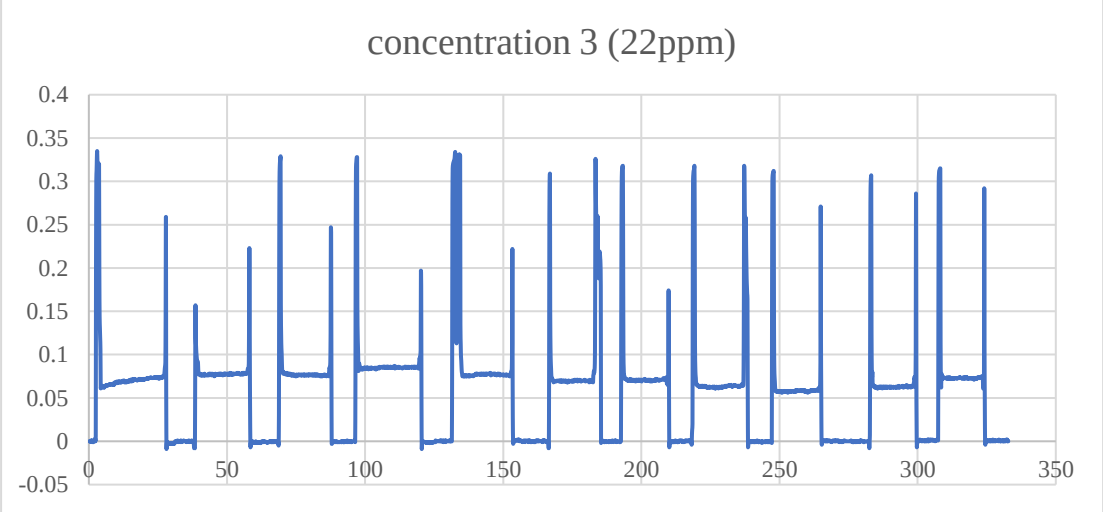

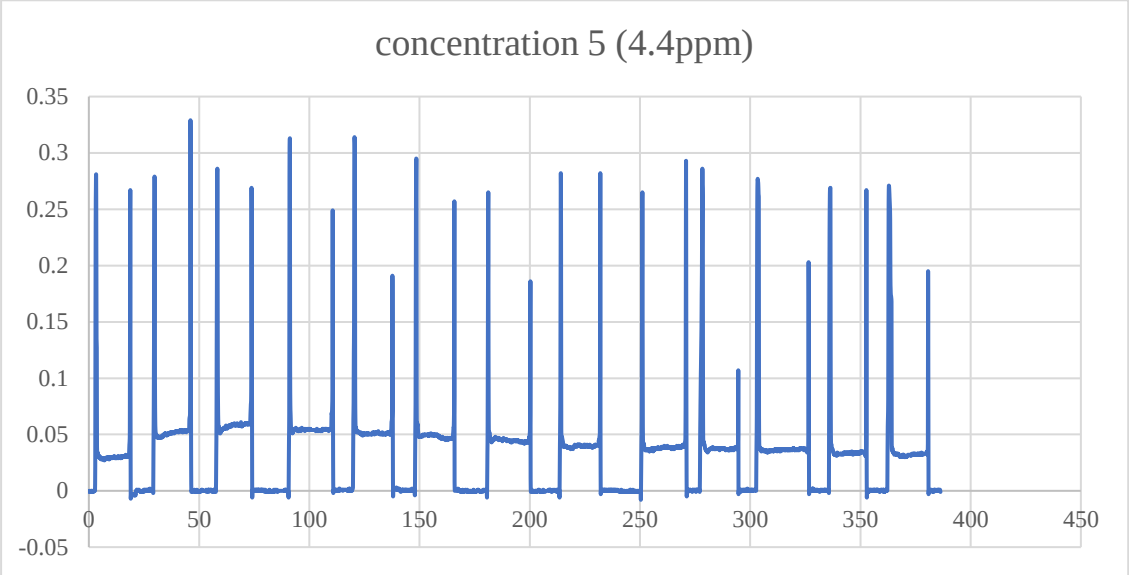

Figure 74: The results of three of the six nitrate concentrations are shown. The absorbance increased during the first two or three minutes, then became stable.

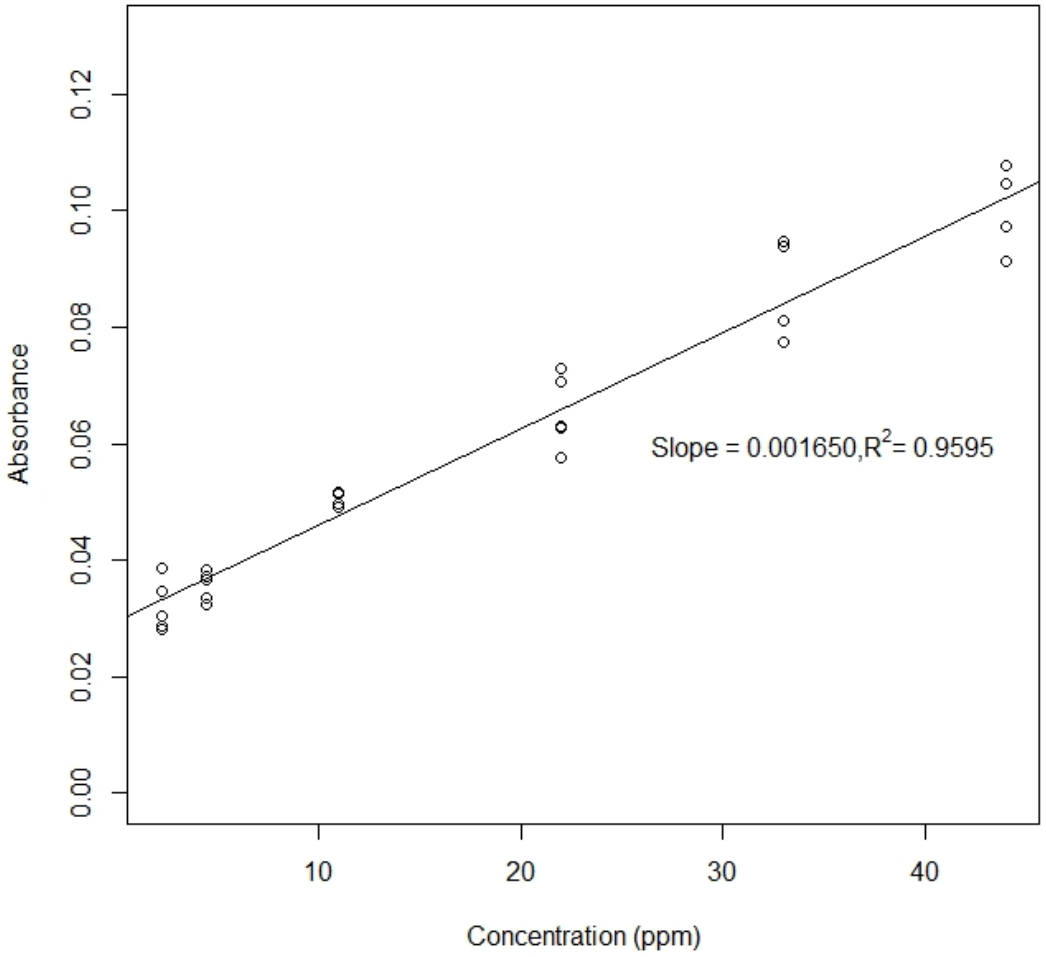

Figure 75: Five consecutive measurements after the absorbance became stable were recorded for each of the six nitrate concentrations.

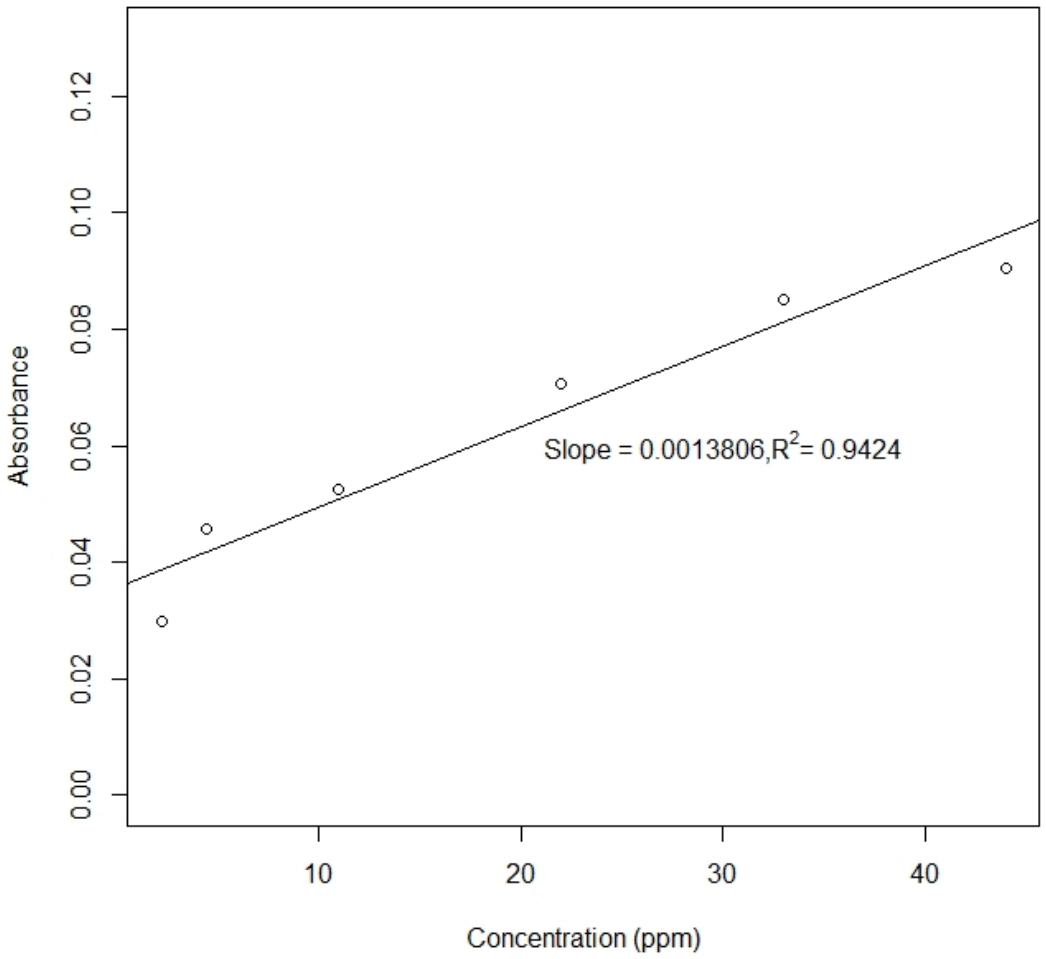

Figure 76: The first measurement (before precipitation, droplet was clear) of six nitrate concentrations

It was observed that the droplet attacked the top plate. Two large droplets were left on a top plate (top plate is 1 mm acrylic covered by 190 nm ITO and 90 nm CYTOP, dried overnight but not baked) and a bottom plate (bottom plate is a normal bottom plate which was covered by 90 nm CYTOP baked at 190℃), separately, for 5 minutes, and were removed with a wipe. The top plate had traces from corrosion, while the bottom

plate was clear. Pseudo chips were made with the same layers but without electrode patterns on glass. The droplet test showed that the yellowish ITO layer was gone, leaving a clear circular shape. This means that the droplet attacked the CYTOP layer, the ITO layer and the acrylic sheet of the top plate all together. The bottom chip was not affected, possibly because the CYTOP coating was baked at 190℃ for 20 minutes and the top plate was not baked because of the low melting temperature of acrylic. The solution is highly acidic, with a less than 2 pH value.

If CYTOP is cured at 190℃ it is resistant to 35% HCl. One of the disadvantages of plastics compared to conventional materials such as metals, ceramics, and glass is that they are often not heat resistant. Heat-resistant plastics generally refer to a class of plastic products with a heat distortion temperature (HDT) above 200℃. However, such plastics tend to have a thermal expansion coefficient much larger than that of the ITO deposit layer, causing cracks during heating. If a transparent, high-temperature resistant plastic can be found, and the conductivity of the ITO layer is ensured by multiple deposition steps, the CYTOP can be heated to make the surface layer more resistant to acid and alkali corrosion. Polyimide (PI) film and cyclic olefin copolymer (COC) may be a good solution.

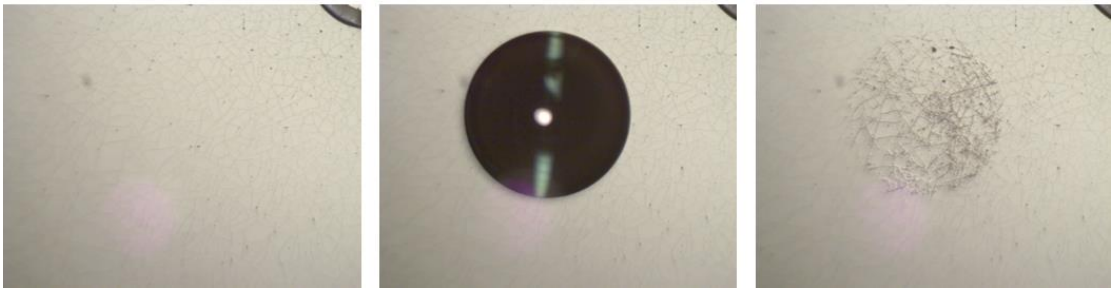

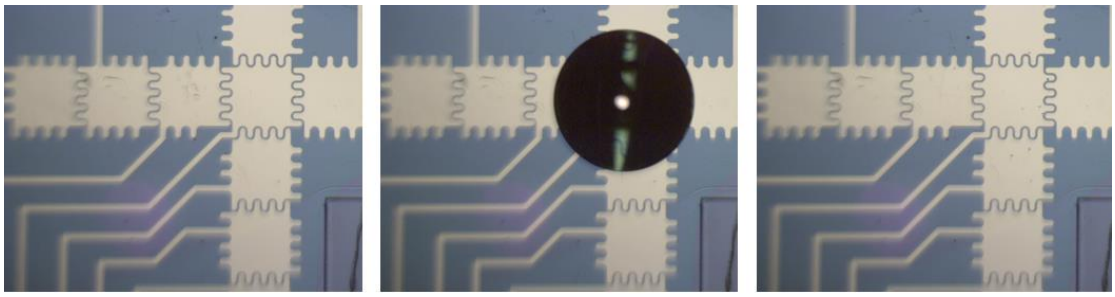

Figure 77: Top plate is attached by the solution.

Top three pictures: top plate. Bottom three pictures: bottom plate. Top plate is covered by 90 nm CYTOP, dried overnight, not baked. Bottom plate is covered with baked CYTOP. From left to right: the plates were in good condition before contact with the solution – the solution settled on the plate surface for 5 minutes – after removing the solution, top plate was damaged while the bottom plate was not.

5.5 Conclusions

Three colorimetric tests for determining the concentration of sulfate, nitrate and ammonium ions in droplet have been performed off chip with a Tecan plate reader and the measured absorption values proved to be described by Beer's law. According to the configuration of the chip, two optical fibers were loaded on the chip in a vertical or horizontal manner to measure the droplet's absorbance. However, the absorbance measurement using the vertical light path was affected by oil lenses caused by the uneven thickness of the oil film between the droplets and the two plates, so that the same droplet produced different absorbance measurements. The law of oil lens generation is still unclear, but it is related to the movement of the droplet and the change of voltage polarity. When the droplet is stationary on an electrode, the shape and

position of the oil lens does not change over time. After changing the optical path to the horizontal direction, the absorbance is less affected by the oil lens and the measured values are stable.

Since the chip supports 1:1 droplet mixing, the reactant concentration is adjusted so that the reactant and the analyte solution can mix on chip in droplet forms. For each analyte the premixed concentrations and solvents were adjusted to adapt to on-chip measurement with shorter light path length and a 1:1 mixing ratio. The vertical light path absorption measurements did not generate consistent absorbance readings due to randomly formed oil lenses. The horizontal light path absorption measurements were more stable. A comparison between the plate reader results and the on-chip results are found in Table 7.

In general, off-chip and on-chip methods generate comparable results, which are reflected in the following aspects: 1) All R^2 values are around 0.96, indicating that the on-chip method can reproduce the linear relationship exhibited in the off-chip method. 2) The limit of detection of the on-chip measurement method is generally several times larger than that obtained by the off-chip method. In the sulfate test, both limits of detection are similar (11 ppm and 7 ppm). However, this is because the sulfate was diluted when tested by the off-chip method, the slope of linear regression was small, which impaired the calculated value of LOD. In the ammonium test, the solution to be tested was not diluted, so the slope of the on-chip method is much smaller than that of off-chip method, making the LOD of on-chip method about 5 times larger. 3) Even though the on-chip LOD is larger, the converted LOD in air by equation (1) is: sulfate

– 6.6ppb, ammonium – 0.15ppb (and nitrate failed due to the problem of the acidic reagent), these numbers are still small enough. Based on the above, the on-chip colorimetric assay can obtain measurements comparable to off-chip methods and can be applied to ion detection in air.

		off-chip (plate reader)	on-chip (horizontal)
sulfate	slope	0.0026	0.0107
	R2	0.9514	0.957
	absorbance range	1.35-1.65	0.8-2.1
	limit of detection	7ppm	11ppm
	Std dev/avg	0.2-4%	0.3-2.7%
nitrate	slope	0.0036	0.00165
	R2	0.9961	0.9595
	absorbance range	0.04-0.18	0.02-0.1
	limit of detection	0.11ppm	N/A
	Std dev/avg	1.5-5%	N/A
ammonium	slope	0.1503	0.0118
	R2	0.9645	0.9782
	absorbance range	0.1-2.3	0.02-0.2
	limit of detection	0.0565ppm	0.256ppm
	Std dev/avg	7-14%	0.4-11.6%

Table 7: Comparison of the performance of Tecan spectrometer and digital microfluidics chip system (horizontal light path, with mixing on chip) on all three colorimetric assays.

Chapter 6 Conclusions

6.1 On-chip Colorimetric Test

By assembling an LED light source, spectrometer and digital microfluidics chip, a new system was created that allows spectrophotometric experiments. Since the measurement on the chip has a short optical path, the absorbance is much smaller than the traditional measurement method, and the slope obtained from the linear regression of absorbance-concentration is much smaller. (Note that in the sulfate test, the final solution sent for off-chip measurement was diluted 4 times, and the resulting slope was similar to the slope measured on chip.) Without dilution, the absorbance would exceed the range of the Tecan spectrometer. Thus, the real off-chip slope should be 4 times of the value obtained).

However, compared to off-chip measurements, the absorbance variance was smaller with on-chip horizontal measurements. This is good for obtaining a large signal-to-noise ratio. The limit of detection from on-chip measurements was not as small as off-chip measurements due to the linear correlation slope being too small. The best result is from the ammonium test. The ammonium concentration range was 0-15 ppm and the limit of detection 0.256 ppm. The sulfate assay has a larger limit of detection, which may come from the chemistry where uncomplexed MTB and complexed MTB have the same absorption peak wavelength. The measured sulfate range was 0-120 ppm and the limit of detection was 11ppm. The limit of detection in solution of 0.256-11 ppm corresponds to the limit of detection in air - on the order of 1 ppb.

6.2 Aerosol Collection and Impaction Efficiency

By applying the design rule of an inertial impactor and reducing the dimensions while keeping Reynolds number in the optimal range, a digital microfluidic impactor was designed on the top plate of the chip. The deposited air particles are densely concentrated in a fixed area and form clear patterns. The collection efficiency is larger than 95%. Air flow rate is 1L/min, and can be easily achieved with a small vacuum pump. Collection time is expected to be less than 1 minute before causing overloading and increasing the pressure difference. However, the ambient aerosol contains a lot of undissolvable components. To perform colorimetric tests later, some kind of filter that can block large particles such as soot should be added to the inlet nozzle of the chip-to-world chamber. Small undissolvable components that can form a uniform suspension in the droplet is allowed, but the absorbance caused by this turbidity should be measured before chemical reaction.

6.3 Contributions

Original design analysis contributions: The DMF chip design and fabrication were done by the author under guidance from Professor Fair and the DMF research group. The design of the top plate aerosol impactor was done by the author under guidance from Professor Andrey Khlystov (Dessert Research Institute). Chip-to-world connections and the optical measurement setup were fabricated by the author with the help of the Duke Student Machine Shop. Aerosol collection experiments were performed by the author together with a master's student Jessica Connolly (Dessert Research Institute).

The chemistry of nitrate and ammonium assays were also developed based on Jessica Connolly's research.

Original contributions from this work include the following:

- A miniaturized aerosol detection system based on digital microfluidics was designed and fabricated for on-line analysis of sulfate, nitrate and ammonium. It combined aerosol impaction, extraction and chemical detection on the same chip in real time.
- Conducted a co-design of particle impaction, collection and chemical detection elements integrated on a common microfluidic platform. Fabricated these elements and tested them on the microfluidic platform.
- Developed scientific theory and analysis of droplet extraction through an oil/air interface
- Designed an impaction region that allows droplet scanning of the impaction area with a five-fold particle concentration enhancement without droplet pinning at impactor nozzles.
- Developed an analysis on the effect of oil film instabilities on vertical absorption measurements of sulfate concentration, and demonstrated theoretically and experimentally that horizontal light path measurements allowed for stable measurements.
- Designed and experimentally tested an inertial digital microfluidic impactor by scaling dimensions while keeping Reynolds number in the optimal range. The

deposited air particles were densely concentrated in a fixed area and formed clear patterns. The collection efficiency was larger than 95%.

6.4 Future Work

First, the cause of the formation of small particles in the nitrate test is unclear. Possible solutions could be to reduce the acidity of the solution or use a perforated glass plate as the top plate so that the CYTOP can be heated to the glass transition temperature and can withstand solutions with very small pH value.

It is not yet possible to automate all the steps from aerial collection to detection. After collecting aerosol, it is still necessary to manually move the chip onto the electrowetting platform for testing. The next step would be to integrate the electrowetting platform with the aerosol collection platform. The chip-to-world chamber should be redesigned to have external electrode connections so that the chip could perform colorimetric assays without being physically removed from a collection location to a testing location. The chamber should also hold the optical fibers, LED and the spectrometer.

If three sets of measurements of three different analytes are to be completed on chip at the same time, the number of reservoirs of the chip should be increased by three times. From the dispensing of the aerosol collection droplet, three separate channels should be formed, although they can share the same impaction area and absorbance measurement place. A two-conductive layer chip would be ideal to fit more electrodes on a small chip area. Current technology limits the lifetime of the device. The sputtered ITO layer shows many cracks, which may come from a large coefficient of thermal expansion of

acrylic or the fact that acrylic is flexible and may slightly deform during handling. Also, the parylene insulator deposition was not done in the clean room, and the chip may collect particles in the air and make the parylene surface uneven. The quality of fabricated chips varies. A good chip can last during a few days of experiment, but a poor chip may either fail to electrowet even with the maximum voltage, or else show dielectric breakdown. These issues must be addressed before moving towards fabricating a full-featured chip.

To test the applicability of the chip for aircraft studies, the chip needs to operate stably under low pressure and motion. The air pump needs to maintain a constant air flow rate with different air pressures at different altitudes. The movement of the aircraft includes acceleration and deceleration in all directions, as well as axial rotation. To ensure the normal operation of the chip, the limit of these physical quantities need to be determined experimentally.

Bibliography

[1] Hinds, W. C. (1999). Aerosol Technology: Properties. Behavior, and Measurement of airborne Particles

[2] Sîrbu, A., Loreto, V., Servedio, V. D., & Tria, F. (2017). Opinion dynamics: models, extensions and external effects. In Participatory Sensing, Opinions and Collective Awareness (pp. 363-401). Springer, Cham.

[3] 1, Stöber, W. (1971). A note on the aerodynamic diameter and the mobility of non-spherical aerosol particles. Journal of Aerosol Science, 2(4), 453-456.

[4] Gibbs, A. R., & Pooley, F. D. (1996). Analysis and interpretation of inorganic mineral particles in" lung" tissues. Thorax, 51(3), 327-334.

[5] Henze, D. K., Seinfeld, J. H., & Shindell, D. T. (2009). Inverse modeling and mapping US air quality influences of inorganic PM 2.5 precursor emissions using the adjoint of GEOS-Chem. Atmospheric Chemistry and Physics, 9(16), 5877-5903.

[6] Kim, H. S., Huh, J. B., Hopke, P. K., Holsen, T. M., & Yi, S. M. (2007). Characteristics of the major chemical constituents of PM2. 5 and smog events in Seoul, Korea in 2003 and 2004. Atmospheric Environment, 41(32), 6762-6770.

[7] Pope III, C. A., Burnett, R. T., Thun, M. J., Calle, E. E., Krewski, D., Ito, K., & Thurston, G. D. (2002). Lung cancer, cardiopulmonary mortality, and long-term exposure to fine particulate air pollution. Jama, 287(9), 1132-1141.

[8] Cohen, A. J., Brauer, M., Burnett, R., Anderson, H. R., Frostad, J., Estep, K., ... & Feigin, V. (2017). Estimates and 25-year trends of the global burden of disease attributable to ambient air pollution: an analysis of data from the Global Burden of Diseases Study 2015. The Lancet, 389(10082), 1907-1918.

[9] Congress, U. S. (1990). Clean air act amendments of 1990. Public Law, 1990, 101-549.

[10] NAAQS Table, https://www.epa.gov/criteria-air-pollutants/naaqs-table

[11] Park, R. J., Jacob, D. J., Field, B. D., Yantosca, R. M., & Chin, M. (2004). Natural and transboundary pollution influences on sulfate‐nitrate‐ammonium aerosols in the United States: Implications for policy. Journal of Geophysical Research: Atmospheres, 109(D15).

[12] Harrison, R. M., Jones, A. M., & Lawrence, R. G. (2004). Major component composition of PM10 and PM2. 5 from roadside and urban background

sites. Atmospheric Environment, 38(27), 4531-4538.

[13] Pöschl, U. (2005). Atmospheric aerosols: composition, transformation, climate and health effects. Angewandte Chemie International Edition, 44(46), 7520-7540.

[14] Querol, X., Alastuey, A., Rodriguez, S., Plana, F., Mantilla, E., & Ruiz, C. R. (2001). Monitoring of PM10 and PM2. 5 around primary particulate anthropogenic emission sources. Atmospheric Environment, 35(5), 845-858.

[15] Huang, R. J., Zhang, Y., Bozzetti, C., Ho, K. F., Cao, J. J., Han, Y., ... & Zotter, P. (2014). High secondary aerosol contribution to particulate pollution during haze events in China. Nature, 514(7521), 218.

[16] Li, Xue, Zhen Zhou, Zhengxu Huang, Wei Gao, Mei Li, and Lei Li. "Techniques and instruments used for real-time analysis of atmospheric nanoscale molecular clusters: A review." Emerging Contaminants 1, no. 1 (2015): 33-38.

[17] Kulkarni, P., Baron, P. A., & Willeke, K. (Eds.). (2011). Aerosol measurement: principles, techniques, and applications. John Wiley & Sons.

[18] Cornelis, Rita, Joseph A. Caruso, Helen Crews, and Klaus G. Heumann. Handbook of elemental speciation II: species in the environment, food, medicine and occupational health. John Wiley & Sons, 2005.

[19] Mester, Z., & Sturgeon, R. E. (2003). Sample preparation for trace element analysis (Vol. 41). Elsevier.

[20] Clement, R. E., Yang, P. W., & Koester, C. J. (1999). Environmental analysis. Analytical chemistry, 71(12), 257-292.

[21] Scaringelli, F. P., & Rehme, K. A. (1969). Determination of atmospheric concentrations of sulfuric acid aerosol by spectrophotometry, coulometry, and flame photometry. Analytical chemistry, 41(6), 707-713.

[22] Crider, W. L. (1965). Hydrogen flame emission spectrophotometry in monitoring air for sulfur dioxide and sulfuric acid aerosol. Analytical Chemistry, 37(13), 1770-1773.

[23] Yongchun, L., & Hong, H. (2007). Analysis of chemical composition of atmospheric particles.

[24] Slanina, J., Schoonebeek, C. A., Klockow, D., & Niessner, R. (1985). Determination of sulfuric acid and ammonium sulfates by means of a computer-controlled thermo-denuder system. Analytical Chemistry, 57(9), 1955-1960.

[25] Orsini, D. A., Ma, Y., Sullivan, A., Sierau, B., Baumann, K., & Weber, R. J. (2003). Refinements to the particle-into-liquid sampler (PILS) for ground and airborne

measurements of water soluble aerosol composition. Atmospheric Environment, 37(9-10), 1243-1259.

[26] Product information form TSI ®

http://www.tsi.com/uploadedFiles/Product_Information/Literature/Spec_Sheets/3800SeriesPN1933798RevD.pdf

[27] Verpoorte, E., & De Rooij, N. F. (2003). Microfluidics meets MEMS. Proceedings of the IEEE, 91(6), 930-953.

[28] Zhao, X. M., Xia, Y., & Whitesides, G. M. (1996). Fabrication of three‐dimensional micro‐structures: Microtransfer molding. Advanced Materials, 8(10), 837-840.

[29] Fair, R. B. (2007). Digital microfluidics: is a true lab-on-a-chip possible?. Microfluidics and Nanofluidics, 3(3), 245-281.

[30] Lippmann, G. (1875). Relations entre les phénomènes électriques et capillaires (Doctoral dissertation, Gauthier-Villars).

[31] Bruno, B. (1993). Electrocapillarité et mouillage de films isolants par l'eau. Comptes Rendus de L'Academie des Sciences Paris, Serie, II, 317, 157-163.

[32] Khenissi, H. Sulfur isotopic composition and concentration in throughfall.

[33] Quinn, A., Sedev, R., & Ralston, J. (2005). Contact angle saturation in electrowetting. The journal of physical chemistry B, 109(13), 6268-6275.

[34] Chiou, C. H., & Lee, G. B. (2004). Minimal dead-volume connectors for microfluidics using PDMS casting techniques. Journal of Micromechanics and Microengineering, 14(11), 1484.

[35] Skinner, C., Tang, T., Harrison, D. J., Bings, N., Wang, C., Ocvirk, G., ... & Thibault, P. (2003). U.S. Patent No. 6,605,472. Washington, DC: U.S. Patent and Trademark Office.

[36] Hua, Z., Rouse, J. L., Eckhardt, A. E., Srinivasan, V., Pamula, V. K., Schell, W. A., ... & Pollack, M. G. (2010). Multiplexed real-time polymerase chain reaction on a digital microfluidic platform. Analytical chemistry, 82(6), 2310-2316.

[37] Witters, D., Sun, B., Begolo, S., Rodriguez-Manzano, J., Robles, W., & Ismagilov, R. F. (2014). Digital biology and chemistry. Lab on a Chip, 14(17), 3225-3232.

[38] May, K. R. (1945). The cascade impactor: an instrument for sampling coarse aerosols. Journal of Scientific instruments, 22(10), 187.

[39] Heidam, N. Z. (1981). Aerosol fractionation by sequential filtration with Nuclepore filters. Atmospheric Environment (1967), 15(6), 891-904.

[40] Saltzman, B. E., & Hochstrasser, J. M. (1983). Design and performance of miniature cyclones for respirable aerosol sampling. Environmental science & technology, 17(7), 418-424.

[41] Noone, K. J., Ogren, J. A., Heintzenberg, J., Charlson, R. J., & Covert, D. S. (1988). Design and calibration of a counterflow virtual impactor for sampling of atmospheric fog and cloud droplets. Aerosol Science and Technology, 8(3), 235-244.

[42] Loo, B. W., & Cork, C. P. (1988). Development of high efficiency virtual impactors. Aerosol Science and Technology, 9(3), 167-176.

[43] Marple, V. A., & Chien, C. M. (1980). Virtual impactors: a theoretical study. Environmental science & technology, 14(8), 976-985.

[44] Marple, V. A., & Liu, B. Y. (1974). Characteristics of laminar jet impactors. Environmental Science & Technology, 8(7), 648-654.

[45] Marle, L., & Greenway, G. M. (2005). Microfluidic devices for environmental monitoring. TrAC Trends in Analytical Chemistry, 24(9), 795-802.

[46] Marple, V. A., & Willeke, K. (1976). Impactor design. Atmospheric Environment (1967), 10(10), 891-896.

[47] May, K. R. (1945). The cascade impactor: an instrument for sampling coarse aerosols. Journal of Scientific instruments, 22(10), 187.

[48] Kavouras, I. G., Ferguson, S. T., Wolfson, J. M., & Koutrakis, P. (2000). Development and validation of a high-volume, low-cutoff inertial impactor. Inhalation Toxicology, 12(sup2), 35-50.

[49] Kim, Y. H., Park, D., Hwang, J., & Kim, Y. J. (2009). A hybrid chip based on aerodynamics and electrostatics for the size-dependent classification of ultrafine and nano particles. Lab on a Chip, 9(18), 2722-2728.

[50] Fuchs, N. A. (1975). Sampling of aerosols. Atmospheric Environment (1967), 9(8), 697-707.

[51] Hinds, W. C. (2012). Aerosol technology: properties, behavior, and measurement of airborne particles. John Wiley & Sons.

[52] Marple, V. A., & Rubow, K. L. (1986). Theory and Design Guidelines, Cascade Impactors: Sampling & Data Analysis. JP Lodge Jr., TL Chan, 79-101.

[53] Ceyssens, F., Witters, D., Van Grimbergen, T., Knez, K., Lammertyn, J., & Puers,

R. (2013). Integrating optical waveguides in electrowetting-on-dielectric digital microfluidic chips. Sensors and Actuators B: Chemical, 181, 166-171.

[54] Patnaik, P. (2010). Handbook of environmental analysis: chemical pollutants in air, water, soil, and solid wastes. Crc Press.

[55] Miller, J. J., & Curtin, D. (2006). Electrical conductivity and soluble ions. Soil sampling and methods of analysis, 2.

[56] Colorimetry, D. O. S. B. A. (1993). Method 375.2 Determination of Sulfate By Automated Colorimetry.

[57] EPA Method 9028 (1986). Sulfate – Turbidimetric

[58] EPA Method 352.1 (1993). Nitrogen, Nitrate - Colorimetric, Brucine

[59] EPA Method 200.8 (1994). Trace elements in waters & wastes/ ICP MS

[60] Michalski, R., & Kurzyca, I. (2006). Determination of Nitrogen Species (Nitrate, Nitrite and Ammonia Ions) in Environmental Samples by Ion Chromatography. Polish Journal of Environmental Studies, 15(1).

[61] Chow, J. C., & Watson, J. G. (1999). Ion chromatography in elemental analysis of airborne particles. Elemental analysis of airborne particles, 1, 97-137.

[62] Swinehart, D. F. (1962). The beer-lambert law. Journal of chemical education, 39(7), 333.

[63] Lambert, J.H., Photometrie: Photometria, sive de mensura et gradibus luminis, colorum

et umbrae. the Bavarian State Library, 1760. Cited on: p. 1.

[64] Beer, (1852), Bestimmung der Absorption des rothen Lichts in farbigen Flüssigkeiten. Ann. Phys., 162: 78-88. doi:10.1002/andp.18521620505

[65] Fuwa, K., & Valle, B. L. (1963). The Physical Basis of Analytical Atomic Absorption Spectrometry. The Pertinence of the Beer-Lambert Law. Analytical Chemistry, 35(8), 942-946.

[66] Cannon, C. G., & Butterworth, I. S. C. (1953). Beer's law and spectrophotometer linearity. Analytical Chemistry, 25(1), 168-170.

[67] Madsen, B. C., & Murphy, R. J. (1981). Flow injection and photometric determination of sulfate in rainwater with methylthymol blue. Analytical Chemistry, 53(12), 1924-1926.

[68] EPA Method 375.2, Revision 2.0: Determination of Sulfate by Automated

Colorimetry

[69] EPA Method 9036, SULFATE (COLORIMETRIC, AUTOMATED, METHYLTHYMOL BLUE, AA II)

[70] Jaworski, E. G. (1971). Nitrate reductase assay in intact plant tissues. Biochemical and biophysical research communications, 43(6), 1274-1279.

[71] Miranda, K. M., Espey, M. G., & Wink, D. A. (2001). A rapid, simple spectrophotometric method for simultaneous detection of nitrate and nitrite. Nitric oxide, 5(1), 62-71.

[72] Guevara, I., Iwanejko, J., Dembińska-Kieć, A., Pankiewicz, J., Wanat, A., Anna, P., ... & Szczudlik, A. (1998). Determination of nitrite/nitrate in human biological material by the simple Griess reaction. Clinica Chimica Acta, 274(2), 177-188.

[73] Dillon, J. H. (1990). The modified Griess test: a chemically specific chromophoric test for nitrite compounds in gunshot residues. AFTE Journal, 22(3), 243-50.24

[74] Guevara, I., Iwanejko, J., Dembińska-Kieć, A., Pankiewicz, J., Wanat, A., Anna, P., ... & Szczudlik, A. (1998). Determination of nitrite/nitrate in human biological material by the simple Griess reaction. Clinica Chimica Acta, 274(2), 177-188.

[75] Campbell, W. H. (1999). Nitrate reductase structure, function and regulation: bridging the gap between biochemistry and physiology. Annual review of plant biology, 50(1), 277-303.

[76] Mellor, R. B., Ronnenberg, J., Campbell, W. H., & Diekmann, S. (1992). Reduction of nitrate and nitrite in water by immobilized enzymes. Nature, 355(6362), 717.

[77] Green, L. C., Wagner, D. A., Glogowski, J., Skipper, P. L., Wishnok, J. S., & Tannenbaum, S. R. (1982). Analysis of nitrate, nitrite, and [15N] nitrate in biological fluids. Analytical biochemistry, 126(1), 131-138.

[78] Ivančič, I., & Degobbis, D. (1984). An optimal manual procedure for ammonia analysis in natural waters by the indophenol blue method. Water Research, 18(9), 1143-1147.

[79] EPA method 350.1, Determination of Ammonia Nitrogen by Semi-Automated Colorimetry

[80] Niedzielski, P., Kurzyca, I., & Siepak, J. (2006). A new tool for inorganic nitrogen speciation study: Simultaneous determination of ammonium ion, nitrite and nitrate by ion chromatography with post-column ammonium derivatization by Nessler reagent and diode-array detection in rain water samples. Analytica chimica acta, 577(2), 220-224.

[81] Molins-Legua, C., Meseguer-Lloret, S., Moliner-Martinez, Y., & Campins-Falco, P. (2006). A guide for selecting the most appropriate method for ammonium determination in water analysis. TrAC Trends in Analytical Chemistry, 25(3), 282-290.

[82] Holmes, R. M., Aminot, A., Kérouel, R., Hooker, B. A., & Peterson, B. J. (1999). A simple and precise method for measuring ammonium in marine and freshwater ecosystems. Canadian Journal of Fisheries and Aquatic Sciences, 56(10), 1801-1808.

[83] Holmes, R. M., Aminot, A., Kérouel, R., Hooker, B. A., & Peterson, B. J. (1999). A simple and precise method for measuring ammonium in marine and freshwater ecosystems. Canadian Journal of Fisheries and Aquatic Sciences, 56(10), 1801-1808.

[84] Aminot, A., Kérouel, R., & Birot, D. (2001). A flow injection-fluorometric method for the determination of ammonium in fresh and saline waters with a view to in situ analyses. Water Research, 35(7), 1777-1785.

[85] Chen, G., Zhang, M., Zhang, Z., Huang, Y., & Yuan, D. (2011). On-line solid phase extraction and spectrophotometric detection with flow technique for the determination of nanomolar level ammonium in seawater samples. Analytical letters, 44(1-3), 310-326.

[86] Srinivasan, V., Pamula, V. K., & Fair, R. B. (2004). Droplet-based microfluidic lab-on-a-chip for glucose detection. Analytica Chimica Acta, 507(1), 145-150.

[87] Jung, D. G., Jung, D., & Kong, S. H. (2017). A Lab-on-a-Chip-Based Non-Invasive Optical Sensor for Measuring Glucose in Saliva. Sensors, 17(11), 2607.

[88] Chang-Yen, D. A., Eich, R. K., & Gale, B. K. (2005). A monolithic PDMS waveguide system fabricated using soft-lithography techniques. Journal of lightwave technology, 23(6), 2088.

[89] Cai, Z., Qiu, W., Shao, G., & Wang, W. (2013). A new fabrication method for all-PDMS waveguides. Sensors and Actuators A: Physical, 204, 44-47.

[90] Bêche, B., Pelletier, N., Gaviot, E., & Zyss, J. (2004). Single-mode TE00–TM00 optical waveguides on SU-8 polymer. Optics Communications, 230(1-3), 91-94.

[91] R. B. Fair, A. Khlystov, V. Srinivasan, V. K. Pamula and K. N. Weaver,(2004) Lab-on-a-Chip: Platforms, Devices, and Applications, Pro-ceedings of SPIE, Philadelphia, pp. 113–124

[92] V. Babin and R. Holyst, (2005) Evaporation of a Sub-Micrometer Droplet.”J.Phys.Chem. B, vol.109(22),pp.11367-11372

[93] M. G. Pollack, A. D. Shenderov, and R. B. Fair, (2002) Electrowetting-based actuation of Droplets for Integrated Microfluidics.”, Lab Chip, vol. 2, pp. 96–101

[94] J. H. Song, et al.,(2009) A scaling model for electrowetting-on-dielectric microfluidic actuators, Microfluids and Nanofluids, vol. 7, pp. 75-89

[95] D.Brassard, L.Malic, F.Normandin, M.Tabrizian, T.Veres, (2008) Water-oil core-shell droplets for electrowetting-based digital microfluidic devices, DOI: 10.1039/b803827a

[96] S.Fan,T-H Hsieh,D-Y Lin, (2009) General digital microfluidic platform manipulating dielectric and conductive droplets by dielectrophoresis and electrowetting, DOI: 10.1039/b816535a

[97] Y.-W. Hsu, C.-H. Chen, and S.-K. Fan,(2009)Water Droplet Encapsulation By A Quantitative And Removable Oil Shell, Transducers 2009, Denver, CO, USA, June 21-25, pp.1995-1998

[98] Butt, H. J., Graf, K., & Kappl, M. (2006). Physics and chemistry of interfaces. John Wiley & Sons.

[99] H. Ren, (2004) Electro-wetting based sample preparation: an initial study for droplet transportation, creation and on-chip digital dilution, Thesis (Ph.D.), Duke University

[100] K. V. Beard and H. R. Pruppacher, (1969). A determination of the terminal velocity and drag of small water drops by means of a wind tunnel, Journal of Atmospheric Sciences, vol. 26, pp. 1066-1072

[101] Brzoska, J. B., Brochard-Wyart, F., & Rondelez, F. (1993). Motions of droplets on hydrophobic model surfaces induced by thermal gradients. Langmuir, 9(8), 2220-2224.

[102] Y-Y Lin, (2011) Low Voltage DNA Sequencing Platform Utilizing Picofluidic Electrowetting Devices (Doctoral dissertation), Duke University

[103] Hsu, B.-N., Digital Microfluidic Impactor for the Measurement of Sulfate Aerosol Concentration, qualifying exam. 2010.

[104] COMPATIBILITY, C. D., CHEAM, V., CHAU, A., & TODD, S. (2011). Burlington, Ontario, Canada. Statistical Aspects of Water Quality Monitoring, 27, 64.

[105] McSwain, M. R., Watrous, R. J., & Douglass, J. E. (1974). Improved methylthymol blue procedure for automated sulfate determinations. Analytical chemistry, 46(9), 1329-1331.

[106] Hu, H., Liang, Y., Li, S., Guo, Q., & Wu, C. (2014). A modified o-phthalaldehyde fluorometric analytical method for ultratrace ammonium in natural waters using edta-naoh as buffer. Journal of analytical methods in chemistry, 2014.

[107] Adamski, J. M., & Villard, S. P. (1975). Application of the methylthymol blue sulfate method to water and wastewater analysis. Analytical Chemistry, 47(7), 1191-1194.

[108] Standard Methods for the Examination of Water and Wastewater (1999) American Public Health Association, American Water Works Association, Water EnvironmentFederation

[109] Eatough, D. J., Major, T., Ryder, J., Hill, M., Mangelson, N. F., Eatough, N. L., ... & Fischer, J. W. (1978). The formation and stability of sulfite species in aerosols. In Sulfur in the Atmosphere (pp. 263-271).

[110] Shakya, K. M., & Peltier, R. E. (2015). Non-sulfate sulfur in fine aerosols across the United States: insight for organosulfate prevalence. Atmospheric Environment, 100, 159-166.

[111] Kérouel, R., & Aminot, A. (1997). Fluorometric determination of ammonia in sea and estuarine waters by direct segmented flow analysis. Marine Chemistry, 57(3-4), 265-275.

[112] Patton, C. J., & Kryskalla, J. R. (2011). Colorimetric determination of nitrate plus nitrite in water by enzymatic reduction, automated discrete analyzer methods. US Geological Survey Techniques and Methods, 34.

[113] Hong, J., Kim, Y. K., Won, D. J., Kim, J., & Lee, S. J. (2015). Three-dimensional digital microfluidic manipulation of droplets in oil medium. Scientific reports, 5, 10685.

[114] Kleinert, J., Srinivasan, V., Rival, A., Delattre, C., Velev, O. D., & Pamula, V. K. (2015). The dynamics and stability of lubricating oil films during droplet transport by electrowetting in microfluidic devices. Biomicrofluidics, 9(3), 034104.

[115] Paik, P., Pamula, V. K., & Chakrabarty, K. (2004). Thermal effects on droplet transport in digital microfluidics with applications to chip cooling. Proceedings of the IEEE, 649-654.

[116] Woo,R (2001) Capacitance and Microfluidics. Independent Study Project. Duke University

[117] Colovos, G., Panesar, M. R., & Parry, E. P. (1976). Linearizing the calibration curve in determination of sulfate by the methylthymol blue method. Analytical Chemistry, 48(12), 1693-1696.

[118] Choi, K., Mudrik, J. M., & Wheeler, A. R. (2015). A guiding light: spectroscopy on digital microfluidic devices using in-plane optical fibre waveguides. Analytical and bioanalytical chemistry, 407(24), 7467-7475.

Biography

Shuquan Huang went to the University of Virginia in the U.S. and graduated with Bachelor of Science degree in Electrical and Computer Engineering in 2013. Afterwards she went to Duke University in North Carolina for Ph.D. study and is expected to graduate in 2018.